Light-induced absorption changes in ferroelectric crystals: $Sr_xBa_{1-x}Nb_2O_6$:Ce; $KTaO_3$; $KTa_{1-x}Nb_xO_3$

Dissertation zur Erlangung des Grades
DOKTOR DER NATURWISSENSCHAFTEN

Von
AIRAT GUBAEV
aus Kazan, Russland

vorgelegt dem Fachbereich Physik der

UNIVERSITÄT OSNABRÜCK

Osnabrück, im November 2005

Table of contents:

1. Introduction

Strontium barium niobate $Sr_xBa_{1-x}Nb_2O_6$ (SBN with x=0.61 for the congruent composition) was synthesized and identified as a ferroelectric crystal at room temperature in the 1960s [1]. The large electro-optic coefficient could satisfy the requirement for an electro-optic material with a low half-wave voltage for laser modulation and deflection devices. After discovery of the photorefractive effect in 1966, SBN was considered as a material for holographic storage [2,3,4,5]. The first electrical fixing of holographic storage was accomplished in SBN crystals [2]. Due to its large pyroelectric effect it was also used for the pyroelectric detection [6,7]. From 1980s SBN crystals received more and more attention because a huge interest in optical information processing did appear and large size SBN crystals for optical applications also became available [8,9,10]. At this moment SBN has been considered as to be one of the most promising materials for a lot of nonlinear optical applications, among which are volume holographic storage [5,11,12,13,14] and phase conjugation [15,16,17]. The large electro-optic coefficient r_{33} makes possible a sizable modulation of the refractive index under non-uniform illumination by the electro-optic effect. In addition, the photorefractive properties of SBN crystals can be improved by suitable dopants. For example, Ce doping is found to increase the photorefractive sensitivity in the visible region by two orders of magnitude in comparison with pure SBN crystals [9,18]. Cr and Rh doped SBN crystals show enhanced sensitivity in the red spectral region due to their additional absorption bands in the red [19,20,21,22,23].

The photorefractive effect consists of several steps [24,25]:

1. illumination for instance in the form of an interference pattern formed in a photorefractive crystal by the illumination of two coherent laser beams produces photoexcited charge carriers;
2. the photoexcited charge carriers migrate to the dark region by diffusion, bulk photovoltaic effect or drift under electrical field;
3. the photoexcited charge carriers are eventually trapped in the dark region;
4. the distribution of charge between dark and illuminated areas causes a space-charge field, which modulates the refractive index via the electro-optic effect.

In many photorefractive materials the detailed origin of the photorefractive trapping centers is not completely understood, and even in materials that have been purposely doped to provide trapping centers, the lattice site occupancy of dopants and the distribution of dopant charge states are subject to variations [26,27]. Most works on SBN crystals in the past decade have been concentrated on the characterization of photorefractive properties and their applications using these crystals. Very little is known about the origin of trapping centers and the light-induced charge transport process involved in the photorefractive effect. To tailor the photorefractive properties for spectral purposes and most efficiently utilize the potential of the materials, a detailed understanding of the microscopic mechanism of the photorefractive effect and the light-induced charge transport properties in these materials is of importance.

In recent years in many unconventional photoactive solids, where the relaxation of optical excited states results in ordering motion of large number of atoms and electrons, the appearance of macroscopic domains, new structural and electronic orders have been

discovered and called "photoinduced structural transitions" [28,29]. Photo-induced (PhI) cooperative effects are facilitated in systems with hidden multi-stability, and a degenerated ground state, close to the stability limit, e.g., in a system close to a structural phase transitions (PT). Perovskite-like quantum paraelectrics $SrTiO_3$ (STO), $KTaO_3$ (KTO), at low temperatures being nearly at the quantum mechanical stability limit, are namely such materials. Therefore recent observations of giant UV light induced enhancement of the dielectric constant ("*critical behavior of giant photodielectricity*") and unconventional Debye-type dispersion in STO [30,31,32,33] and KTO [32,33,34] (in presence of a weak *dc* field [32,33] and without field [30,31,34]) have been tentatively connected with possible photo-induced phase transitions. Observations of gigantic photo-induced dielectricity under UV excitation in STO, KTO but not in quantum ferroelectric $SrTi^{18}O_3$ [32,33] allowed to propose that this phenomenon is inherent to quantum paraelectrics in the region of dominating quantum statistic, although this effect was found recently in incipient ferroelectric $CaTiO_3$ (CTO) too [33].

Two main models considered photo-induced inhomogeneities and their polarization response with mesoscopic metallic or polar clusters, formed around captured photocarriers (which can be treated as "photo-induced local structural transformation", or "local photo-induced phase transitions") were suggested. According to Ref [30,31,32,33,34], photocarriers are localized as small polarons [35,36] with a huge dipole moment and finite lifetime. Accompanying spatial lattice distortions form PI polar domains (PIPD) whose generation and annihilation induce redistribution of PIPD followed by permittivity enhancement and unconventional Debye-like dielectric relaxation [30,31,34].

There are remarkable analogies, between giant PI dielectricity in KTO and STO and dielectric properties of $K_{1-x}Li_xTaO_3$ (KLT), where dielectric relaxation and induced PT are caused by polar regions associated with Li <100> dipole off center ions in the soft KTO matrix [37]. In KTO and STO, instead of Li-related dipole systems, the dielectric response can come from polar regions (clusters) originating around captured photopolarons. [30,31,34]

Another origin of giant photodielectricity was suggested and attributed to photocarriers captured by domain boundaries associated with PIPD and a inhomogeneous insulator-to-metal transition [32]. Such intriguing result stimulated theoretical analysis of the charge carrier-doping effects on the structural instabilities in STO [38]. It was found that the electron polaron doping enhances the antiferrodistorsive TiO_6-octahedron rotation instability, while the hole polaron doping suppresses it. Both the electron and the hole polaron doping suppress the ferroelectric instability, confirming that carrier localization is essential for the comprehension of the PI gigantic dielectric effect.

Optical experiments, especially photochromic investigations under UV light irradiation, can give valuable information about the photo-charge carrier parameters, dynamics, localization, and nature of the localized states. However, there are only a few of such optical experiments containing reliable data concerning incipient ferroelectrics at low temperatures. A complex broad photo-induced absorption band observed around 1.4 eV in STO at 4.5 K [36] was tentatively attributed to transitions involving localized small electron polarons and O^- hole centers. Just recently, broad absorption bands peaking at 1.23 eV, 1.53 eV and 2.36 eV have been reported by us for reduced KTO specimens at low temperatures. [39] Additional UV-illumination in the band-gap region gave rise to broad light induced absorption bands in the

same 1-2 eV region, more pronounced for as grown and oxidized specimens. This IR light-induced effect has been tentatively attributed to different sorts of the O^- hole polaronic centers, which where revealed in recent photo-EPR experiments with KTO. [40,41]

This study presents an effort to elucidate the basic properties of the electronic excitations and photo-carriers localization, which can yield the unusual PI gigantic effects and PT. We report on photochromic effects, i.e. UV-light-induced NIR optical absorption studies for a series of diluted $KTa_{1-x}Nb_xO_3$ (KTN) single crystals. KTN is an excellent object to study the effect of the variation of the structural parameters in perovskite ferroelectrics. As mentioned above, the absence of giant photo-dielectricity in $SrTi^{18}O_3$ [32,33] lead to the suggestion that this effect is not inherent to ferroelectrics. It can be easily examined using KTN, in which, depending on the Nb concentration, various types of structural states (incipient ferroelectric – quantum paraelectric – quantum ferroelectric – ferroelectric) can be realized at low-temperatures (see details in Ref. [42]).

We intend to search for evidences of Nb^{4+} polarons and their localization in the optical absorption of KTN. Polarons and their role in structural transformations, dielectric and optical properties in ABO_3 perovskites is one of the actual and intensively discussed problems at this time (see. e.g. Refs [43,44]). Whereas hole O^- polarons have already been established in KTO, [40,41] $BaTiO_3$ (BTO)[45] and $LiNbO_3$ (LNO),[46] electron polarons were not proven experimentally neither in STO nor in KTO. Small electronic Nb^{4+} polarons are known for LNO [46] and nonisovalent Nb doping plays a crucial role in the Ti^{3+} Jahn-Teller electronic polaron formation for BTO [47]. Studies of this problem for KTN are practically absent, although the PI Nb^{4+} polaronic concept has been used as the possible origin of laser-induced transient gratings in four-wave-mixing experiments for KTN. [48]

From a practical point of view KTN is a well-known advanced material for a number of nonlinear optics applications, holographic gratings, channel switchers e.t.c. [49,50]. As well as quantum paraelectric STO and KTO, diluted KTN is a promising material for operating at cryogenic temperatures, in outer space, and now, for novel optical controlled dielectric devices.

The aim of the current work was to investigate properties of these materials like the origin of trapping centers which are involved in the charge transport process, characterization of trapping centers, like temperature dependence, illumination intensity dependence, evolution with time, spectral response, activation energies, the basic properties of the electronic excitations and photo-carriers localization, and so on. The experimental methods used in this dissertation to analyze these crystals are: absorption, light-induced absorption, photoluminescence, and photocurrent measurements.

1.1 Outline of the Dissertation

This dissertation consists of 6 chapters. The chapter "*Introduction*" is general overview and introduction to the physical problems in the field investigated. Some basic physical properties of SBN, SBN:Ce, KTO and KTN crystals, like structure, phase transitions and the experimental techniques employed in this work are described in chapter 2, "*Experimental Methods and Materials*". Chapters 3, "*Spectroscopic Study of SBN Crystals*", chapter 4, "*Spectroscopic Study of KTO Crystals*" and chapter 5, "*Spectroscopic Study of KTN Crystals*", constitute the main core parts of this dissertation, which present the experimental results of absorption, light-induced absorption, photoluminescence and photocurrent measurements, and discuss the related light-induced centers for all of these crystals, their properties and possible nature. The main results are concluded and suggestions for further work are given in the final chapter, "*Conclusions and Suggestions for Further Work*".

1.2 List of Figures

1.3 Small Polaron Theory

The possibility of self-localization of an electron at an ideal lattice site was described in [51,52]. The presence of charged defects or localized carrier-electrons or holes- can induce local polarization in solids. When the charge carrier moves relatively quickly so that only electrons of the host ions are able to adjust themselves to the different charge distribution caused by the moving charge carrier, electronic polarization occurs. If the charge carrier moves sufficiently slowly, the more massive cations and anions have time to adjust themselves to the new charge distribution. The displacement of the host lattice ions causes ionic polarization and a lattice distortion occurs in this situation. The combination of the charge carrier and the associated lattice distortion is called a polaron. When the lattice distortion is in the order of several lattice constants, normally 10-15 Å, it is called a large polaron. If the lattice distortion is about the size of one lattice constant, it is known as a small polaron. Furthermore, a combination of lattice distortions may cause two charge carriers to be attracted, which is called a bipolaron [53].
An oscillator model [54] in the configurational coordinate diagram can be used to discuss the thermally and optically induced transport properties of a small polaron as illustrated in Fig. 1.3.1. In this model, a harmonic oscillator representing the host lattice, is perturbed by a constant force representing the interaction of the charge carrier and the lattice.

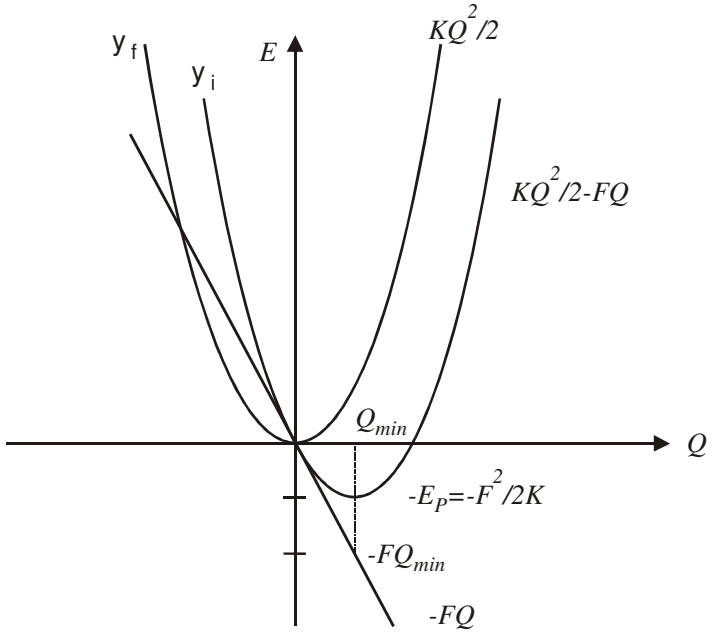

Fig 1.3.1. The influence of the charge carrier with the constant force F on a harmonic oscillator represented by a parabola.

The elastic energy of the harmonic oscillator has the form of

$$E_{elast} = \frac{1}{2} KQ^2 \tag{1.3.2}$$

where Q is the configurational coordinate, K is the elastic coefficient. The presence of an electron (or hole) changes the total energy, in the first order, by a linear term, $-FQ$, where F is the force exerted on the oscillator. Therefore the total energy is given by

$$E = \frac{1}{2}KQ^2 - FQ \tag{1.3.3}$$

One finds the stabilization energy of a small polaron (the binding energy) in the form of

$$E_p = E(Q_{\min}) = -\frac{F^2}{2K} + \frac{F^2}{K} = \frac{F^2}{2K} \text{ with} \tag{1.3.4}$$

$$Q_{\min} = \frac{F}{K} \tag{1.3.5}$$

Let's consider two equivalent sites *1* and *2*. If an electron is to jump from one site to another site, the configurational coordinate parameters Q_1 and Q_2 must be such that the electron's energy is the same in either site, thus

$$FQ_1 = FQ_2 \tag{1.3.6}$$

so that $Q_1=Q_2$. The energies required to distort sites *1* and *2* to configurations in which $Q_1=Q_2=Q$ are

$$\frac{K}{2}(Q - Q_{\min})^2 \text{ and } \frac{K}{2}Q^2 \tag{1.3.7}$$

which add up to a total energy E_a given by

$$E_a = \frac{K}{2}(2Q^2 - 2Q_{\min}Q + Q_{\min}^2) \tag{1.3.8}$$

There is a minimum when

$$Q = \frac{Q_{\min}}{2} \tag{1.3.9}$$

and E_a has the value

$$E_a = \frac{K}{4}Q_{\min}^2 = \frac{F^2}{4K} = \frac{E_p}{2} \tag{1.3.10}$$

This is the activation energy for the hopping motion of a small polaron. A small polaron may move from one site to its neighbor site via two distinct types of processes [55,56]: the first process involves the tunneling of a small polaron between adjacent lattice sites with no charge in the population of any phonon mode (so-called band motion); the second corresponds to the phonon assisted tunneling (hopping motion) of the carrier between adjacent sites. In an ideal crystal, the small polaron band mobility will dominate at low temperatures. With rising temperature, the contribution of the hopping motion will increase and at sufficiently high

temperature the small polaron motion will proceed predominantly via hopping. However, the extreme narrowness of the small polaron band leads one to expect that the band motion typically will be washed out by whatever disorder exists in a real crystal. Therefore, usually only the hopping motion of small polarons exists in a real crystal. At a sufficiently high temperature the small polaron hopping motion rate is proportional to $exp(-E_a/kT)$.
The energy E_{opt} required to transfer an electron optically from one site to another, without moving the ions according to the Franck-Condon principle, is

$$E_{opt} = FQ_{\min} = \frac{F^2}{K} = 2E_p = 4E_a \,. \tag{1.3.11}$$

The frequency dependence of the optical absorption of small polarons is discussed in full detail by Reik and Heese [57,58]:

$$\alpha = \frac{\sigma}{c\varepsilon_0 n} \text{ with} \tag{1.3.12}$$

$$\sigma = \sigma_0 \frac{\sinh(\hbar\omega / kT)}{\hbar\omega / kT} \exp(-\omega^2\tau^2 r(\omega)) \tag{1.3.13}$$

where σ is the real part of the conductivity, σ_0 a scaling factor related to the conductivity at zero frequency, n the index of refraction, ε_0 the dielectric constant, c the speed of light, ω the frequency of light, $\hbar$ the Plank constant, k the Boltzmann constant, T the absolute temperature, τ the moment relaxation time and $r(w)$ a function weakly decaying with frequency [57,58].

The electron-lattice interaction can act with the localizing potentials associated with defects to produce small-polaronic localized states [56]. Consider, for example, an electron in a deformable lattice in the presence of a positively charged defect. If without any electron-lattice interaction, there is a single finite-radius (hydrogenic) minimum associated with an electron in the defects coulomb well (like in the case of color center). However, when the attractive potential of the defect and the electron-lattice interaction are both of sufficient strength, the barrier to the small-polaronic state is eliminated and only the small-polaronic state survives. Thus, the localizing potentials of defects generally reduce, and sometimes destroy, the barrier to self-trapping, thereby enhancing the possibility that small polarons will form.

2. Experimental Methods and Materials

2.1. Fourier Spectroscopy

From times of Newton the optical spectroscopy always was one of the most informative methods of research of matter. Lately ways of registration of radiation have been essentially modernized, new type of detectors start to be available and so on. However principles of construction of spectral devices up to the middle of 20ths century practically did not change. Devices traditionally were build with the same schema: radiation is focused on an entrance slit, then by the help of a mirror with a focus on the entrance slit light as a parallel beam goes on an dispersive element (long time it was a prism, in 20ths century it began to be replaced by diffraction lattices) and after focusing on a exit slit radiation is registered by a detector. In the second half of 20ths century's rapid development of interference spectroscopy with Fourier transformation began.

Advantages of Fourier-spectroscopy compared with other spectroscopic methods using decomposition in a spectrum are defined first of all by the energy advantages that have received the name of Jacquinot and Fellgett.

The first is that at Fourier-spectrometers the entrance aperture is greater than at dispersive devices, light in which gets through a narrow entrance slit. This advantage is seen from comparison of entrance parts of the systems and it can reach hundreds of times. Also resolution depends mainly on the path difference, but not so strongly on the entrance aperture size.

Second advantage (Fellgett's multiplex advantage) is connected with the fact that in usual spectrometers each spectral interval is measured in steps while in Fourier-spectrometers the time of registration of each spectral interval is equal to the time of registration for the whole spectrum. Fellgett's multiplex advantage is proportional to the number of resolved intervals in the registered spectrum. The reason for appearance of such an advantage can be understood from comparison of exit parts of systems, and its size also reaches hundreds times. Both factors together can give an advantage of about four orders in the size of registered energy.

An essential advantage of the FTIR method is also the absence of restrictions due to the sizes of optical elements. It is difficult to expect, that the size of diffraction lattices or especially prisms will be more than 50 cm. This gives us a natural limit for the resolution of the devices that is using a spatial dispersion equal about to 0,02 cm^{-1}. At the same time serial industrial Fourier-spectrometers resolution is mainly depend on the path difference and can reach up to 0,002 cm^{-1} (for example with 3.2 m path difference and Bruker IFS120HR Fourier spectrometer).

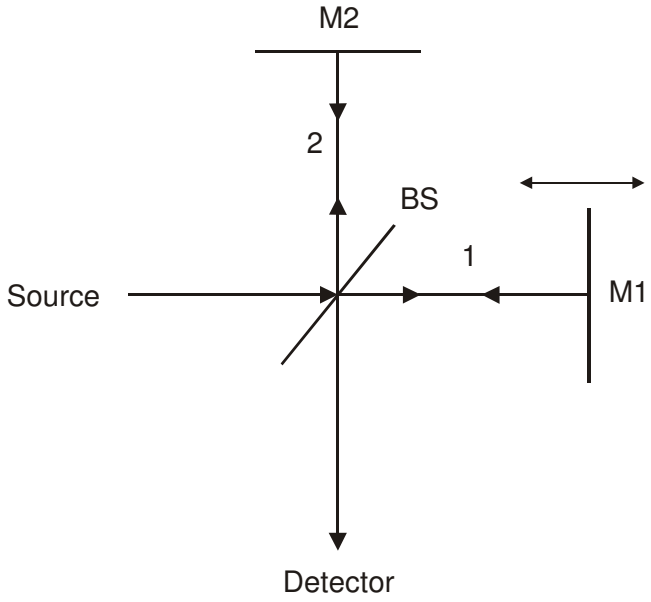

Fig. 2.1.1. Scheme of Michelson Interferometer.
BS- Beamsplitter, 1- channel with moving mirror, 2-channel with fixed mirror.

The typical optical circuit of a Fourier-spectrometer is based on a Michelson interferometer design (fig. 2.1.1). Light is passing through an entrance diaphragm and falls on a collimating mirror and a parallel beam goes to the beam splitter. The beam splitter usually represents a transparent plane-parallel plate with a coating.

The ideal beam splitter should reflect and pass exactly 50 % of light and should not have any absorption in all the spectral region of the device. The deviation from this requirement reduces the efficiency of its work. However, it is very difficult to realize such requirement especially in the infrared area of a spectrum. Therefore in Fourier-spectrometers usually exist several replaceable beam splitters. In the field of low frequencies when the length of a wave exceeds 25 microns (microwave area) beam splitters usually made from polymeric films.

After the beam splitter the passing and reflected beams go on to the reflecting mirrors, requirements to the quality of them and of the stability in the interferometer are very high: their surface should not deviate from the ideal wavefront more than for 1/20 lengths of the short-wave border of the working region of the device. Recently, instead of flat plates people began to use corner cube reflectors made of three mutually perpendicular plates. Such a design has allowed lowering the requirement for stability because for the corner cube reflector the incoming and reflected beams remain parallel under rotation of the reflector.

The interferometer output light is focused by a mirror objective to a place where the sample is located, if spectra of absorption are investigated. After that light is focused on the detector of the radiation. With the help of the Fourier transformation we can get spectral distribution of the light intensity:

$$I(\nu) = \int_{-\infty}^{\infty} I(x) \cos(2\pi\nu \cdot x)\, dx \qquad (2.1.2)$$

Where *I(x)* is intensity dependence on the path difference, *x* is the path difference, and later we can get the ratio between the reference channel and sample channel versus frequency.

The important element of the optical circuit is the system of measurement of a path difference between the interferometer mirrors. For this purpose radiation of single mode laser is used (usually it is a He-Ne laser), which in precision devices is in addition stabilized. In its path through the interferometer the monochromatic He-Ne laser beam generates upon movement with constant speed of a mirror a sine wave signal on a special receiver. The period of a sinusoid is equal to the length of a wave of laser radiation. This signal, after transformation, is used in creation of command pulses for reading indications from the detector of radiation in the detecting-amplifying system of the interferometer for the displacement of the mobile mirror as a function of the distance (with other words, path difference) equal or multiple this length. Due to such a system the Fourier-spectrometer becomes a device with high accuracy for measurements of frequencies of spectral lines, and the accuracy is determined by the accuracy of the basic laser.

The technique when the mirror moves rapidly and we collect the data continuously gives us the advantage in working with AC amplifying and detecting systems, that as a result reduces noise, and increases the speed of single measurements.

The transition from conventional methods to the Fourier-spectroscopy has allowed to increase essentially the spectral resolution, speed of registration and the signal to noise ratio. With appropriate light sources, beamsplitters and detectors, the measurable spectral region can be extended from the UV to the far infrared region. The signal to noise ratio can be improved even more with the help of superposition of many scans (this will improve the signal to noise ratio $\sqrt{n}$ times). For this reason the Fourier-spectroscopy now is used even for routine measurements.

2.2 Bruker IFS-120HR, High Resolution Fourier Spectrometer

Absorption spectra and light-induced absorption in this work were measured with the help of the Fourier spectrometer Bruker IFS-120HR. Schematically it is drawn in Fig 2.2.1. The light source chamber consists in several light sources like tungsten lamp, globar and through the external port the Osram XBO lamp is connected for measurements in the UV/VIS region. A dichroic filter is used to reflect the light with wavelength less than 500 nm. The same Xenon lamp is used as illumination source for light-induced absorption experiments. For the different spectral regions the Fourier spectrometer has a set of

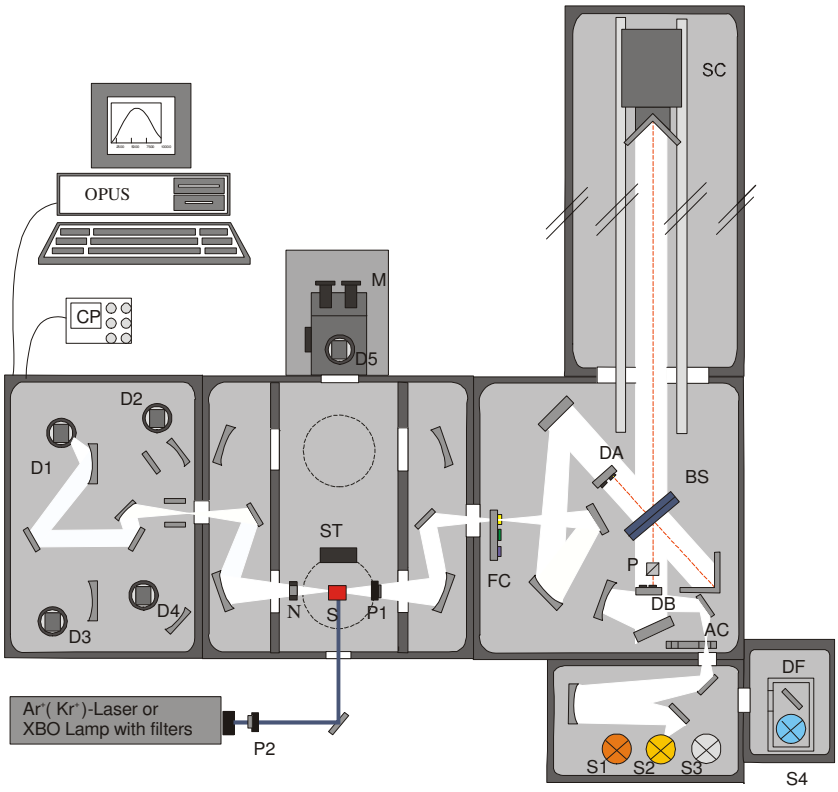

D1-D5: Detectors
S1-S4 : Light Sources
M : External Microscope
DF : Dichroic Filter
FC : Filter Changer
AC : Aperture Changer
ST : Beam Stopper
P1-P2 : Polarizors

S : Sample
DF : Dichroic Filter
P : Coupling Prism
SC : Scanner
DA-DB : Diode Pairs
OPUS : Control Software
CP : Control Panel
N : Notchfilter
BS : Beam Splitter

Fig 2.2.1. Scheme of Bruker IFS120HR- high resolution Fourier spectrometer.

Range ν in cm^{-1}	**Source** ν in cm^{-1}	**Beamsplitter** ν in cm^{-1}	**Detector** ν in cm^{-1}	**Modulation Frequency**, KHz
UV 35000-20000	Xenon 35000-20000	UV/Quartz 45000-8000	Photomultiplier 35000-10000	7.5
			GaP- Diode 30000-18000	7.5
VIS 20000-10000	Tungsten 25000-3000	VIS/Quartz 25000-8000	Si-Doide 32000-9000	20
NIR 10000-2000	Tungsten 25000-3000	Si/CaF_2 10000-1000	Ge-Diode 14000-6500 (Cooled with LN_2)	5
			InSb 9000-2000 (Cooled with LN_2)	40
FIR 2000-100	Globar 5000-100	Ge/KBr 4800-400	HgCdTe (MCT) 6000-800 cooled with LN_2	10

Table 2.2.2. The light sources, beamsplitters, detectors and modulation frequencies for different spectral regions.

beamsplitters and detectors (see table 2.2.2.). A frequency stabilized Spectra-Physics He-Ne laser (λ=632.8 nm) is used to control the moving mirror and for frequencies measurements. In our Fourier spectrometer due to maximal path difference restrictions highest resolution possible is 0.0035 cm^{-1}. There is a reference channel and sample channel in the Fourier spectrometer.

Ar^+ laser and Kr^+ laser (Spectra physics type 171), red laser diode or XBO lamp with set of filters are used as illumination sources in light –induced absorption experiments. Pumping light can be applied in perpendicular and parallel way in respect to the Fourier measuring light direction.

For time resolved measurements like build-up and decay processes of the light-induced absorption time marks of the rapid scan method is used. The time resolution is restricted by maximum velocity of the scanner and chosen spectral resolution, and in the case of IFS-120HR and our measurement needs it is equal to about 0.5 s (we are using $10cm^{-1}$ resolution for light-induced absorption spectra).

2.3 Luminescence Measurements

The experimental setup for photoluminescence and thermoluminescence measurements is shown in Fig 2.3.1. The registration channel consists in a photon counting system based on SPEX1402 double grating monochromators and cooled RCA31034 GaAs photomultiplier. As the excitation source we used a high pressure Xenon Lamp (ILC Cermax, 300W) with SPEX Minimate for wavelength selection together with variable bandpass filters. A closed cycle cryostat (Leybold, 10-300 K) and programmable temperature controller (LTC60, Leybold) is used for measurements. For lifetime measurements a multichannel scaler (EG&G 914P) is used.

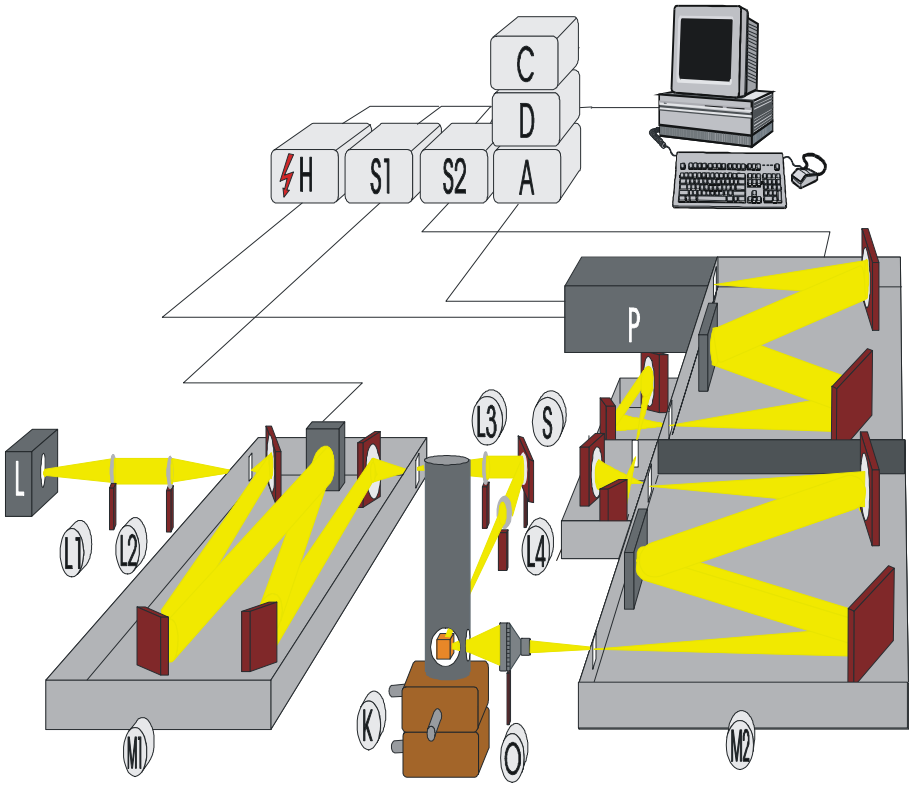

(A) Amplifier
(C) Counter
(D) Discriminator
(H) High-Voltage Power-Supply
(K) Cryostat (Crystal Position)
(L) XBO-Lamp (450 W)
(L1) -(L4) Lenses

(M1) Spex Minimate
(M2) Doppel-Monochr. Spex 1402
(O) Objective
(P) Photomultiplier
(S) Mirror
(S1) Drive System Minimate
(S2) Drive System Spex

Fig 2.3.1. Scheme of setup for luminescence and thermoluminescence measurements.

2.4 Helium Bath Cryostat

For absorption measurements at low temperatures (in range of 1.3 K-300 K) a helium bath cryostat (Fig. 2.4.1) is used. For an improved temperature stability the crystal can be immersed in superfluid helium. Liquid nitrogen is used to shield the inner helium tank from room temperature. Liquid helium from the big tank in the upper part of the cryostat is flowing through a small capillary tube to the inner part of the cryostat where the samples are located. Under pumping in the sample part the superfluid state of the helium can appear, so even under illumination in light-induced experiments heat from the sample can be immediately removed to the superfluid helium. A Lakeshore temperature controller (321, and Si-diode, Lakeshore, D type) and heater are used to control the temperature inside the sample part and give the possibility to take measurements at various temperatures.

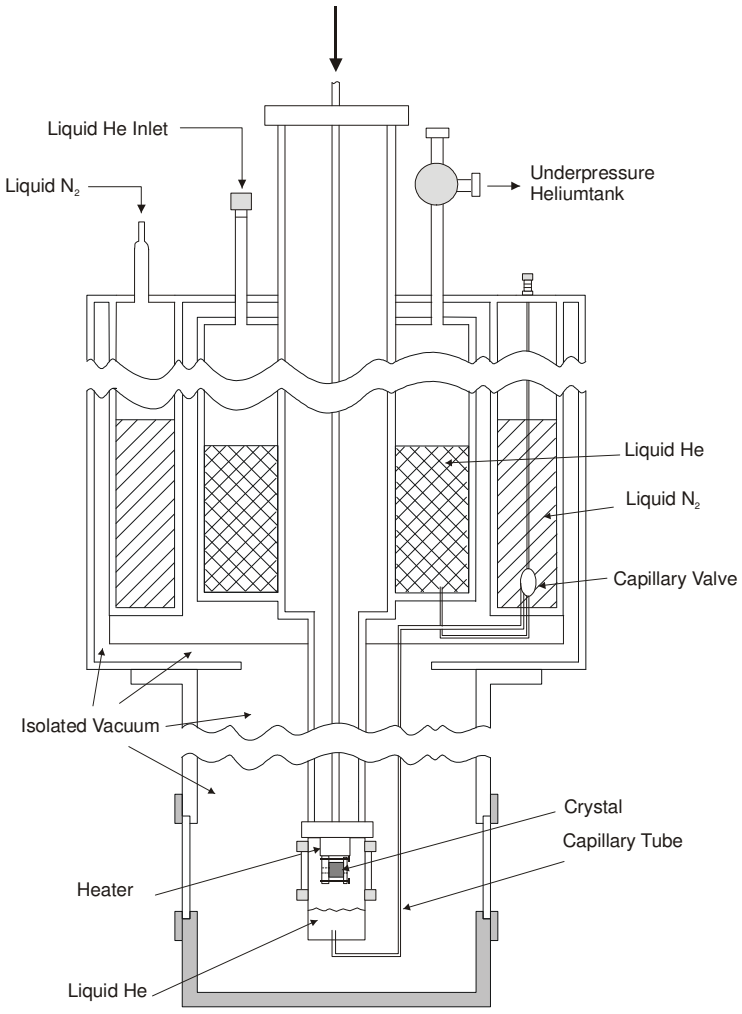

Fig 2.4.1. The Helium bath cryostat for absorption measurements at low temperatures.

2.5 Oxidation and Reduction Treatment

For gas treatments we used an oven, drawn in Fig 2.5.1. The inner part of the oven can be evacuated first and then filled with different gases (for oxidation we used O_2 gas, for reduction H_2 or vacuum). Temperature is controlled by special hardware and can be varied from room temperature till 1300 C^0.

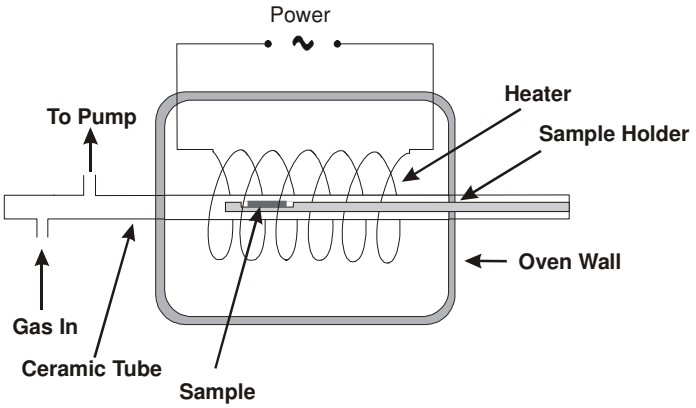

Fig. 2.5.1. The oven for oxidation and reduction treatment of samples. Ceramic tube and sample holder are made from Al_2O_3.

2.6 Setup for Measurements of Photo-Hall Effect

For measurements of charges that appear under different illumination or under heating procedure we used a setup based on a cryostat (Oxford) with superconducting magnet (split coil, 8 Tesla). For registration of Hall voltages we used two digital voltmeters (Kethley 2000). Special programs were written using LabView 7.0 for automation (controlling magnet field, registering experimental data from voltmeters, registering temperature during measurements) and saving of experimental results. For field control also a digital to analog converter using the parallel interface of a PC and several elements from the Maxim-IC Company were build during my work in Osnabrueck University. The scheme of the photo-Hall setup can be found in Fig 2.6.1.

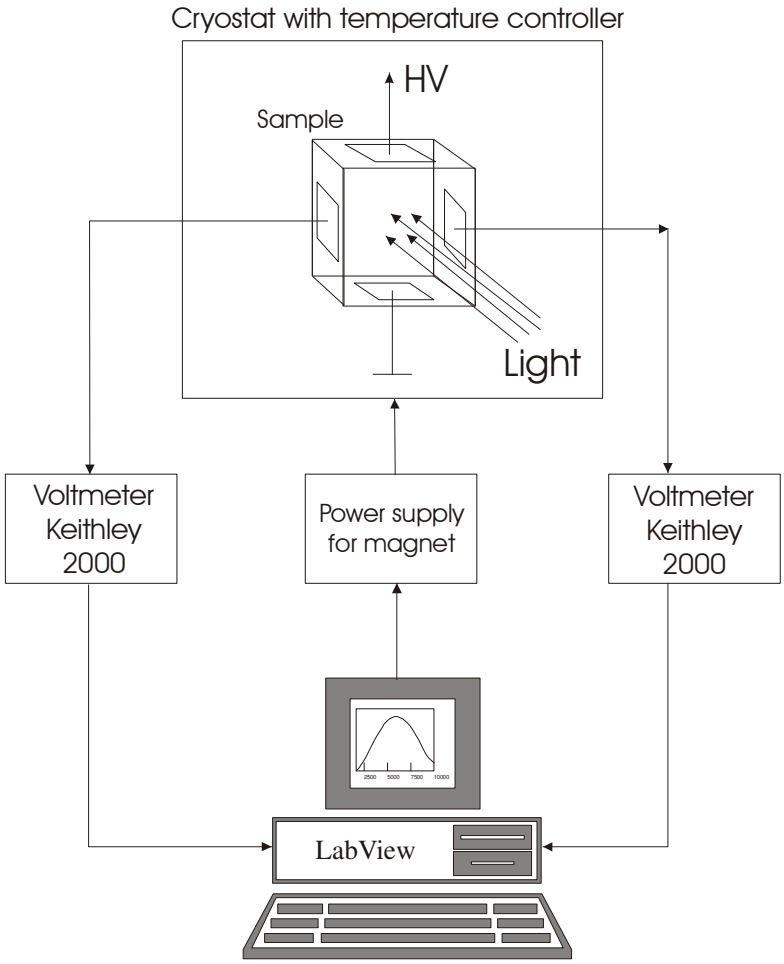

Fig. 2.6.1. The scheme of the Photo-Hall setup. The sample is located in the cryostat between two magnet coils. Temperature could be varied from 2 K till 400K. The highest value of the magnet field is 8 Tesla. The sample can be illuminated through optical windows.

2.7 $Sr_xBa_{1-x}Nb_2O_6$ (SBN), $KTaO_3$ (KTO), $KTa_{1-x}Nb_xO_3$ (KTN) Crystals

2.7.1 SBN Crystals, Growth, Structure and Properties

All congruent crystals (x=0.61, where melt and crystal have the same composition) were grown by Dr. Pankrath using the Czochralski method at the Crystal Growth Laboratory of the Physics Department at the University of Osnabrueck. The ultrapure raw materials for crystal growth are $SrCO_3$, $BaCO_3$ and Nb_2O_5. Various concentrations of CeO_2 were added into the melt in order to obtain Ce-doped SBN crystals. The crystals are grown in the c-direction and pulled-out with a speed of 0.8 mm/h, rotation rate 7round/min, growth temperature 1510° C, the temperature gradient above the solid-liquid interface 0.5° C/cm and below the solid-liquid interface 1.5° C/cm (Resistance heating is used to achieve these values). The striation-free and optical quality SBN crystals were obtained in a typical length of 100 mm and the diameter of 10 mm.

SBN pure

SBN crystals belong to the tungsten bronze family of crystals with the general chemical formula: $(A1)_4(A2)_2C_4(B1)_2(B2)_8O_{30}$. The lattice structure is shown in Fig. 2.7.1.1. One unit cell consists of ten BO_6 octahedra linked by their corners to form three different types of tunnels along the c axis of the crystal. These structures are shown in Fig. 2.7.1.1 as A1, A2 and C channels, which correspond to 15-, 12- and 9-fold oxygen coordinated lattice sites, respectively. Both B1 and B2 are 6-fold coordinated sites located inside the BO_6 oxygen octahedera units. The structure is consisting from two alternating layers parallel to the (001) plane. One layer contains the A1, A2 and C sites while the other layer contains the B1 and B2 sites. The unit is one octahedron high with a length of c=3.9 Å and has transverse dimensions of a=b~12.5 Å.

At room temperature SBN crystals are ferroelectric and the point group of this phase is 4mm. According to Jamieson et al. [59] studies the structure of $Sr_{0.75}Ba_{0.27}Nb_2O_6$ is a partially filled lattice in which on average only five of the six available A1 and A2 sites (83.3%) are occupied by Sr^{2+} and Ba^{2+} cations. It was shown that Ba atoms located in the large tunnels occupy their site with an occupancy factor of 34.4 %. The same sites are 50.3 % filled by Sr atoms. The A2 sites are 82.2 % occupied by Sr^{2+}. The variable filling of the A1 and A2 sites in SBN crystals creates a degree of structural disorder that destroys translational invariance of the lattice and is responsible for the diffuse nature of the ferroelectric phase transition. In the case of the congruently melting composition x=0.61 the tetragonal tunnels are occupied 72.5% by the Sr atoms [60] and T_c = 80 °C.

In addition, the composition of SBN crystals can vary in wide range of $0.25<x<0.87$. Megumi et al. [61] found that the congruent composition of SBN crystal lies around x=0.61 where the crystal has the same composition as the melt. The open crystal structure and the composition flexibility provides a large possibility to accommodate different dopants to enhance the sensitivity of the crystals in various wavelength regions (from transition metal

ions to rare-earth metal ions). At the same time, the structural disorder of the crystal makes it difficult to accurately determine the occupancy sites of the impurities introduced.

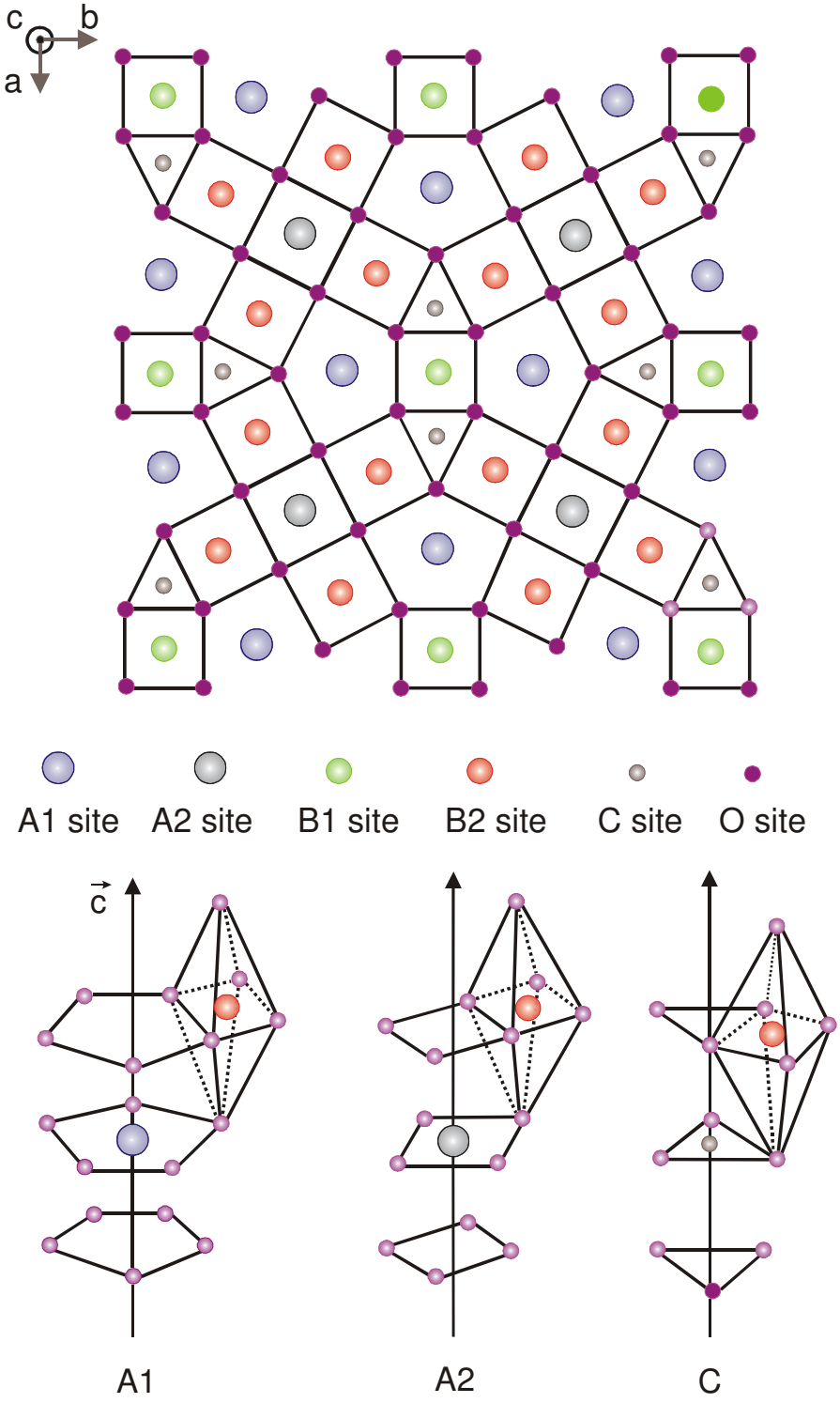

Fig. 2.7.1.1 Tungsten bronze structure of SBN.

Since the spectroscopic properties of these impurity ions usually depend on the surrounding crystal field, it is of interest to study the possible influence of the crystal field on the spectroscopic properties of doped ions in SBN.

The ferroelectric phase transition refers to the transformation of the crystal from a non-polar paraelectric state to a polar ferroelectric state. The location of the transition on the phase diagram is a function of temperature, pressure (i.e. stress), electric field and composition of the crystal. Near the transition the spontaneous polarization of the crystal becomes very sensitive to a change of these parameters. The transition temperature measured under conditions of constant stress and electric field is called the Curie temperature T_c. Since SBN crystals have a disordered lattice structure, it is characterized by a compositional distribution and hence displays a diffuse phase transition [63].

The point group of SBN crystal is 4/mmm in the paraelectric state and 4mm in the ferroelectric state. The Curie temperature T_c of SBN crystal is found to strongly depend on the composition, ranging from about 50 °C for x=0.75 to about 200 °C for x=0.25. The phase transition temperature of the SBN crystals with the congruent composition (x=0.61) is about 80 °C. A roughly linear relationship between T_c and the composition parameter x exists as shown in [62] and with increasing of the Ba content in the crystal T_c is linearly increasing. Therefore, changing the crystal composition can easily alter all the properties associated with the phase transition. SBN crystal with x=0.33 exhibits a minimum of the entropy of the ion distribution in which case only Ba^{2+} ions occupy the A1 sites and Sr^{2+} ions occupy A2 sites [59]. Above x=0.33 the structural disorder increases with the Sr/Ba ratio in SBN and the dielectric measurements show an increasingly broadened structure.

Another phase transition is found to exist at low temperature in SBN crystal [63,64]. The dielectric and pyroelectric constants show a peak around 60-90 K. From the X-ray diffraction result, the phase transition is from the tetragonal point group 4mm to the monoclinic point group m [63,64].

Doped SBN

Since the electro-optic coefficient is largely independent on most impurities [8,9,65], the photorefractive properties, like photorefractive sensitivity, response speed and response spectral region, can be modified by adding suitable impurities to the crystal. Ce doping has been found to improve the sensitivity of SBN crystals in the visible region by two orders of magnitude [9]. Pure SBN has very little absorption in the visible, but Ce doping induces a broad absorption band in this region and therefore the photorefractive properties are enhanced considerably. Other impurities like Rh, Cr have also been added to the crystal to improve the sensitivity and response speed of the crystal [19,20,21,22,23].

Ce doping is found to influence the phase transition temperature. The dielectric measurement results show that the temperature of the maximum of the dielectric constant T_m decreases linearly with increasing Ce concentration from 80 °C in case of zero doping till room temperature in case of two mol percent of CeO_2 in the crystal as shown in [63,66,67] and in Fig 2.7.1.2. For Ce ions in SBN a majority charge state 3+ has been determined [68], from measurement by instrumental neutron activation analysis Ce^{3+} ions have been found to replace mainly Sr^{2+} ions [69] thus lowering the Sr/Ba ratio. In contrast, pure SBN crystal has

an increasing T_c with decreasing Sr/Ba ratio. The Ce^{3+} content can be identified by a broad absorption band extending from the visible range to the UV band edge and additional far-infrared bands near 2000 cm^{-1} due to $^2F_{5/2}$-$^2F_{7/2}$ optical transitions of Ce^{3+} (see Fig 3.1.4, page 33).

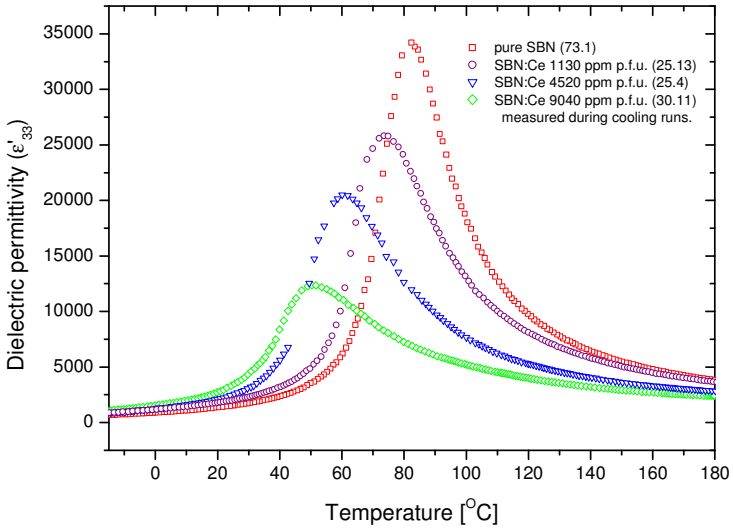

Fig.2.7.1.2. Dielectric susceptibility in SBN:Ce with different Ce doping [67].

The accompanying decrease of T_c with dopant concentration indicates a suppression of long range ordering by impurity related random fields due to charge mismatch brought by the Cr and Ce doping. The increased width of the ε´(T) maximum can be regarded as consequence of nonuniform distribution of the doping ions. Ce doping has a depressing effect on T_c and no self compensation of Ce and Cr ions was found in the experiments with co-doped crystals, which can be understood on the basis of a local charge compensation in the oxygen sublattice around each defect [67].

Li-doping of 0.35 wt% and 0.5 wt% to SBN (x=0,52) seemed to enhance T_c as shown in Fig. 2.7.1.3, but addition to a Cr-doping did reveal rather a further lowering of T_c. The doping with small Li-ions is expected to enhance T_c, due to a possible dipolar off-center nature of the small Li-ions, but this did not seem to take place in the Chromium co-doped crystals. The corresponding absorption spectra for SBN:Cr+Li (10000 ppm p.f.u. each in melt) are shown in Fig 2.7.1.4.

Samples were prepared as optically polished parallelepipeds with faces oriented along <100> axes of the crystal.

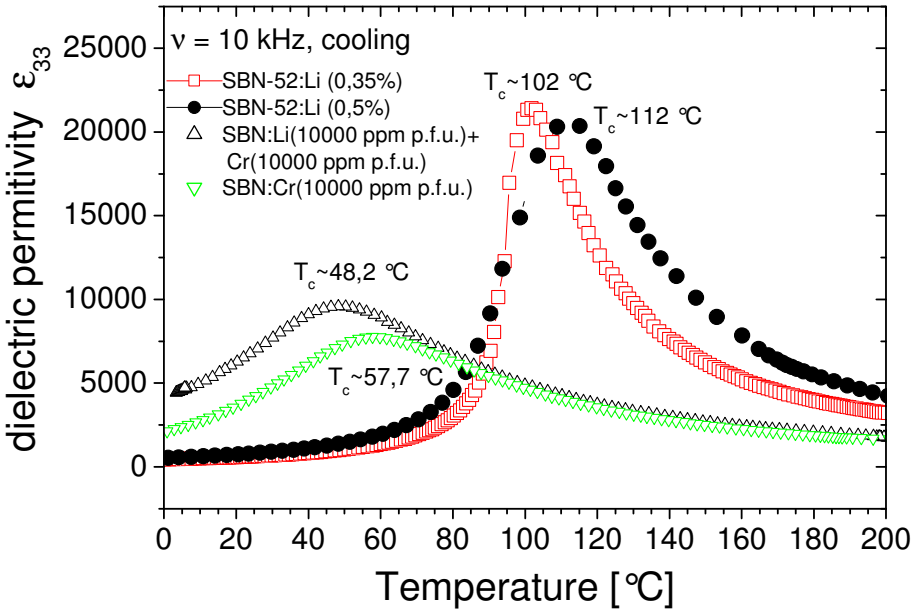

Fig. 2.7.1.3. Dielectric susceptibility in SBN:Li (x=0.52) with two Li doping concentrations, SBN:Li+Cr (10000 ppm p.f.u. each in melt, x=0.61) and SBN:Cr (10000 ppm p.f.u., x=0.61) measured during cooling runs.

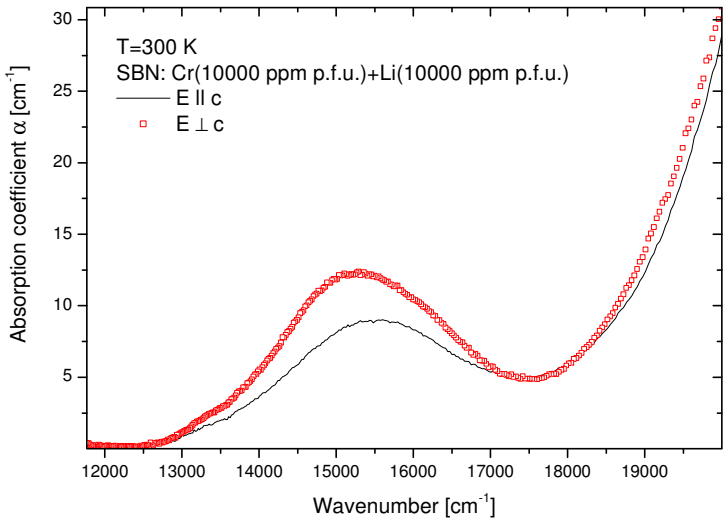

Fig. 2.7.1.4. Absorption in SBN: Cr+Li (10000 ppm p.f.u. each in melt)

2.7.2 KTO and KTN Crystals, Growth, Structure and Properties

Many oxides (as well as some non-oxides) crystal systems can be described by the general formula $A_mB_nC_p$. However usually a combination of two cations A and B with an anion C appears. In the latter manner ABO_3 is used when the anion is oxygen ion.

The radii of the cations are determining the structure of the crystal. If radii of cations have similar sizes, then the structure of the crystal is described as the structure of ilmenite (ilmenite, $FeTiO_3$). In the ABC_3- structure, in which the ionic radius of the A- cations is substantially greater than that of B- cations, the structure corresponds to the perovskite type ($CaTiO_3$) with a cubic symmetry of the crystal. The crystal systems, within the framework of this study, are related to this type of crystal.

Fig. 2.7.2.1 represents the unit cell of the general ABO_3 structure of the perovskite. In this case the large A ions are occupying the corners of the elementary cube, the smaller B ions – are in the center, and the O ions – are in the middle of the surface and are forming an octahedron around the B ions. A ions and ions of oxygen forming a densest cubic ball packing. A ions are surrounded by 12 O ions (cubic octahedron), B ions are surrounded by 6 O ions, which is described by chemical formula $A^{[12]}B^{[6]}O_3{}^{[4+2]}$.

Not only crystals with identical radii of the ions are displaying the perovskite structure, for which the sum of radii should fit to equation:

$$R_{Ca} + R_O = \sqrt{2}\left(R_{Ti} + R_O\right) \tag{2.7.2.2}$$

In the limits of the permissible changes, inside which the structure of perovskite still can appear, i.e., where the equation for the radii is:

$$R_A + R_O = t \cdot \sqrt{2}\left(R_B + R_O\right) \tag{2.7.2.3}$$

Where the t is the coefficient of admittance determined by Goldschmidt [70]. This coefficient can take the values between t = 0.8 - 1.1 [71]. The valency of ions can, however, vary (for example $A^{2+}B^{4+}O_3$, $A^{3+}B^{3+}O_3$ or $A^{1+}B^{5+}O_3$). In many cases the crystals with the perovskite structure do not have ideal cubic structure. Partly covalent bonding influence the band structure of the crystal.

The ideal cubic structure usually exists in the high-temperature phase. Crystals show a phase transition, which is expressed only by insignificant displacement of atomic positions, i.e., the original structure is distorted. The highly symmetrical perovskite crystal structure represents an entire family of low symmetrical structures of the crystals at low temperature, where this structure with high symmetry is used as the prototype.

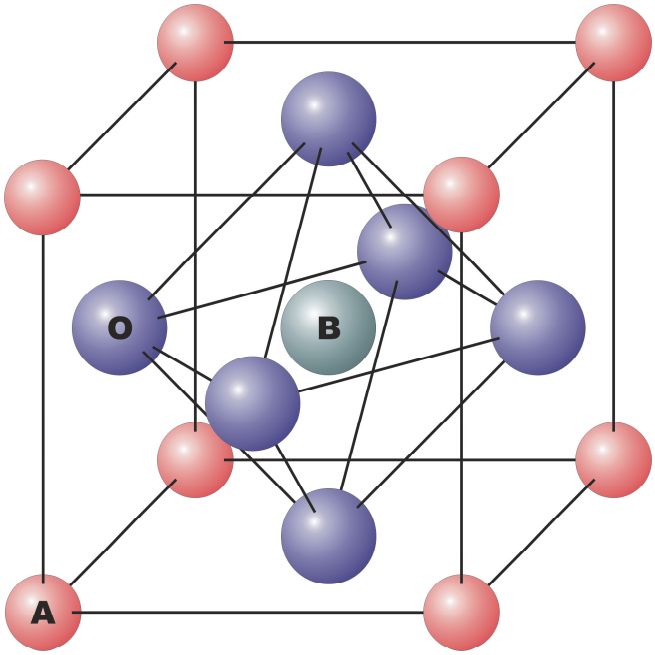

Fig. 2.7.2.1. Ideal unit cell of perovskite.

Crystals of potassium tantalate were grown by Dr. Hesse at the Crystal Growth Laboratory of the Physics Department at the University of Osnabrueck from the melt with 42 mol% Ta_2O_5 and 58 mol% K_2O at a temperature of 1358 ºC. The starting materials (Merk, ultrapure) for crystal growth are Ta_2O_5 and K_2CO_3 or K_2O with surplus of K_2CO_3 or K_2O. As it is shown in the phase diagram [72] that the crystal growth is possible when one has 50-67 mol% K_2CO_3 in the melt. The crystals have cubic perovskite structure (symmetry group Pm3m), and the symmetry of the crystals does not change from room temperature till low temperatures.

According to the nomenclature of perovskite structures, K ions have occupied the A position, Ta ions the B position. From the ionic radii of K^+, Ta^{5+} and O^{2-} ions the determined Goldschmidt factor is t=0,94. At room temperature the lattice constant for potassium tantalate is a=3.9884 Å [72, 73]. The lattice constant changes with temperature are shown by Samara and Morosin [73] in the temperature range from 90K till 600 K (fig 2.7.2.4).

The temperature dependence of the dielectric constant for $KTaO_3$ shows a behavior that is observed usually for ferroelectrics in a para-electric phase, while approaching a phase transition at low temperatures. A study of the temperature dependence of the dielectric constant and susceptibility for $KTaO_3$ was done by Wemple [74] and is shown in Fig 2.7.2.5. Quantum fluctuations at low temperatures and as the result the behavior of a soft mode in $KTaO_3$ is preventing the crystal from the phase transition (Fig. 2.7.2.6, [75,76]). For three perpendicular TO optical modes in $KTaO_3$ the TO-phonon shows the lowest frequency and its frequency is decreasing with the temperature [76,77,78]. Rupprecht and Bell with the help of a modified law of Curie-Weiss-type did get an extrapolated Curie temperature of T_c=2.8 K.

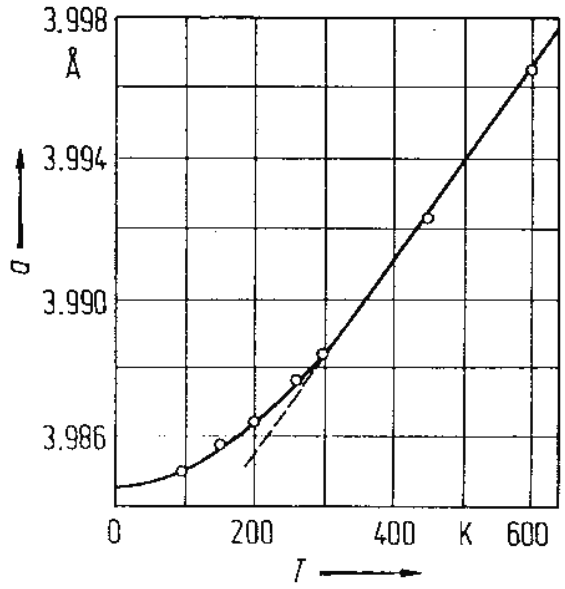

Fig. 2.7.2.4. The lattice constant changes with temperature for $KTaO_3$ [73].

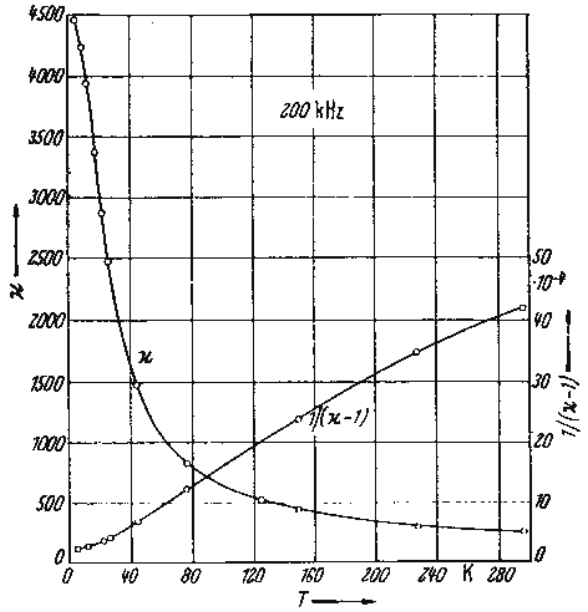

Fig. 2.7.2.5. The temperature dependence of a dielectric constant and susceptibility for $KTaO_3$ [74].

A ferroelectric phase transition is not observed in $KTaO_3$, not even below 2.8 K. Because the dielectric constant and the soft mode show a behavior that is expected for approaching from high T a phase transition, which is, however, not taking place, $KTaO_3$, in analogy to $SrTiO_3$ is named an incipient ferroelectric.

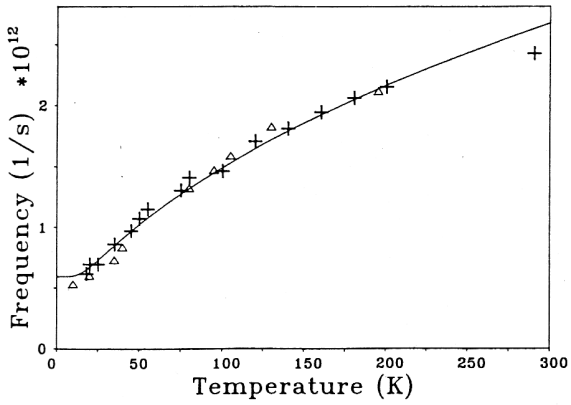

Fig. 2.7.2.6. Soft mode frequency of KTaO3 as measured by Fleury and Worlock [75] (Δ) and Vogt and Uwe [76] (+). Calculated frequency variation (solid line) from Barrett's formula.

However it is possible to induce a ferroelectric phase transition in $KTaO_3$. That, for example, is possible with the help of uniaxial external pressure [79,80] or with the help of applied external electric field [81,82]. Also introduction of such an off-center, dipolar impurity as Nb or Li into the $KTaO_3$ crystal causes the occurrence of a second order phase transition [83,84]. The ferroelectric phase transition for $KTaO_3$:Li with a contents of lithium of about 5 % occurs approximately at T=80 K [85]. The temperature of the phase transition depends on the contents of lithium in the crystals in a nonlinear way.

KTN ($KTa_{1-x}Nb_xO_3$ with $0 \le x \le 1$) also crystallizes in perovskite structure. From the phase diagrams of Hellermann [86], and also from Reisman [87] the mixed crystal is formed as single crystals in the range $0 \le x \le 1$. At low concentrations of Niobium (ratio between Niobium –Tantalum is small) usually the Niobium content in the crystals is smaller than in the melt. During the growth process of the crystal the Tantalum concentration is changing and the ratio between Niobium and Tantalum is changing in the crystal. The content of niobium determines the phase transition temperatures. Both Triebwasser [88], and Baller [89] have found that the phase transition temperature has a linear dependence on the concentration of Niobium *x* in the crystal. Phase transition temperatures for the tetragonal to cubic transition (T^{tc}) and from the orthorhombic to tetragonal phase (T^{ot}) can be described by following formulas:

$$T^{tc}/°C = 682*x-261,$$
$$T^{ot}/°C = 426*x-224$$

where *x* is the concentration of Niobium.

Most of the transparent, colorless $KTa_{1-x}Nb_xO_3$ single crystals (x = 0.004, 0.007, 0.012, 0.07, 0.3) used in our investigations were grown at the Oak Ridge National Laboratory and A.F. Ioffe Physical-Technical Institute by solidification from nonstoichiometric melt of high purity (99.999 %) Ta_2O_5, K_2CO_3 and Nb_2O_5 starting materials as it was described in [90]. The Nb content inside of the experimental specimens was determined by electron microprobe analysis and dielectric permittivity measurements (at 1KHz), comparing positions of the phase transitions points with the KTN phase diagram [91]. The specimens' conductivity at RT was in the order of 10^{-13} $\Omega^{-1}cm^{-1}$. Samples were prepared as optically polished parallelepipeds with faces oriented along <100> cubic axes.

3 Spectroscopic Study of SBN Crystals

3.1 Absorption of SBN and SBN:Ce

Typical polarized absorption spectra of SBN and SBN:Ce crystals are shown in Fig. 3.1.1.

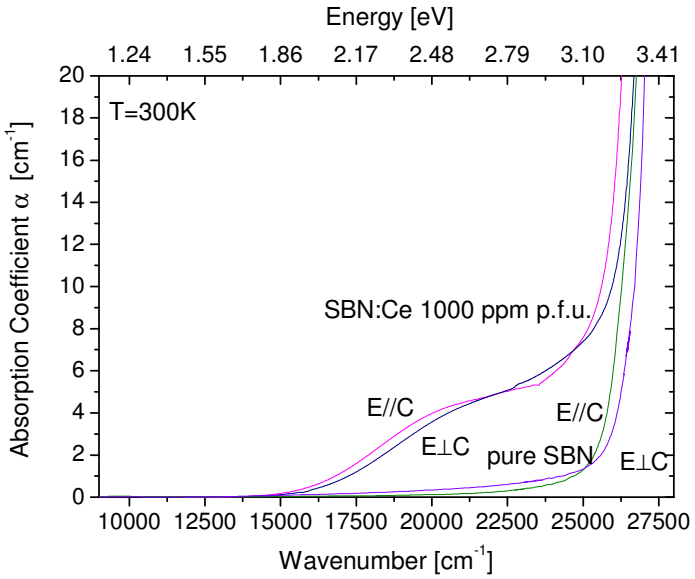

Fig. 3.1.1. Polarized Absorption spectra of congruent pure SBN and SBN:Ce at room temperature.

The UV absorption band edge of pure SBN crystals at room temperature lies at about 370 nm (3.35 eV) with a slight dichroism for extraordinary and ordinary light. In the visible region pure SBN is transparent and shows no absorption. Ce doping shifts the onset of the absorption edge to longer wavelengths and an absorption shoulder around 500 nm (2.48 eV) appears. This absorption shoulder is attributed to the 4f-5d transition of Ce^{3+} ions and in Fig 3.1.2 the absorption spectra of SBN:Ce and pure SBN is shown with different Ce doping at room temperature.

The absorption coefficients in the visible region (at 514 nm, 2.41 eV) for SBN single crystals increase linearly with the Ce (up to ~20000 ppm., p.f.u.) concentration (Fig. 3.1.3) in agreement with data of ref. [69]. The spin-orbital and crystal field splitting of $4f^1$ level of Ce^{3+} ions is not resolved in the visible range, but this splitting exists and is shown in characteristic absorption bands in the FIR region (around 2000 cm^{-1}, 0.25 eV, Fig 3.1.4) [92, 93, 67]. Dependence of the maxima of FIR absorption in SBN:Ce on Ce concentrations is shown in fig 3.1.5 and earlier was described by Greten in [94]. The integral FIR absorption of the Ce^{3+} band near 2000 cm^{-1} (0.25 eV) also varies linearly with the Ce concentration in the crystal (Fig. 3.1.6) at least till 20000 ppm p.f.u..

Although the absorption due to the transition of Ce^{3+}: 4f-5d is strong in SBN:Ce crystals, no luminescence is observed for the de-exitation:5d-4f of Ce^{3+}. Blasse [95] discussed the

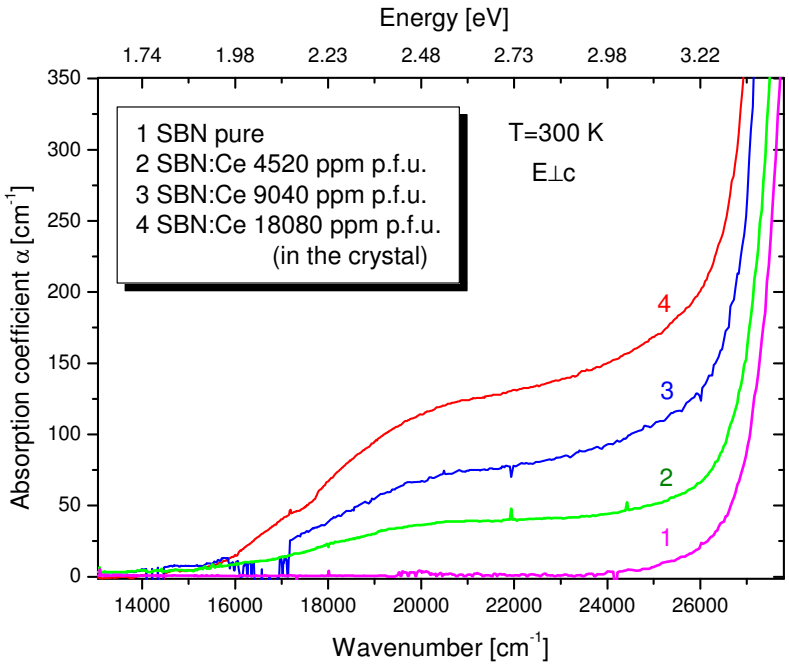

Fig.3.1.2. Absorption spectra of SBN:Ce and pure SBN with different Ce doping at room temperature.

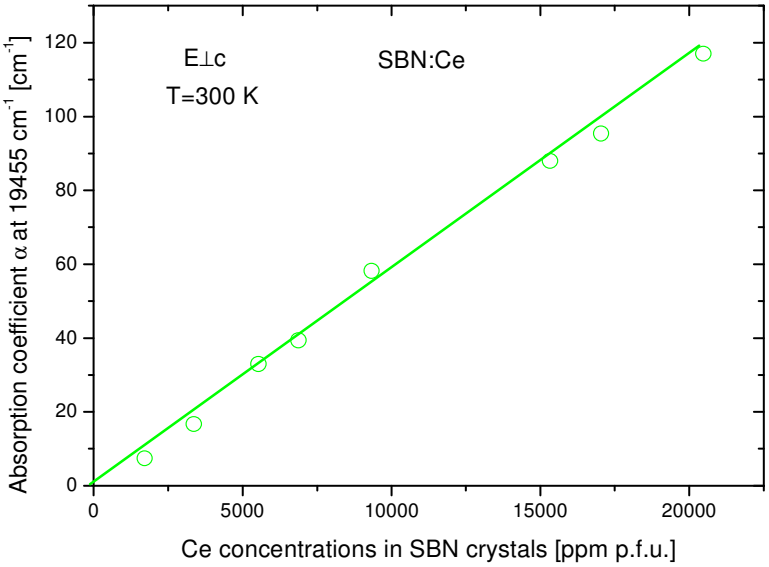

Fig.3.1.3.The absorption coefficients in SBN:Ce crystals at 19455 cm^{-1} (2.4 eV) versus Ce concentrations in the crystals (at room temperature).

quenching of the luminescence of Ce^{3+} in detail and proposed that Ce^{3+} may be expected to yield luminescence in host materials which have the optical absorption edge in the far ultraviolet

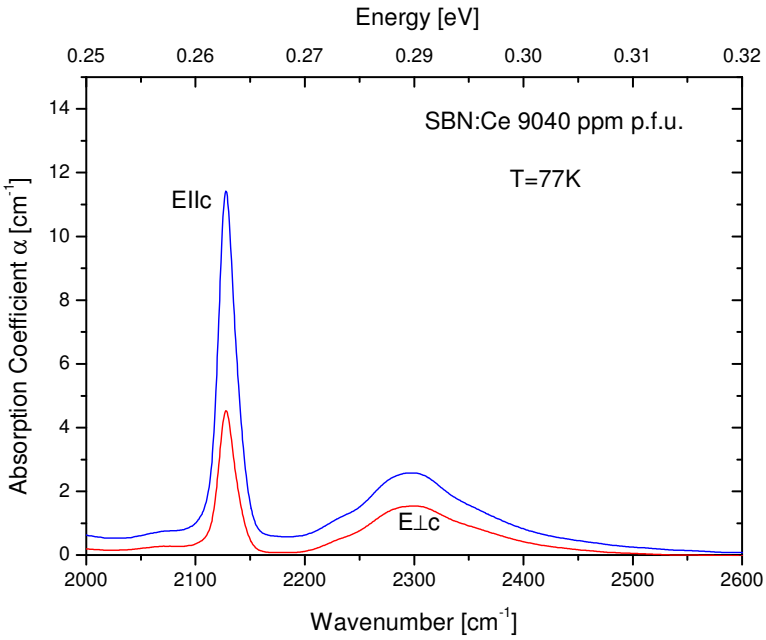

Fig.3.1.4. FIR absorption of Ce^{3+} in SBN:Ce (9040 ppm p.f.u.) crystal.

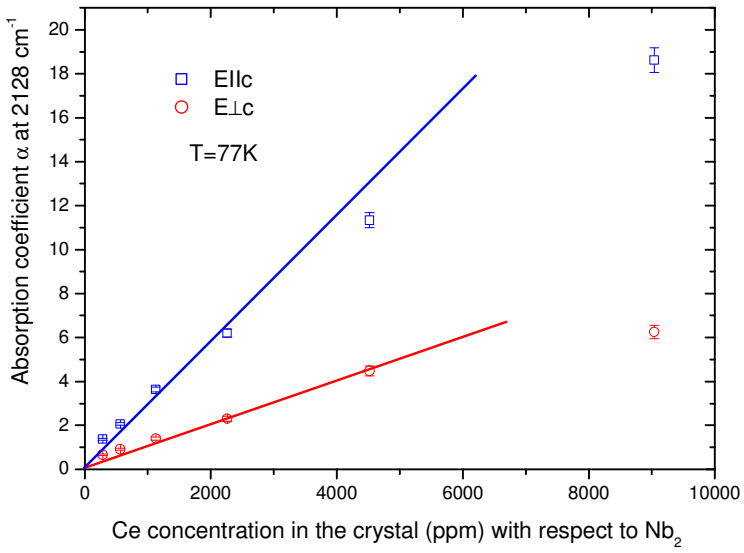

Fig.3.1.5.Dependence of the maximum (2128 cm^{-1}, 0.26 eV) of FIR absorption (see Fig. 3.1.4) in SBN:Ce on Ce concentrations [94].

and the quenching by electron transfer could rapidly eliminate the luminescence of Ce^{3+} if the optical absorption edge of the host materials shifts to the low energy side. The absorption band of Ce^{3+} in the SBN:Ce crystals is very close to the absorption edge, suggesting the first

excited state $5d^1$ of Ce^{3+} lies near the bottom of the conduction band or inside the conduction band. In this case an electron transfer transition from the ground state $4f^1$ of the Ce^{3+} to the conduction band (4d orbital of Nb^{5+}) becomes possible, quenching the luminescence of Ce^{3+}.

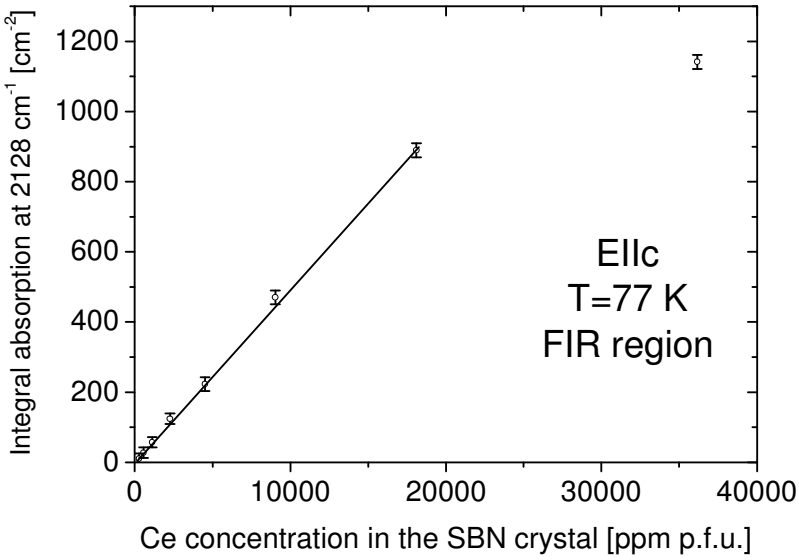

Fig.3.1.6.The integral FIR-absorption of Ce^{3+}-ions (with maximum at 2128 cm^{-1}, 0.26 eV) versus Ce concentrations in the SBN:Ce crystal.

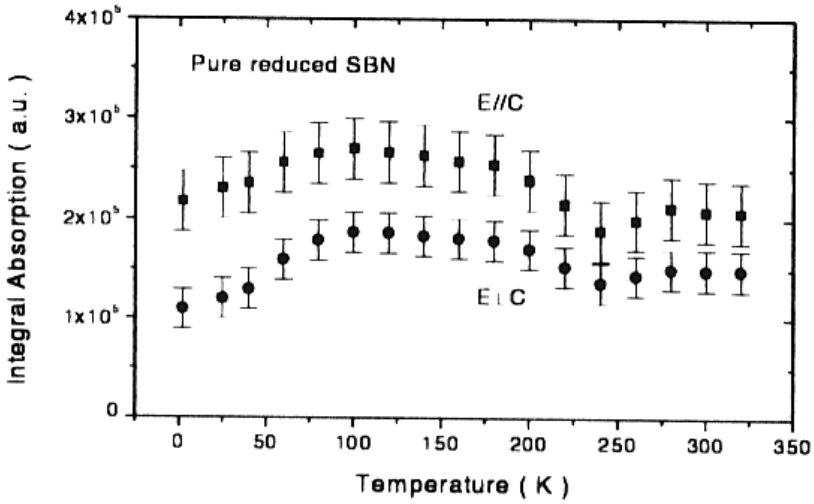

Fig. 3.1.7. Temperature dependence of the integral absorption intensity from 0.3 eV to 1.3 eV in a pure reduced SBN crystal.

After reduction treatment the pure SBN crystals shows a broad NIR absorption band whose peak is located at ~0.75 eV, no other absorption band due to the reduction treatment is observed [96]. This Nb^{4+} polaron absorption extends from the IR spectral region to the visible region, giving rise to the absorption change in the visible region after reduction and this is in agreement with data of ref. [96]. Fig. 3.1.7 demonstrates the temperature dependence of the

NIR absorption intensity in reduced SBN [96]. The fact that the absorption band of Nb^{4+} polaron in the reduced SBN crystals is very stable even at room temperature indicates that the total number of the Nb^{4+} polarons actually does not change in the wide temperature range and the small change as a function of temperature of the intensity of the Nb^{4+} polarons in reduced crystal most probably can be explained by a changing of the oscillator strength of the Nb^{4+} polaron. A shifting of the peak position to higher energies at low temperatures that is observed in [96] was predicted by theory [57,58].

A similar NIR absorption band is observed when SBN crystals are illuminated at low temperatures, which will be discussed later. The NIR absorption which has the same characteristic form and spectral position as observed in $LiNbO_3$:Zn, $LiNbO_3$:In and pure $LiNbO_3$ [97,98] and has been assigned to the absorption of Nb^{4+} polarons.

3.2 Light-Induced Absorption in SBN

Under illumination with a Ar^+-laser (λ=488 nm) or a Xenon lamp with a set of filters (400-500 nm bandpass filter) a broad light induced absorption from NIR till VIS region appears in SBN:Ce (see Fig. 3.2.1). Previously a light-induced absorption was observed in SBN:Ce at room temperature by Buse at al. [99] and at low temperatures by G. Greten [94]. At low temperatures the light-induced absorption becomes more pronounced and shows a broad polaron absorption band around 0.84 eV (6900 cm^{-1}) and a broad VIS-center absorption band near 2.03 eV (16500 cm^{-1}).

The light-induced VIS absorption can be separated with the help of temperatures at which we are taking our measurements. At higher temperatures (T>120 K), the NIR-polaron absorption is going to zero due to rapid decay but the VIS-center absorption is still present, we can perform studies of the VIS-center. The NIR Nb^{4+} polaron absorption band has been first predicted by Baetzold [100] and was described in some detail in [101]. The centers for the visible absorption, being produced simultaneously with the NIR absorption have not been identified yet and we will call it the light-induced VIS centers. The width of the light-induced VIS absorption is quite large giving evidence of the complex origin of the light-induced centers.

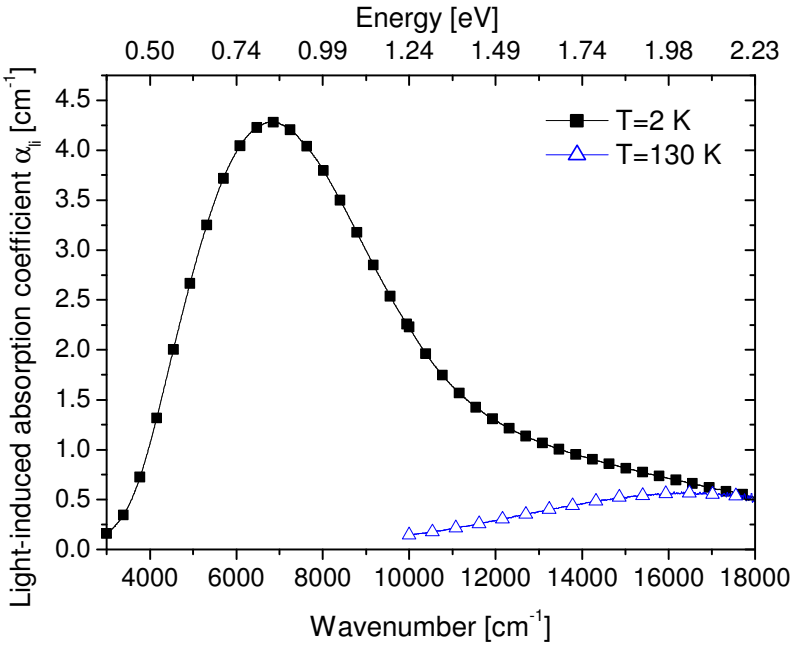

Fig. 3.2.1. Light-induced absorption under illumination with 380-480 nm light (2kW/m^2). Black dots are the absorption spectra at T=2 K (both, NIR absorption and VIS absorption), and open triangles are the absorption spectra at T=130 K, which shows the light induced absorption of VIS centers alone.

At low temperatures the NIR-polaron centers and VIS centers are very stable and show no decay in the dark Fig 3.2.2 (Explanation of the decay measurements conditions: decay of the amount of absorption (centers) in the observation window (∅ about 1 mm) in the steep exponential concentration profile generated by the illumination from the side (90º configuration), for more information see chapter 2, page 16). The slow decay of NIR polaron and VIS centers observed earlier at low temperatures (for light-induced NIR Nb^{4+} polaron absorption T<55 K, for light-induced VIS centers absorption T<170 K) is present due to the light of the Fourier spectrometer (Fig.3.2.2).

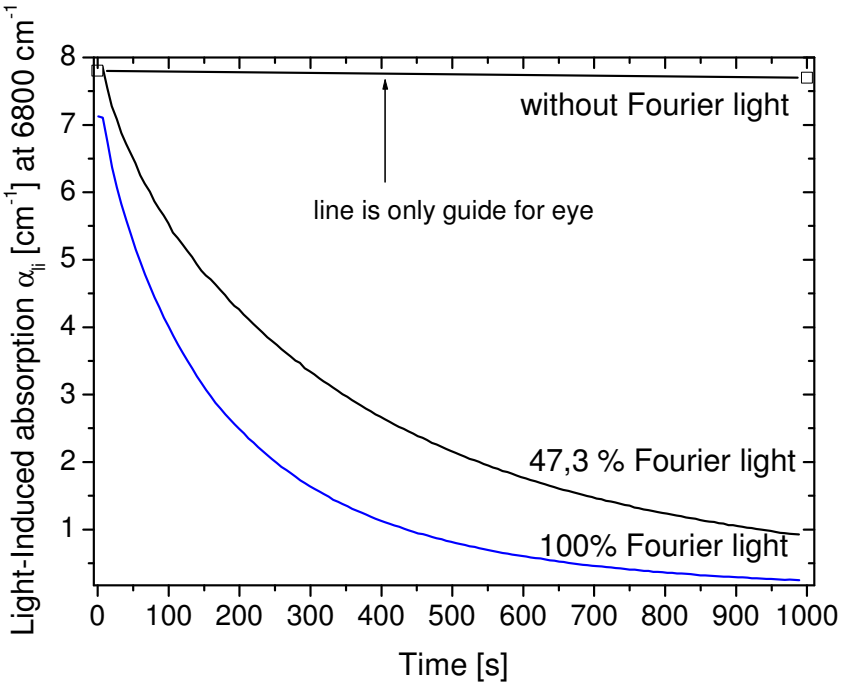

Fig.3.2.2. The light-induced NIR absorption decay after illumination with 380-480 nm light (2kW/m^2) at 2 K. Black curve is decay under 47.3% of the Fourier spectrometer light and blue is decay under 100% of the Fourier spectrometer light. Open squares are measurements only at first two seconds and at the last two seconds.

The experiment to investigate this behaviour was organised in the following way: first, we collect data about the decay of the NIR light-induced polaron absorption or VIS-center light-induced absorption in the usual way. Then under the same conditions we perform measurements only at starting and ending points, all light in time between this two measurements is turned off (Fourier spectrometer measurement light and pumping light was switched off) also we used band-pass and neutral metallic filters to reduce intensity of light of the Fourier spectrometer. At measuring points the light from the Fourier spectrometer was turned on approx. 2 sec., which could explain the slight decay that we observe even at these conditions.

Also from Fig. 3.2.2 we can conclude that the light-induced Nb^{4+} polaron absorption intensity and decay process strongly depend on the intensity of the Fourier spectrometer light (when other parameters like temperature and pumping light are constants).
As the temperature is going lower than 120 K both, the light induced Nb^{4+} polaron absorption and the light-induced VIS absorption appears (see Fig 3.2.1). We found that the influence of the Fourier light is higher for the NIR light-induced Nb^{4+} polaron absorption than for the VIS centers. In this case we can study the Nb^{4+} polarons separately from the VIS centers via using different temperatures, at which we are working. At low temperatures VIS centers are almost frozen, and we can study the Nb^{4+} polarons. At higher temperatures like 140 K the NIR centers are already gone by thermally activated decay, but the VIS centers are still present.

NIR Nb^{4+} Electronic Polarons

According to polaron theory [102], the binding energy of the Nb^{4+} polaron in SBN crystals is about 0.36 eV and the thermal hopping energy is about 0.18-0.19 eV. At 2 K under immersion in superfluid helium, the illumination intensity dependence of the Nb^{4+} polaron absorption in the SBN:Ce crystal is shown in Fig. 3.2.3. The absorption coefficient α_{li} of Nb^{4+} polarons at the peak position is proportional to the concentration n_p of the polarons, and can be described by Smakula's formula:

$$\alpha_{li} = A \cdot \frac{f}{w} \cdot n_p \qquad (3.2.4)$$

where A is a constant, w is the full width at the half-maximum of the absorption band, f is the oscillator strength of the optical transition. At a fixed temperature, the oscillator strength f and the full band width w in above equation are constants, which means $\alpha_{li} \propto n_p$.

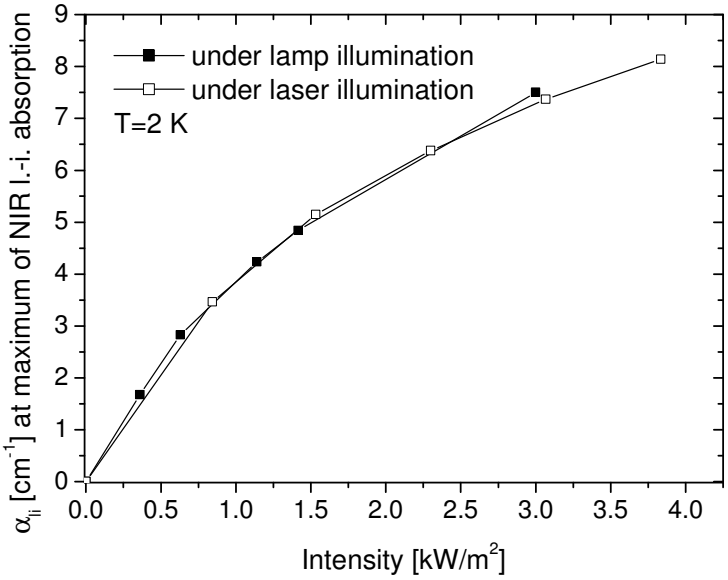

Fig.3.2.3. Intensity dependence of light-induced NIR absorption. Illumination with 380-480 nm light or argon laser (λ = 488 nm) was used. The same broadband power meter measured intensities of the XBO lamp and argon laser.

Even at small illumination intensities there exists a sizable light-induced effect and we can resolve it even more if we will reduce the Fourier light intensity (see Fig. 3.2.2). The dependence between light-induced absorption and illumination intensity is obviously nonlinear.

The temperature dependence of the light-induced Nb^{4+} polaron absorption is shown in Fig. 3.2.5. We can conclude that for the light-induced Nb^{4+} polaron centers the concentration is changing only a little (in analogy to the Nb^{4+} polaron absorption in reduced SBN crystals) in the range of 1.3-50 K and perhaps the slight increase in the absorption with increasing temperature can be explained by a variation of the oscillator strength because in the reduced samples we see the same increasing of the absorption in this temperature region (see Fig. 3.1.7, page 34). When the temperature is going higher than 50 K the light-induced Nb^{4+} polaron absorption start to decay rapidly and the concentration of the centers decreases. The decay process is found to be non-monoexponential and the temperature dependence is shown in Fig. 3.2.6.

Normalized decay curves are shown in Fig. 3.2.7 (in this case decay constants are different because the Fourier light intensity and the spectral distribution were different). Also we should take into account that from 1.4 till 40 K the decay process is changing somewhat and it is going to be longer with increasing temperature. The temperature dependence of the light – induced absorption steady state values and the decay processes indicate that the thermal activation of the light-induced Nb^{4+} polaron centers is playing a dominant role in the region of 50-120 K. The decay at low temperatures is very small and present practically only due to the Fourier light.

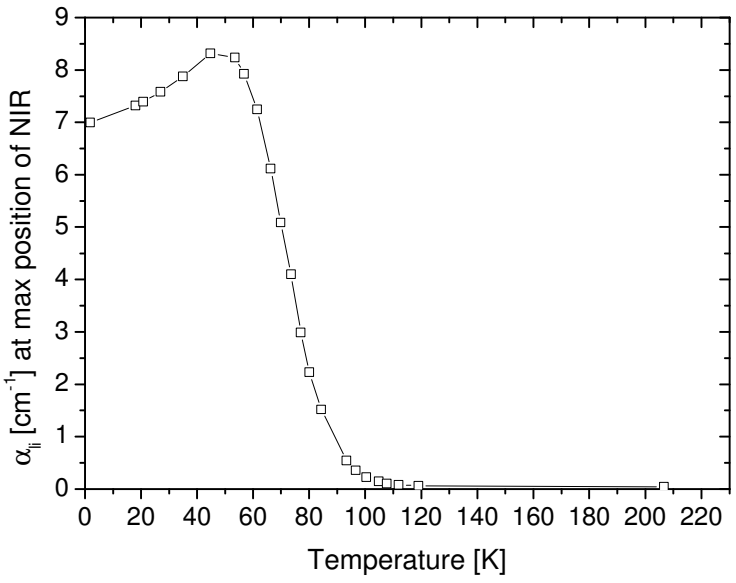

Fig.3.2.5. Temperature dependence of the light-induced NIR absorption under constant illumination with 380-480 nm light (2kW/m^2). Solid line is guide for eyes.

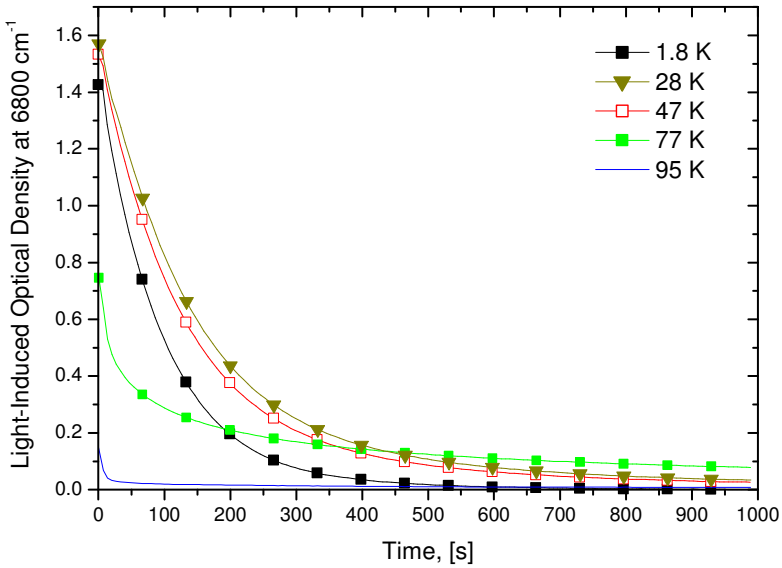

Fig.3.2.6. The light-induced NIR absorption decay at several temperatures after illumination with 380-480 nm light (2kW/m^2, small FTIR light intensity with narrow spectral distribution).

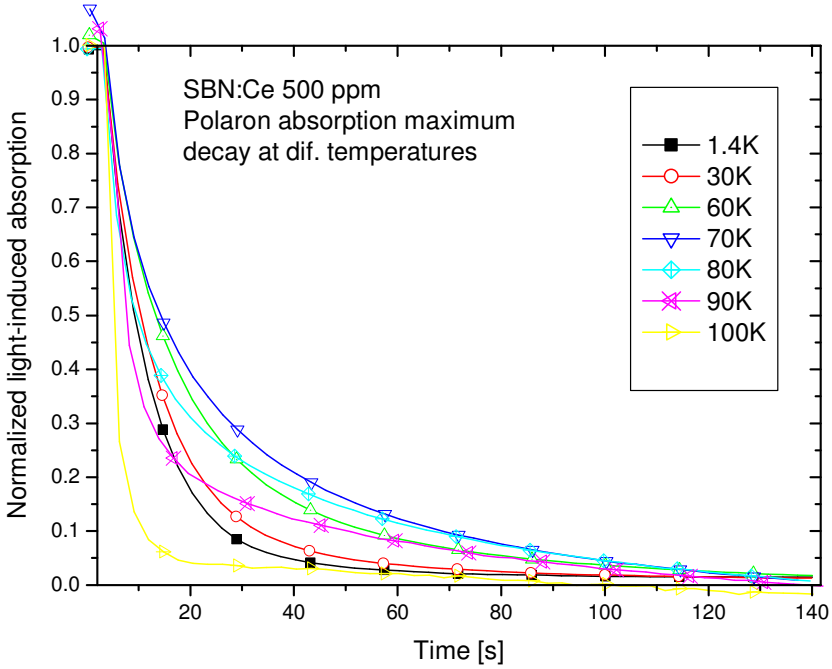

Fig. 3.2.7. The normalized light-induced Nb^{4+} polaron absorption for SBN:Ce crystal (high FTIR light intensity with wide spectral distribution).

The VIS Center

The temperature dependence of the light-induced VIS absorption (see Fig. 3.2.8) shows a behaviour comparable with the temperature dependence for the light-induced NIR Nb^{4+} polaron absorption. From low temperatures till about 160 K the concentration of VIS centers is changing very little but above 160 K it starts to decay rapidly. The decay process is also non-monoexponential and at low temperatures it is slow (and present only due to Fourier light, see Fig. 3.2.9) and becomes faster with increasing temperature, similar to Nb^{4+} polaron behaviour. It indicates also that the thermal activation of the VIS center plays a dominant role in the decay process at higher temperatures (160-300 K).

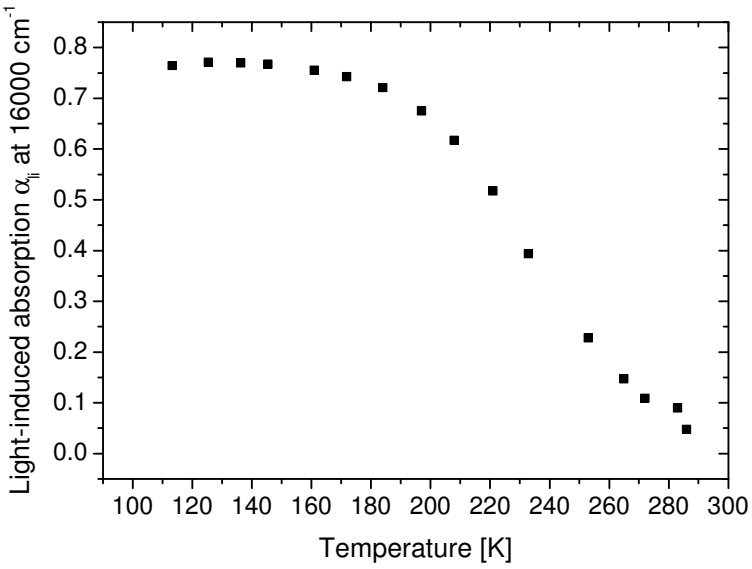

Fig.3.2.8. Temperature dependence of the light-induced VIS absorption under constant illumination with 380-480 nm light (2kW/m^2) and constant Fourier measurement conditions.

The peak position and the FWHM of the absorption band vary little with temperature below 130 K. In Fig. 3.2.10 the experiment is shown when we tried to form more VIS centers during the NIR polaron decay. We did the following: first, we created polarons and VIS centers at low temperatures, switched off every light sources (and pumping light, and light of Fourier spectrometer), second, we heated up the sample to 120 K and waited ca. 30 sec. to let the polarons decay; third, we were taking spectra of the VIS absorption left in the sample and compared it with the measurements before.

From this experiment we can conclude that no further VIS centers are created during thermal activated decay of the light-induced Nb^{4+} polarons.

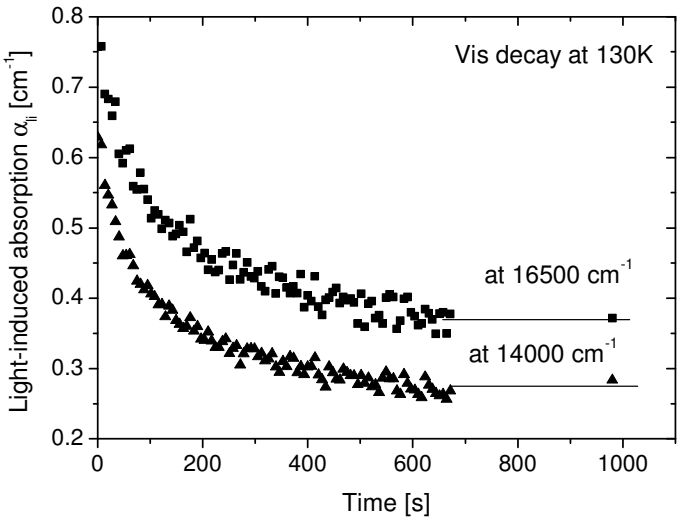

Fig.3.2.9. The VIS light-induced absorption decay after illumination with 380-480 nm light ($2kW/m^2$) at 130 K. The decay is first under continuous Fourier spectrometer light till 680 s., then the decay is in the dark and then a measurement only at the last point (1000 sec.) is done.

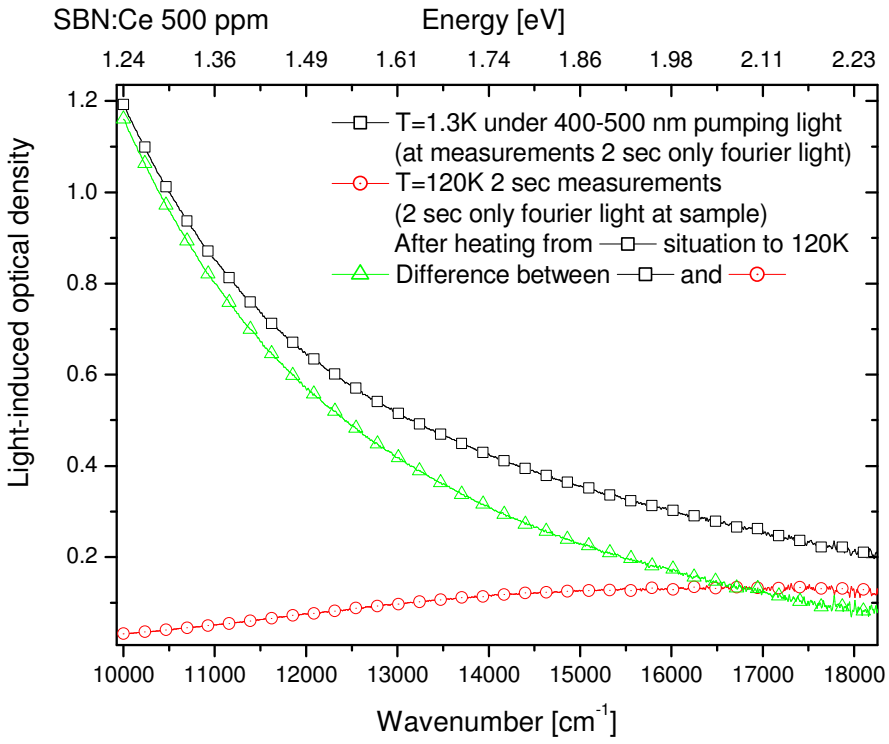

Fig. 3.2.10. Light-induced NIR- and VIS- absorption.

3.3 Light-Induced Dissociation of the VIS-Centers in SBN:Ce Crystals.

Under illumination at low temperatures one will create VIS and NIR centers simultaneously. Then, can wait till the NIR centers will decay under Fourier light illumination. The VIS center absorption will remain. If we then illuminate with light in the region of VIS centers absorption, we will find that the VIS absorption will decrease and simultaneously a NIR transient absorption will appear. As we can see from the Fig. 3.3.1 when we are switching on the Kr^+-laser the Nb^{4+} polaron absorption appears. If we will switch off the laser light, the Nb^{4+} polaron absorption will decay with its usual time constant as in previous experiments (depending on the Fourier light intensity and frequency distribution).

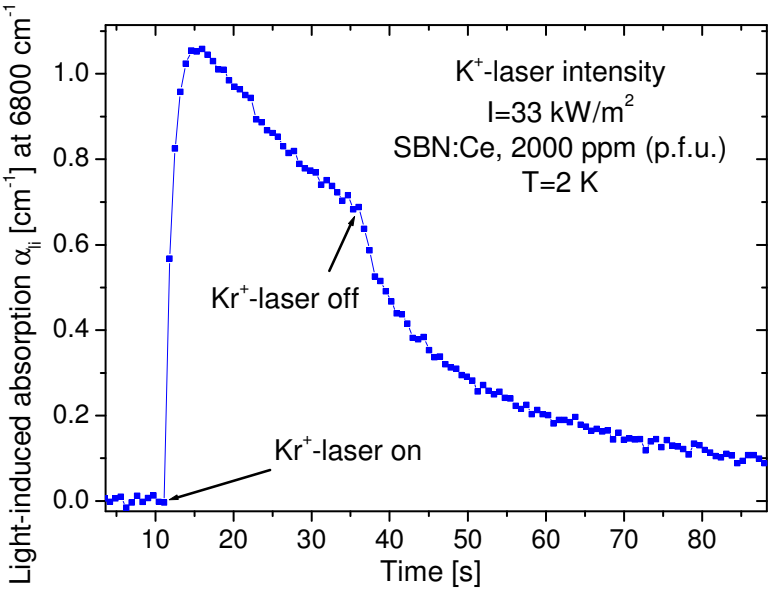

Fig.3.3.1. Transient NIR Nb^{4+} polaron absorption at 6800 cm^{-1}, which appears upon illumination in the VIS absorption maximum.

Variations of the decay processes with different Kr^+-laser intensities are shown in Fig. 3.3.2. We can conclude that under not so high illumination intensities the decay process is going in similar way, but at higher intensities of Kr^+-laser probably all of the VIS centers are dissociating within the first 10 seconds and that's why we see usual decay curve for polaron absorption after switching off pumping illumination. Earlier it was shown by Ming Gao [96] that no light-induced absorption exist under illumination with Kr^+-laser alone in SBN:Ce crystals. Dissociation of the VIS centers to NIR centers under illumination with red Kr^+ laser light or with red laser diode light lead us to conclude that at least one part of the dissociation process are NIR Nb^{4+} polaron centers.

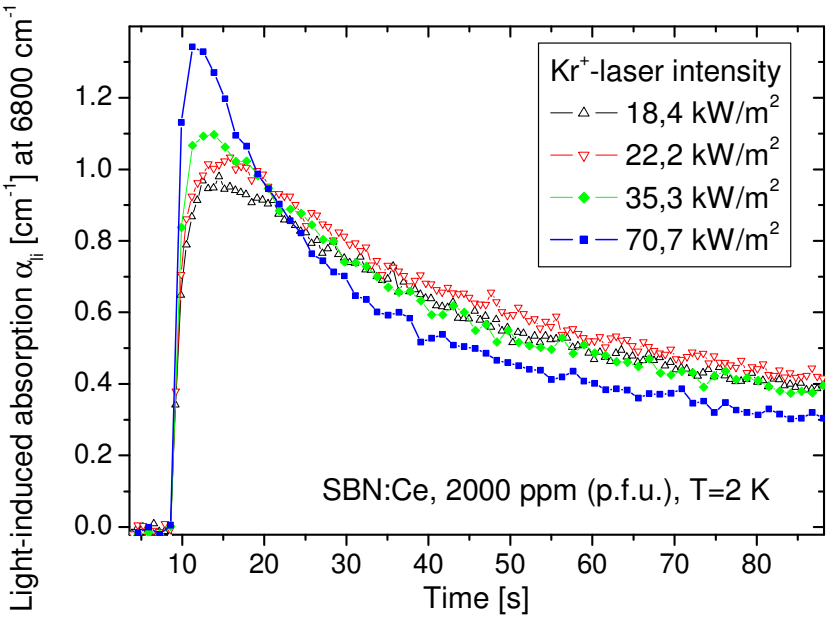

Fig.3.3.2. Dissociation of the VIS centers to the NIR centers. First, we create light-induced absorption and wait till polarons decay completely. Then, we are switching on the Kr^+ laser and measure the light-induced absorption at the polaron absorption maximum position for several Kr^+ laser light intensities.

3.4 Light-Induced Charge Transport Process

SBN crystals belong to the class of oxygen-octahedra ferroelectric crystals. The highest filled valence band in niobate crystals [103] is based on oxygen $2p\pi$ orbitals, which interact through ligand-metal π bonding with the $d\varepsilon$ orbitals of Nb^{5+}. The conduction band is based on the dε orbitals of Nb^{5+}, which is empty in a perfect crystal.

The interband transition of SBN crystals comes from the electron transition from $2p\pi$ orbitals of oxygen to the $d\varepsilon$ orbitals of Nb^{5+} ions and the bandgap is about 3.36 eV (370 nm, from calculations for pure ionic type of bonding the bandgap should be 15 eV, but if one will take into account covalent bonding, one will get a more reasonable value, which will be close to experimental one). From the absorption spectra of SBN:Ce we can conclude that the ground state of Ce^{3+} lies in the bandgap of SBN crystal and the first excited state of Ce^{3+} lies close to or higher than the bottom of the conduction band. Under illumination with a suitable wavelength an intervalence transition 4f (Ce^{3+}) - 4d (Nb^{5+}) occurs.

The electrons in the conduction band can be trapped by their self-induced potential well by electron-lattice coupling interaction and form Nb^{4+} polarons. The illumination of pure SBN crystals with Ar^+ (λ = 488 nm) or Kr^+ lasers (λ = 647 nm) cannot create observable Nb^{4+} polaron absorption because the photon energy is not sufficient to excite an electron from the valence band to the conduction band. However, the illumination with UV light (at low temperatures) indeed generates Nb^{4+} polarons in pure SBN crystals. The reduction of pure and doped SBN crystals induces Nb^{4+} polarons with a similar absorption band in the NIR region [96].

Laser beam coupling experiments in SBN crystals [94,104] indicate that electrons are the dominant photoexcited charge carriers in the light-induced charge transport process even at low temperature. Ce^{3+} is introduced to act as electron donor. Therefore, the concentration of Ce^{3+} in SBN crystals decreases under appropriate illumination at low temperature.

At room temperature light-induced Nb^{4+} polarons and the VIS centers are thermally unstable because of the fast decay rates of the two trapping centers. The light-induced charge transport process in doped SBN crystals can be represented by a simple intervalence transition of the electron from Ce^{3+} ion to Nb^{5+} ion [100]. At 110 K<T<RT, the light-induced VIS trapping centers tend to participate in the light-induced charge transport process. The appearance of this center does not depend on dopants and therefore points to an intrinsic center. Below T=110 K the light-induced Nb^{4+} polaron plays a crucial role in the light-induced process.

One important point, which should be noted, is that probably most Nb^{4+} polarons are formed close to the Ce^{4+} or O^- from where the electrons are originating. In other words, electrons photoexited from Ce^{3+} or O^{2-} to Nb^{5+} ions will be trapped, resulting in the Nb^{4+} polarons at low temperatures. The electrons trapped in Nb^{4+} polarons can in principle transit the potential barrier between Nb^{4+} polarons and Ce^{4+}/O^- ions by tunneling, photon-assisted tunneling, and hopping motion or with the help of Fourier light absorption.

At superfluid helium temperatures the hopping motion of the Nb^{4+} polarons is absent and only tunneling and/or motion due to Fourier light still exists. From our experiments we can

conclude that no recognizable tunneling exists in our case, this means that at low temperatures decay process only consists from the Fourier light-induced part with a time constant >>1 hour. Above 50 K the phonon assisted hopping motion tends to contribute to the decay process and therefore we get a faster decay process with increasing temperature.

Baetzold's light-induced charge transport model [100] in doped SBN crystals considered the role of Ce^{3+}/Ce^{4+} and Nb^{4+} polarons but neglected the active role of the VIS centers. As shown above, the VIS center plays a crucial role in trapping electrons especially at higher temperatures (T > 110 K). In the following two sections we will discuss the light-induced charge transport process in SBN crystals quantitatively at T > 110K and T < 110K, and will discuss the possible nature for the light-induced VIS centers in SBN.

3.4.1 VIS Centers

The absorption coefficient α_{li} of Nb^{4+} polarons or VIS-center at peak position is proportional to the concentration n_p of the polarons or VIS-centers, and can be described by Smakula's formula:

$$\alpha_{li} = A \cdot \frac{f}{w} \cdot n_p \qquad (3.4.1.1)$$

where *A* is a constant, *w* is the full width at the half-maximum of the absorption band, *f* is the oscillator strength of the optical transition. Since the concentration of Nb^{4+} polarons is too small to be observed above T=110 K, the VIS-center becomes the dominant trapping center of electrons in the range 110 K - RT.

Our model first will focus on the calculation of the concentration of VIS-centers in the steady state under illumination. Electrons are found to be the main charge carriers in the light-induced charge transport process of doped SBN crystals [94,104], so in a first approach we only consider the behavior of electrons and neglect the role of holes in the valence band.

Also, the light-induced absorption change due to the decrease of the concentration of Ce^{3+} is much smaller than the absorption of the VIS centers at the peak position of the VIS-center absorption band, so it is omitted in the following discussion. Two centers are taken into account between the conduction band and the valence band: Ce^{3+} is the main charge state in SBN:Ce [68] and serves as the electron donor under illumination; the VIS-center lies close to the conduction band, acting as thermally-activated trapping center. The bulk photovoltaic effect is found to be negligible in the light-induced charge transport process of SBN [99]. The light-induced charge transport model is illustrated in Fig. 3.4.1.2.

Under illumination with the laser or XBO lamp with set of filters (380-480 nm) Ce^{3+} ions are partly photo-ionized and the electrons are excited from Ce^{3+} to the conduction band. The lifetime of the electrons in the conduction band is very short and some of them will be trapped in VIS-centers. At the same time some free electrons in the conduction band will recombine with Ce^{4+} ions. The electrons trapped in the VIS-center can be thermally excited to the conduction band or due to thermally excited hopping motion move on and recombine with Ce^{4+} ions or other traps (like Fe unavoidable impurities), defects in ideal crystal structure e.t.c.

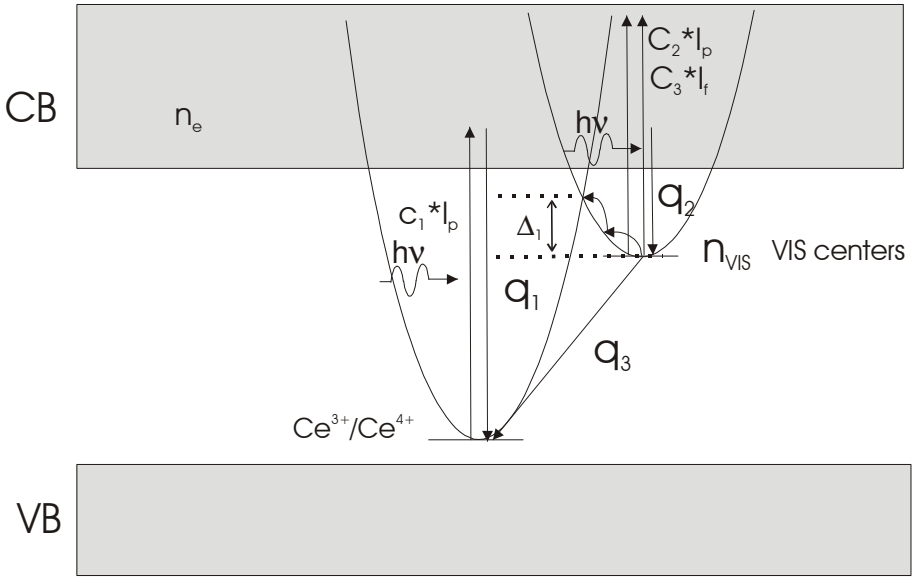

Fig. 3.4.1.2 The light-induced charge transport process in SBN:Ce at T>110 K.

Additionally, as the VIS-center absorption band lies in the visible region, electrons from the VIS center can be excited by photons of pumping light (Ar^+ laser, λ = 488 nm, or XBO lamp, λ=380-480 nm) or by Fourier light, which is used to measure the absorption spectrum. The rate equations are:

$$\frac{d}{dt}n_e = c_1 \cdot I_p + c_2 \cdot I_p \cdot n_{VIS} - q_1 \cdot n_e + c_3 \cdot I_f \cdot n_{VIS} - q_2 \cdot n_e$$
$$\frac{d}{dt}n_{VIS} = q_2 \cdot n_e - c_2 \cdot I_p \cdot n_{VIS} - I_f \cdot c_3 \cdot n_{VIS} - q_3 \cdot n_{VIS} \qquad (3.4.1.3)$$

where n_e is the electron concentration in the CB; n_{vis} is the VIS-center concentration; I_p is the pumping light illumination intensity; c_1 is related to the probability to absorb one photon and form a free electron in the CB; c_2 and c_3 are constants relating to the quantum yield for absorption of one photon and the absorption cross section of the VIS-center for pumping illumination and Fourier spectrometer light; q_1 is the probability for recombination of the electron in the CB with the Ce^{4+} ion; q_2 is the probability of the VIS-center to trap one electron; q_3 is the probability of the electron in the VIS-center to vanish from its potential well by thermally activated hopping or recombination with a Ce^{4+} ion.

In the steady state $dn_e/dt=0$ and $dn_{vis}/dt=0$. From (3.4.1.3) for steady state one can get the following solution:

$$n_{VIS} = \frac{\frac{q_2}{q_1} \cdot c_1 \cdot I_p}{c_2 \cdot I_p + c_3 \cdot I_f + q_3 \cdot \left(1 + \frac{q_2}{q_1}\right)} \qquad (3.4.1.4)$$

$$q_3 = q_{30} + q_{31} \cdot \exp\left(\frac{-\Delta}{kT}\right) \qquad (3.4.1.5)$$

The first term in Eq. (3.4.1.5) represents the direct resonance tunneling effect and the second term comes from hopping over the potential barrier. Δ is the effective thermal activation energy of the VIS center. From our measurements of the light-induced VIS center absorption in SBN:Ce we can exclude any decay process in the dark at least for one hour (when pumping light and Fourier spectrometer light is turned off). We therefore can set q_{30} equal to zero in this case. The general dependence on the illumination intensity, Fourier light intensity and temperature is reflected in equation (3.4.1.4).

According to equation 3.4.1.1, four parameters, α_{li}, w, n_p and f are temperature dependent. If w and f vary only little with the temperature, n_{VIS} will be proportional to the α_{li}. The temperature dependence fitting result is shown in Fig. 3.4.1.6. The fitting of Eq. 3.4.1.4 to the experimental results gives us the estimation of the thermal activation energy of the VIS-center equal to 0.23±0.04 eV.

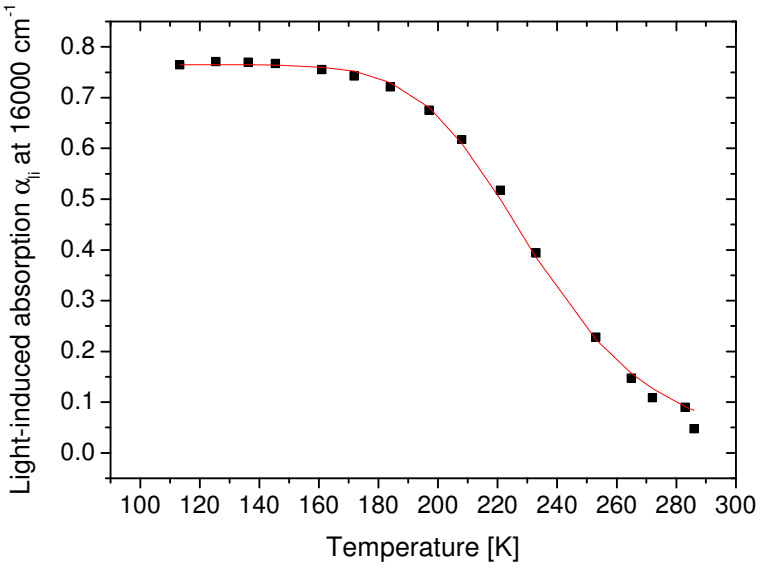

Fig.3.4.1.6. Temperature dependence of the maximum of the light-induced VIS absorption under constant illumination with 380-480 nm light (2kW/m^2) and constant Fourier measurement conditions (closed squares). Solid line is the fitting result with Eq. 3.4.1.4. From the model parameters one can get a thermal activation energy for the VIS-center of Δ=0.23±0.04 eV.

3.4.2 Nb^{4+} Polaron

At temperatures lower than 110 K, Nb^{4+} polarons also serve as trapping centers besides the VIS-centers discussed above. Under illumination with the laser or XBO lamp with set of filters (λ = 380-480 nm) Ce^{3+} ions are partly photo-ionized and the electrons are excited from Ce^{3+} to the conduction band. Due to the strong interaction of electrons and the lattice, some of them will be trapped by Nb^{5+} ions to form the Nb^{4+} polarons and some will recombine. The electron trapped in Nb^{4+} polarons can be released and can subsequently recombine by tunneling or hopping the potential barrier for the Nb^{4+} polaron potential well with the help of phonons. Since the absorption band of the Nb^{4+} polarons extends from the IR region to the visible region, the electrons could also be excited by the illumination from the Nb^{4+} polarons to the CB as well.

With this simplified model shown in Fig.3.4.2.1 we can attempt to describe the light-induced charge transport process in SBN:Ce at T < 110 K. In this simplified charge transport model the Nb^{4+} polarons serve as the major electron trapping center and the role of the VIS center is neglected. The rate equations are similar to VIS center model, with slight differences:

$$\begin{aligned} \frac{d}{dt} n_e &= c_1 \cdot I_p + c_2 \cdot I_p \cdot n_p - q_1 \cdot n_e + c_3 \cdot I_f \cdot n_p - q_2 \cdot n_e \\ \frac{d}{dt} n_p &= q_2 \cdot n_e - c_2 \cdot I_p \cdot n_p - I_f \cdot c_3 \cdot n_p - q_3 \cdot n_p \end{aligned} \qquad (3.4.2.2)$$

where n_e is the electron concentration in the CB; n_p is the Nb^{4+} polaron concentration; I_p is the pumping illumination intensity; c_1 is related to the probability to absorb one photon and form a free electron in the CB; c_2 and c_3 are constants relating to the quantum yield for absorption of one photon and the absorption cross section of the Nb^{4+} polarons for pumping light and Fourier spectrometer light; q_1 is the probability for recombination of the electron in the CB with Ce^{4+}; q_2 is the probability of the Nb^{5+} ions to trap one electron and form one Nb^{4+} polaron; q_3 is the probability of the electron in the Nb^{4+} polaron to vanish from its potential well by thermally activated hopping or recombination with a hole. In the steady state $dn_e/dt=0$ and $dn_p/dt=0$. From Eq. (8.4.2.2) for steady state one can get the following solution:

$$n_p = \frac{\frac{q_2}{q_1} \cdot c_1 \cdot I_p}{c_2 \cdot I_p + c_3 \cdot I_f + q_3 \cdot \left(1 + \frac{q_2}{q_1}\right)} \qquad (3.4.2.3)$$

$$q_3 = q_{30} + q_{31} \cdot \exp\left(\frac{-\Delta}{kT}\right) \qquad (3.4.2.4)$$

The first term in Eq.(3.4.2.4) represents the direct resonance tunneling effect and the second term comes from hopping over the potential barrier. Δ is the effective thermal energy depth of

the Nb^{4+} polaron. From our measurements of the light-induced Nb^{4+} polaron absorption in SBN:Ce we can exclude any decay process in the dark (when pumping light and Fourier spectrometer light is turned off, see Fig. 3.2.2, page 37). We therefore can set q_{30} equal to zero in this case. The general dependence on

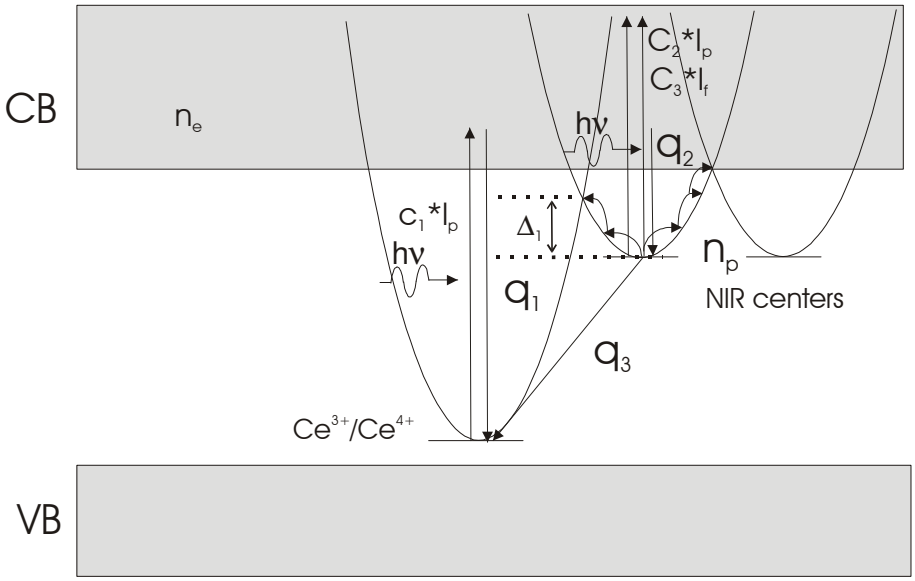

Fig. 3.4.2.1 The light-induced charge transport process in SBN:Ce crystal at T<110 K.

the illumination intensity, Fourier light intensity and temperature is reflected in equation (3.4.2.3). According to equation 3.4.1.1, four parameters, α_{li}, w, n_p and f are temperature dependent. If w and f vary only little with the temperature, n_p will be proportional to the α_{li}. When the laser is switched off (I_p=0), n_p will decay with time t. Solving equations 3.4.2.2 with assumption that we can use the adiabatic approximation [105] (n_e<<n_p), one can get the direct solution:

$$n_p=t_3\cdot((t_2+1/2\cdot t_1+q_1+q_2)\cdot\exp((t_2+1/2\cdot t_1)\cdot t)-(t_2-1/2\cdot t_1+q_1+q_2)\cdot\exp((t_2-1/2\cdot t_1)\cdot t))/c_3/I_f$$

where

(3.4.2.5)

$$t_1=(q_2^2+q_1^2+c_3^2\cdot I_f^2+q_3^2+2\cdot q_2\cdot q_1+2\cdot c_3\cdot I_f\cdot q_2-2\cdot q_2\cdot q_3-2\cdot q_1\cdot c_3\cdot I_f-2\cdot q_1\cdot q_3+2\cdot c_3\cdot I_f\cdot q_3)^{1/2}$$
$$t_2=-1/2\cdot(q_2+q_1+c_3\cdot I_f+q_3)$$
$$t_3= np_0\cdot c_3\cdot I_f/t_1$$

The intensity dependence of the light-induced Nb^{4+} polaron absorption at 1.3 K is shown in Fig. 3.4.2.6. The solid line is the fitting result with equation 3.4.2.3, which agrees with the experimental data quite well. The temperature dependence of α_{li} is more complicated according to Smakula's formula, because three parameters w, n_p and f are functions of the temperature T. Our experimental results show that f and w depend only little on the temperature, so n_p and α_{li} share nearly the same temperature dependence as shown in Fig. 3.4.2.7. α_{li} changes a little at T< 60 K so with increasing temperature the light-induced polaron absorption is increasing, and it decreases rapidly above 60 K. Above 120 K, the

polaron absorption becomes too small to be detected if the laser intensity is intermediate, i.e. a CW laser. We use

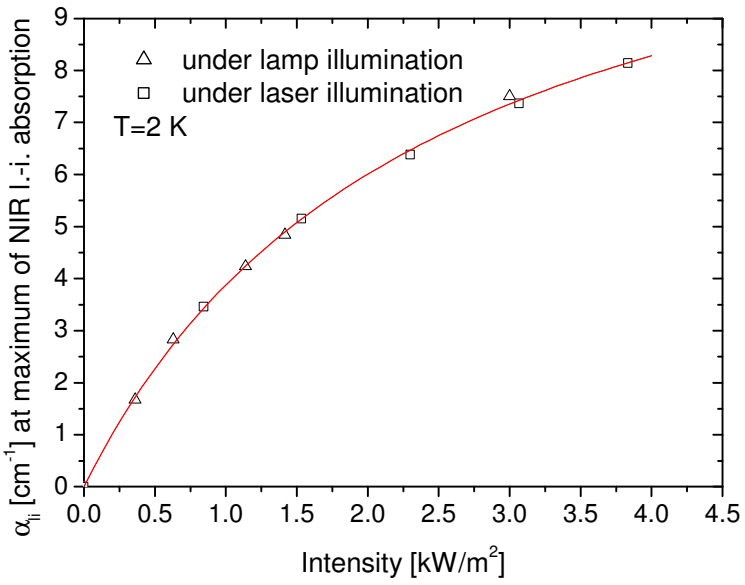

Fig.3.4.2.6. Fitting results (solid line) of the intensity dependence of the light-induced Nb^{4+} polaron absorption (open triangles). Illumination with λ=380-480 nm light or argon laser (λ=488 nm) was used. The size of the triangles and squares indicates the error bars.

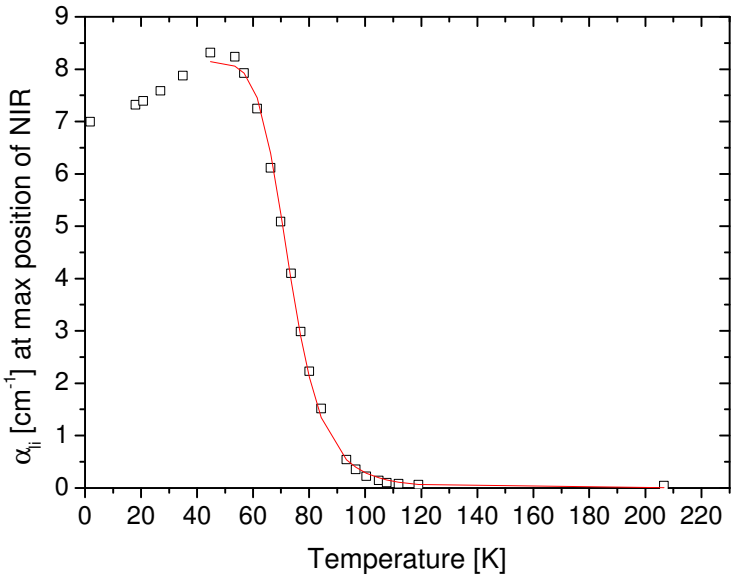

Fig.3.4.2.7 Temperature dependence of the light-induced absorption under constant illumination with 380-480 nm light (2kW/m^2). Solid line is the fitting result with Eq. 3.4.2.3. From model parameters one can get the thermal activation energy Δ=0.08±0.02 eV.

equation 3.4.2.3 to fit the experimental data (solid line). From the fitting parameter, the thermal activation energy for the polaron can be estimated to be Δ=0.08 eV.

The fitting result of the time evolution process of polarons after the laser is switched off is shown in Fig. 3.4.2.8. The theoretical calculation and experimental data are in a good agreement. If we will take in to account that the intensity of the Fourier light is much more smaller than the intensity of the pumping light, from the model and the fitting parameters we can conclude that the probability to excite one electron from the Nb^{4+} polaron to the conduction band with Fourier light is much bigger than the probability to excite one electron from Nb^{4+} polaron using pumping light. The probability of free electrons in the conduction band to form Nb^{4+} polaron is two times smaller than the probability to recombine again with a Ce^{4+} center at low temperatures.

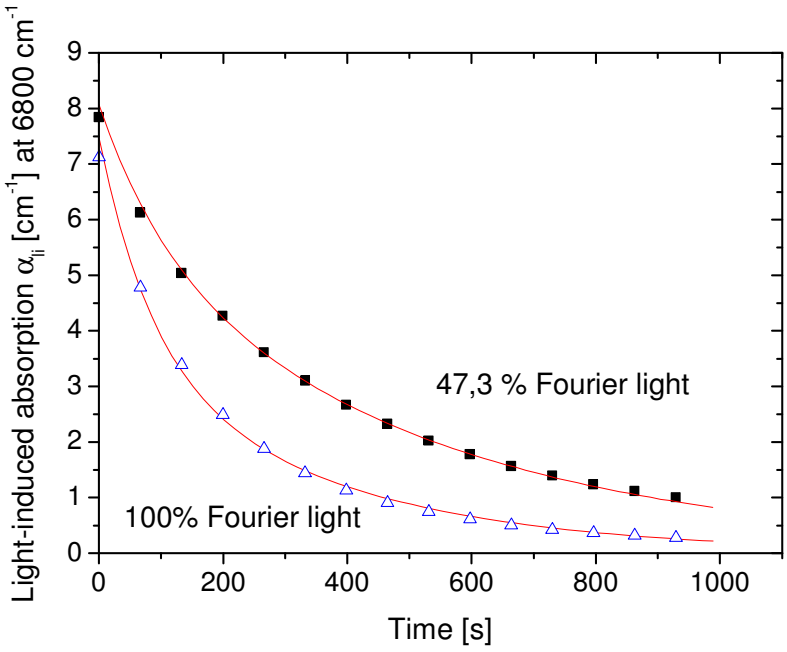

Fig.3.4.2.8. The light-induced absorption decay after illumination with λ = 380-480 nm light (2kW/m^2) at 2 K. Black squares is decay under 47.3% of the Fourier spectrometer light and open triangles is decay under 100% of the Fourier spectrometer light. The solid lines are fitting results with equation 3.4.2.5.

If we will continue to fit experimental data at different temperatures, we will see that parameters of the model are changing, but from the model by itself the light-induced polaron absorption should not change in the low temperature region (T<60 K). Perhaps the slight increasing in the light-induced polaron absorption can be explained if we will take a look again at Smakula's formula. There the oscillator strength is also temperature dependent. If we will take a look at the absorption of polarons in reduced SBN crystals we will find that in this case also a slight increase in the polaron absorption exists (see Fig. 3.1.7, page 34). In other words, we can assume that for the light-induced Nb^{4+} polarons in the SBN:Ce case the oscillator strength also changes slightly with the temperature.

3.5 Possible Nature of the VIS-Centers

Let us underline the main experimental results for the VIS-center investigation in SBN as the resume of the present work and the results published in [99,94,106,96,107,108]. These are the manifestation of the following:

a) The optical excitation and production of VIS-centers appears in a parallel way and at the same time as the production of electronic polarons in SBN.
b) A strong absorption band with a peak at 2.1 eV and with a width of about 1.4 eV is displayed by VIS centers.
c) A metastable behavior of the VIS-centers at low temperatures appears on the time scale of at least one hour.
d) Red light pumping leads to the VIS-center decay.
e) The decay products of the VIS centers contain electronic polarons.

The Model

We shall use the main features of the VIS-centers mentioned above as the background for the proposal of the VIS-center model.
The main position of the VIS-center model in SBN will be a *triad structure* related to the simultaneous bonding of *two hole polarons* and of *one electronic polaron* (Figs. 3.5.1a, 3.5.1b) [109]. It is clear that the metastable behavior could be induced here by vibronic effects on the one hand, and by taking part of electronic polarons in the strong local field of two polaronic holes on the other. Let us discuss this model in more details.

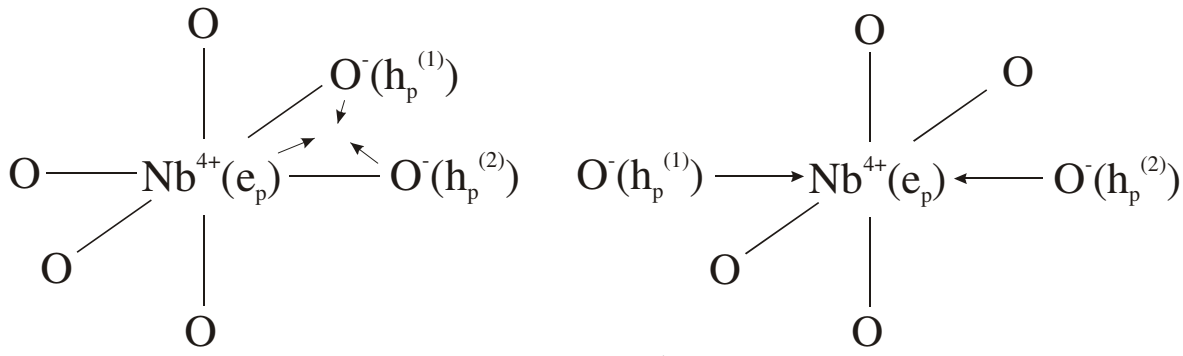

Fig.3.5.1 Co-existence of the triangle-type polaronic VIS-center (“a”) and the linear chain-type polaronic VIS-center (“b”) for “two hole polarons – one electronic polaron” cluster. Arrows correspond to the equilibrium displacements of three active ions ($Nb^{4+}(e_p)$, $O^-(h_p^{(1)})$, $O^-(h_p^{(2)})$).

Nature of the triad type polaronic formations in SBN

As metastable formation with long lifetime, which has the same conditions for optical excitation as the usual Nb^{4+} electron polarons in SBN, we will consider polaronic triad type

structures formed from two hole polarons and one electronic polaron. The presence of the three-particle "Negative-U" effect in addition to the three –particle polaronic effect is causing the realization of the deep electron and hole levels corresponding to the triad. The appearance of sufficiently deep potential wells with vibronic nature in this case will give here the metastable behavior of the triad state.

On the other hand, these triad states could be explained as states that were formed by localized charge transfer vibronic excitons (CTVE, [110,111,112]) and bi-polaron hole excitons. But first of all we should mark here, that in the perovskite-like structure two types of the triad polaronic states that consists from two hole polarons and one electron polaron exist (Fig. 3.5.1a, 3.5.1b). One of them is a triad state with triangle geometry (Fig 3.5.1a), and second is a triad state with linear type of geometry (Fig. 3.5.1b). The ratio between Coulomb forces and vibronic attraction (as the result of "Negative-U" effect) for two holes in these two geometries is different. When the attraction forces are higher, the triangle type is realized. In the other situation the linear type is taking place. For the situation in Fig. 3.5.1a a hole bipolaron is formed, but in the case of the linear type triad state the two hole polarons have no strong correlation. From Fig. 3.5.1a we can see that the triangle type of triad state could be explained as a result of hole bipolaron formation and bonding with a hole bipolaron localized CTVE on the electron polaron and one of the hole polarons, which is part of the hole bipolaron. On the other side, the linear type triad state can be discussed as two neighboring CTVE with one shared electron polaron.

The magnetic properties of the two types of triads are also different. For the triangle type of triad hole bipolaron the ground state has S=0 and the resulting spin for the triad is S=1/2. On the other side for the CTVE in the ground state S=1 and as a result for the linear type triad it should be S=3/2. But strong deformation in the equilibrium state coming from polaronic origin (including three-polaron cooperative "Negative-U" effect) for both cases is causing a strong vibronic reduction of the spin-lattice interaction. In this case the velocity of the spin-lattice relaxation is decreased. That could lead to a saturation of the ESR-absorption under usual values of the microwave power and as a result to the absence of the ESR absorption.

Properties of the Triad type polaronic states as possible states of the VIS-center in SBN

The strong deformation in the equilibrium state caused by the polaronic origin of the two types of the VIS-centers discussed give us not only energy levels deeply located in the forbidden band (Fig.3.5.2) for electron and hole polarons bonded into the triads. It also suppresses the relaxation of the VIS–center through luminescence channels. Really strong deformation that follows the formation of the VIS-center corresponds to the occurrence of an essential difference between this deformation and equilibrium deformation for the ground state (Fig.3.5.3). As a result, most effective adiabatic luminescence transitions followed by the emission of photons are forbidden. Such an absence of Franck-Condon-type luminescence transitions leads to the slow relaxation of VIS-centers. This promotes the VIS-center *metastable* behavior.

Note that the appearance of the characteristic optical absorption in the visible range could be explained for the triad VIS-center as a result of the excitation of the *light-induced* electron polaron and one of the hole polarons and a subsequent *recombination*. Two active in the light absorption Franck-Condon optical transitions for the two types of VIS-centers (shown before in Fig. 3.5.1a, 3.5.1b) is pictured in Fig. 3.5.3. The second localized hole polaron in the structure of the VIS-center is getting in a free state as a result of this recombination.

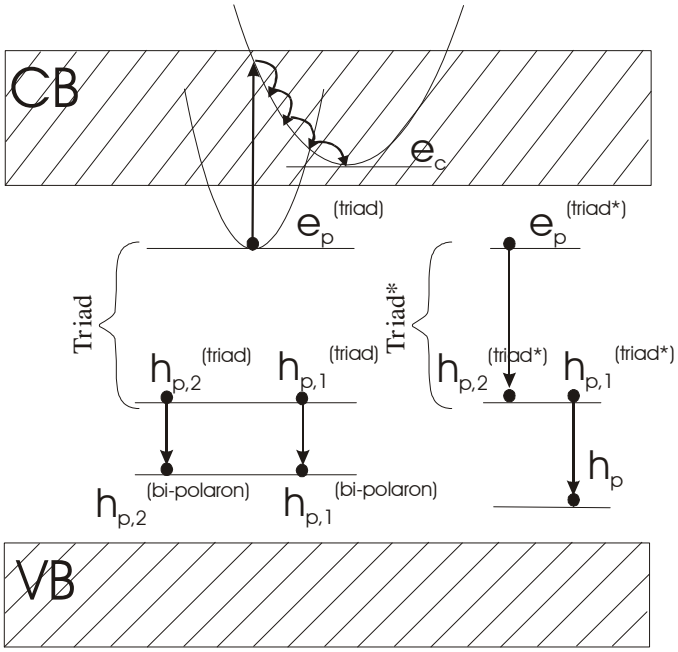

Fig. 3.5.2. Resonance up-conversion mechanism for the decay in the dark for triad polaronic center. One of the triads (at the left side) is under excitation accompanied by the appearance of a conduction electron (and the following free electronic polaron), which takes place together with a hole bi-polaron transition from triad state to the free one. Another triad is under down relaxation due to electronic polaron – hole polaron recombination within the triad as well as due to polaronic hole relaxation from the triad state to the free one again. Arrows in the figure denote photon emission relaxation transitions appearing after a Franck-Condon type excitation transition to the free electronic state.

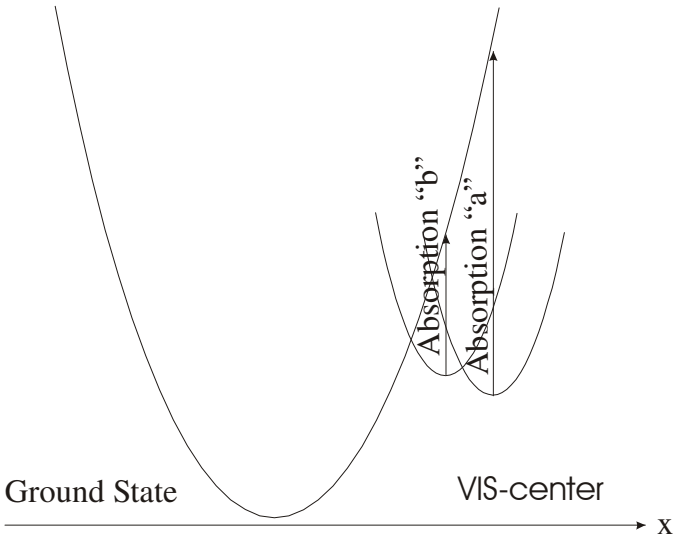

Fig.3.5.3. The main absorption transitions ("a" and "b") for resulting VIS-center

Thus both types of the VIS-centers are involved in the optical absorption. Let's note also that the existence of the two types of VIS-centers (Fig 3.5.1a, 3.5.1b) could explain the significant width of the resulting visible absorption band. Last not least, let us consider the typical mechanisms of the slow decay in the dark as well as light-induced decay for such a metastable state.

We have to deal with two typical mechanisms with respect to the slow decay in the dark of the VIS-center. *First*, this is a resonance up-conversion mechanism (Fig.3.5.2) related to the interaction between the two neighboring polaronic triads under discussion. While the first among these two triads is excited in the framework of the up-conversion with a following decay to conduction electron and hole bi-polaron states simultaneously (left-side triad on Fig. 3.5.2), the second triad involved in such an up-conversion is under a down relaxation transition (right-side triad on Fig. 3.5.2). The latter relaxation transition corresponds to a electronic polaron – hole polaron recombination which takes place simultaneously with the liberation of a polaronic hole within such a triad to a free polaronic hole. It is important to underline that this up-conversion decay for the two interacting polaronic triads has a conduction electron as decay product. Such a free electron will be under the following relaxation to *free electronic polaron* state. Free bi-polaronic holes as well as free polaronic holes both are also the triad decay products in this context. All these type polaronic excitations mentioned above with respect to the VIS-center decay could be detected by specific optical absorptions related to the light-induced charge transport phenomenon.

Note also, that another, *second* VIS center decay mechanism acting in the dark takes place here in a parallel way. This is the polaronic electron-polaronic hole recombination via tunneling as well as via thermally activated excited state tunneling or overbarrier processes (Fig.3.5.4). Only polaronic holes are remaining as a result of this decay mechanism taking place.

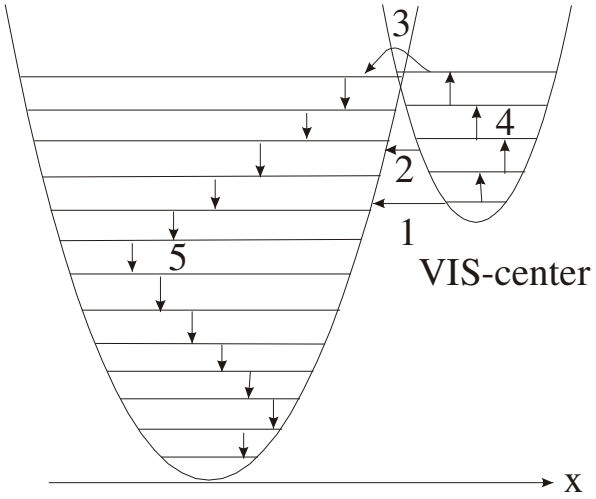

Fig.3.5.4. Three mechanisms of the VIS-center decay. “1” is the tunnel transition from VIS-center ground vibration state to exited vibration state related to the electronic ground state; “2” is tunnel transition between exited vibration states; “3” is thermally induced hopping between near barrier top quasidegenerate vibration states; “4,5” are phonon induced excitation and de-excitation processes within VIS-center state and ground state vibration wells, respectively.

It is important to underline that these decay mechanisms both could explain the VIS-center metastable behavior at low temperatures. This is due to the leading role of the transitions between vibronic states centered at rather different equilibrium positions for active ions. As a result, these vibronic states have exponentially small overlapping corresponding to exponentially small transition matrix elements and related transition probabilities for the VIS center decay.

It should be stressed that vibronic matrix elements and corresponding VIS center decay probabilities increase with temperature due to the occupation of excited vibration states with much more strong overlapping than for the ground vibration states. This general property for the mechanisms of the decay in the dark explains the shortening with temperature of the VIS-center life time in the dark, which has been detected experimentally for the SBN case at T > 140 K.

It should be also underlined that definite illumination could significantly accelerate the decay of the VIS-center. Moreover, electronic polarons could be the decay products in this situation. For instance, red light pumping could be used here. The model of the VIS-center in SBN proposed in the present work leads to the explanation for such an effect. Namely, a corresponding mechanism for the light-induced decay of the VIS center accompanied by electronic polaron liberation could be the direct light-induced excitation of the bonded, within the VIS –center, electronic polaron to a free electronic polaron state (channel 1 on Fig.3.5.5) or to the conduction band electronic state with the following transition to a free electronic polaron state (channel 2 on Fig.3.5.5). An initial optical excitation is possible in the framework of Franck-Condon transition (Fig.3.5.5) for both of these channels.

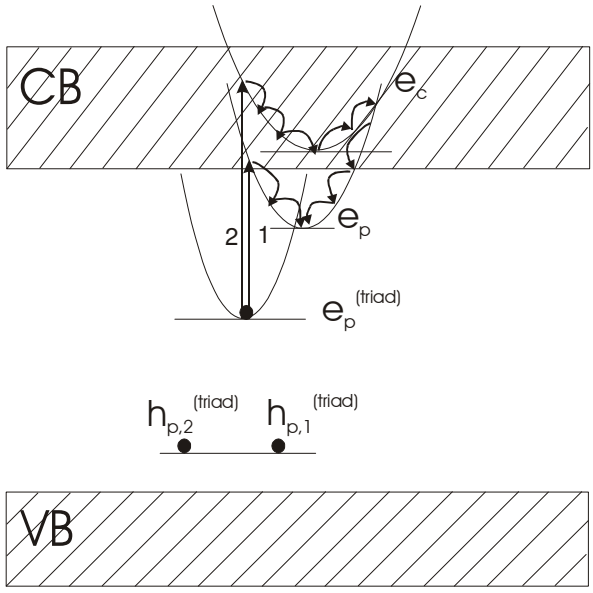

Fig.3.5.5 Light-induced decay of polaronic triad VIS-center to the electronic polaron state (channels “1”,”2”). Simultaneously, the denoted hole bi-polaron within the triad will be transformed to free hole bi-polaron with corresponding energy increase. Channel “1” is related to direct excitation of free electronic polaron state, while channel “2” is related to a two step transition from electronic polaron state within the triad to a conduction band electron state and then to the free electronic polaron state. The latter is realized via an overbarrier transition. Arrows in figure 3.5.5 are corresponding to successive relaxation processes with phonon emission or absorption.

4. Spectroscopic Study of KTO Crystals

4.1 Absorption and Light-Induced Absorption in KTO Crystals

The typical absorption spectrum of a pure KTO crystal is shown in Fig. 4.1.1. The UV absorption band edge of pure KTO crystals at room temperature lies at about 3.5 eV. In the visible range most of our samples show negligible absorption. After reduction or oxidation treatments the pure KTO crystals shows

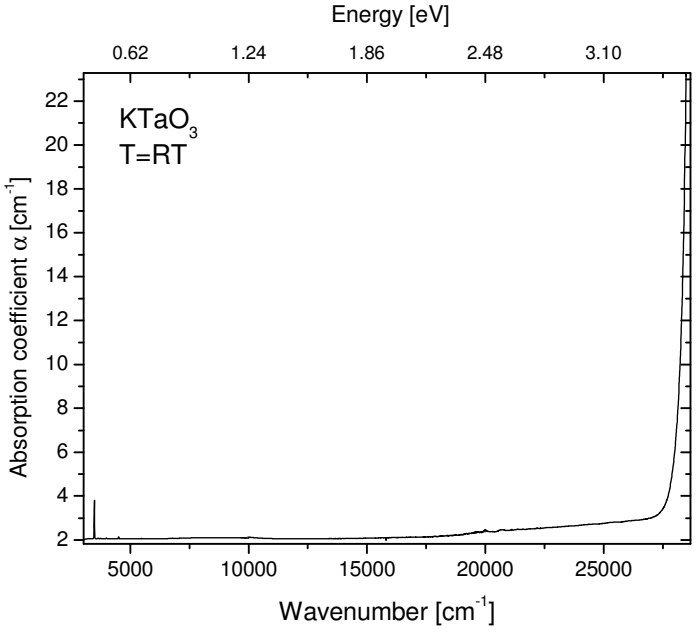

Fig. 4.1.1. Absorption spectra of KTO crystal (R108.2) at room temperature.

a broad absorption whose peaks are located at 12000 cm^{-1} and 18500 cm^{-1} (1.49 eV and 2.2 eV) at room temperature, Fig. 4.1.2. No other absorption bands due to reduction or oxidation treatments were observed. At low temperature these bands start to be more pronounced and one can distinguish three overlapping bands, Fig. 4.1.3, with maximum positions of absorption at 9925 cm^{-1} (1.23 eV), 12327 cm^{-1} (1.52 eV), and 18188 cm^{-1} (2.25 eV).

Also, in as grown and reduced KTO crystals a small amount of absorption at ~3500 cm^{-1} caused by OH centers incorporated at crystal growth or during reduction is present, Fig. 4.1.4.

At the same time, at low temperatures under illumination with an XBO lamp (λ=300-400 nm bandpass filter) a broad light-induced absorption from NIR to the VIS region appears in mostly all of the KTO crystals, Fig. 4.1.5.

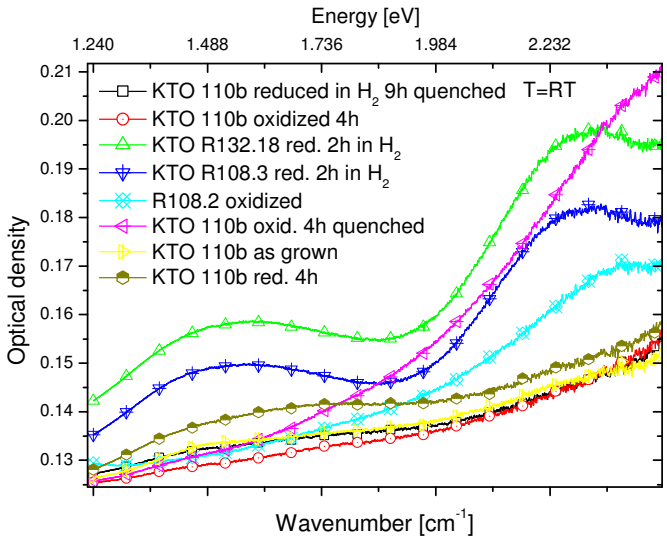

Fig. 4.1.2. Absorption spectra of reduced, oxidized and as grown KTO crystals at room temperature.

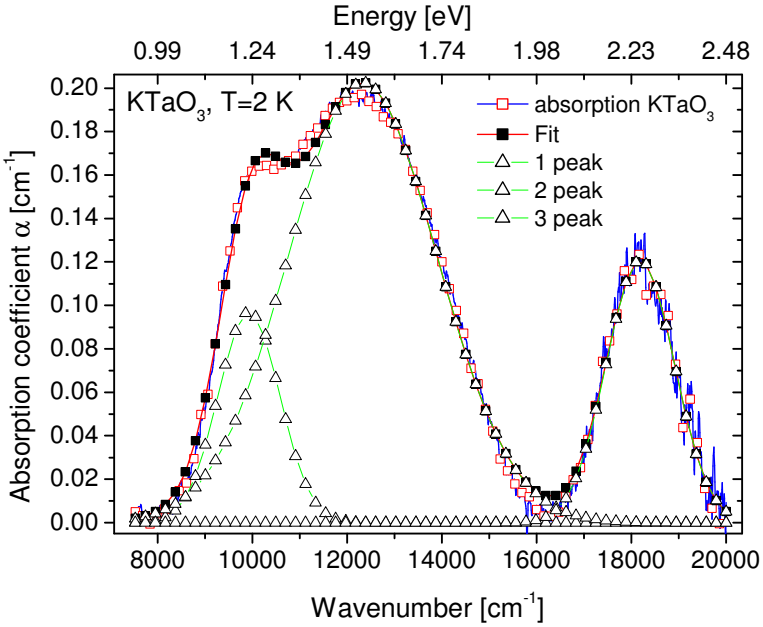

Fig. 4.1.3. Absorption of reduced KTO crystal (R132.18) at low temperature. Three overlapping bands could be resolved. Maximum positions of absorption from left to right: 9925 cm^{-1} (1.23 eV), 12327 cm^{-1} (1.52 eV), and 18188 cm^{-1} (2.25 eV).

The light-induced absorption is most pronounced in oxidized samples, whereas in reduced samples it is somewhat lower than in as grown crystals or even absent if the sample is treated in H_2 for more than two hours (depending on sample thickness). The width of the light-induced absorption is quite large giving evidence of the complex origin of the light-induced centers.

In most of the samples light-induced absorption looks quite similar, but in one of our samples, namely R101.2, it really differs (Fig. 4.1.5). The reason for such big difference is not clear at this moment. The temperature dependence of the light-induced absorption is shown in Fig.4.1.6.

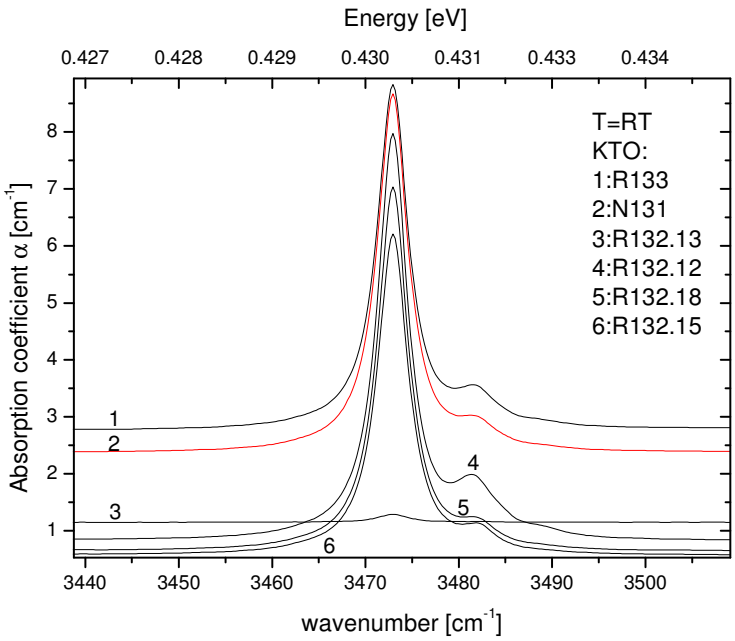

Fig. 4.1.4. OH absorption in different KTO crystals at room temperature. Reduction treatment is increasing OH absorption intensity. № 1-6 indicate different samples from three different boules (N131, R132, R133).

The absorption in reduced samples and the light-induced absorption in oxidized and as grown samples is quite similar, lying in the same spectral region and the band maxima have approximately the same energies. For example, fitting results of the light-induced absorption in oxidized KTO R108.2 sample with 3 Gaussian curves are shown in Fig. 4.1.7 (2 K) and Fig. 4.1.8 (52 K). The maximum positions of light-induced absorption are located at 9787 cm^{-1} (1.21 eV), 10900 cm^{-1} (1.35 eV), and 15660 cm^{-1} (1.94 eV) for T=2 K, and at 9191 cm^{-1} (1.14 eV), 11946 cm^{-1} (1.48 eV), and 17532 cm^{-1} (2.17 eV) for T=52 K.

We should also mention, that in the lowest temperature region, namely 1.3 - 30 K a strong change in the light-induced absorption shape exists. The reason for this change is not so clear up to now, but one of the explanations could be that a fourth band, which lays close to 9000 cm^{-1} is not present at temperatures higher than 20-30 K, see Fig.4.1.9.

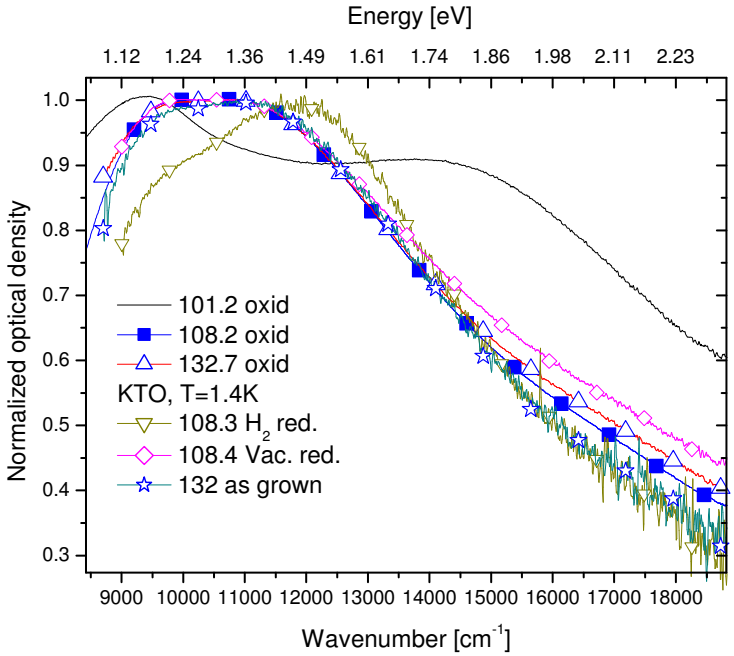

Fig. 4.1.5. Light-induced absorption in reduced, oxidized and as grown KTO crystals at 1.4 K under illumination with 300-400 nm light.

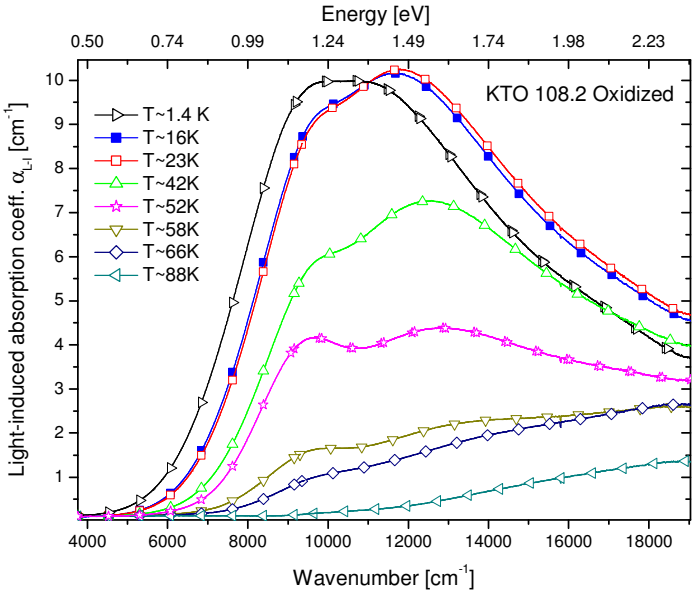

Fig. 4.1.6. The temperature dependence of the light-induced absorption in oxidized KTO R108.2 crystal under constant illumination with λ=300-400 nm.

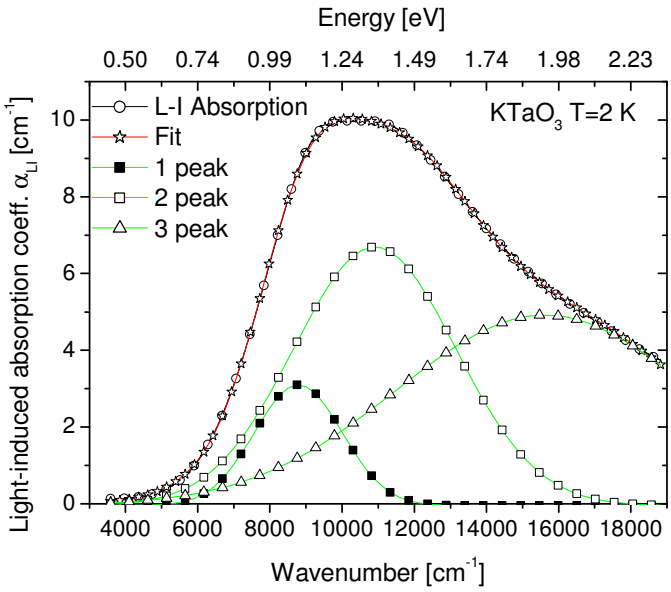

Fig. 4.1.7. Light-induced absorption under continuous illumination at 2 K in oxidized KTO. The fitting parameters are given in the text.

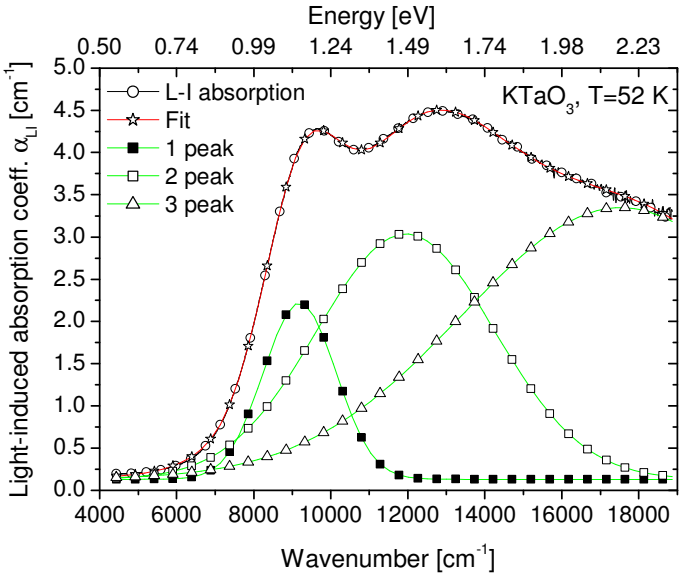

Fig. 4.1.8. Light-induced absorption under continuous illumination at 52 K in oxidized KTO. The fitting parameters are given in the text.

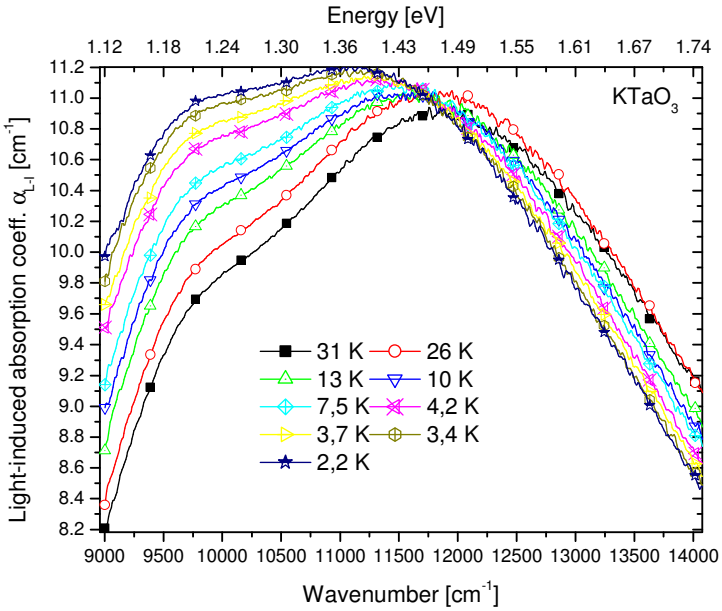

Fig.4.1.9. Variation of the light-induced absorption in the temperature range of 1.3-30 K under constant illumination with 300-400 nm light.

The fitting result of the light-induced absorption temperature dependence with 3 Gaussian curves is shown in Fig.4.1.10. From these results we could conclude that lower energy bands decay firstly with the temperature increase and the activation energies for these three bands about equal.

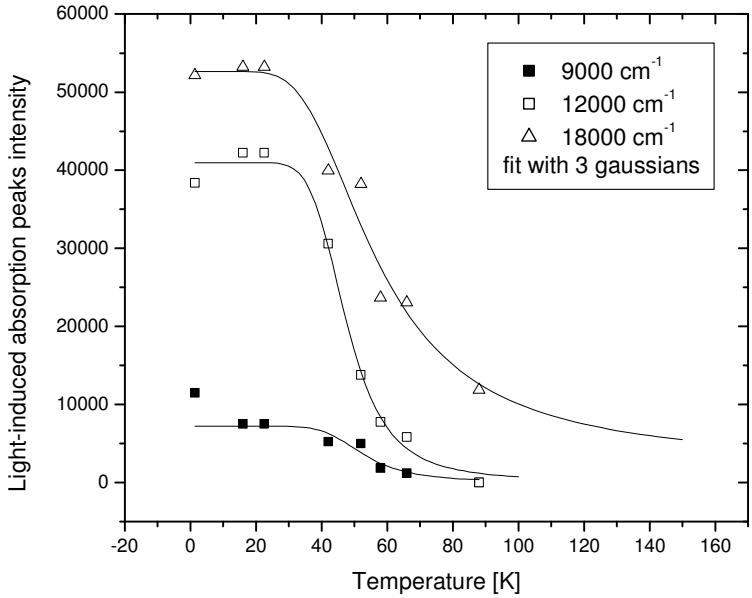

Fig. 4.1.10. Temperature dependence of the three subbands of the light-induced absorption in oxidized KTO crystal.

From the fitting of the temperature dependence we could get the values of the activation energies for this three bands: 9000 cm^{-1} ~0.033±0.015 eV, 12000 cm^{-1}~ 0.031±0.01 eV and for 18000 cm^{-1} 0.018±0.015 eV. The decay process of the light-induced absorption in oxidized KTO is shown on Fig. 4.1.11, and it is a rather complicated, not a single exponent decay.

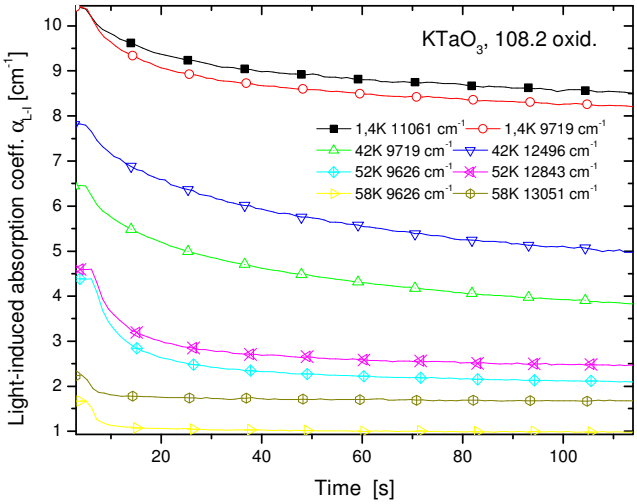

Fig.4.1.11. The light-induced decay process in oxidized KTO sample after switching off 300-400 nm light.

All of our samples show the same behaviour of the photo-EPR signals (measurements were performed at Kazan Sate University) as was found previously by Laguta at al. [40] and a possible explanation was given by O.F. Schirmer at al. in [41], Fig. 4.1.12, 4.1.13. After illumination with λ=300-400 nm light in the EPR spectra at 4.2 K three intensive lines with tetragonal symmetry appear with $g_{||}$=2.08, 2.09, 2.04 and $g_{\perp}$=1.17, 1.35 and 1.73, respectively.

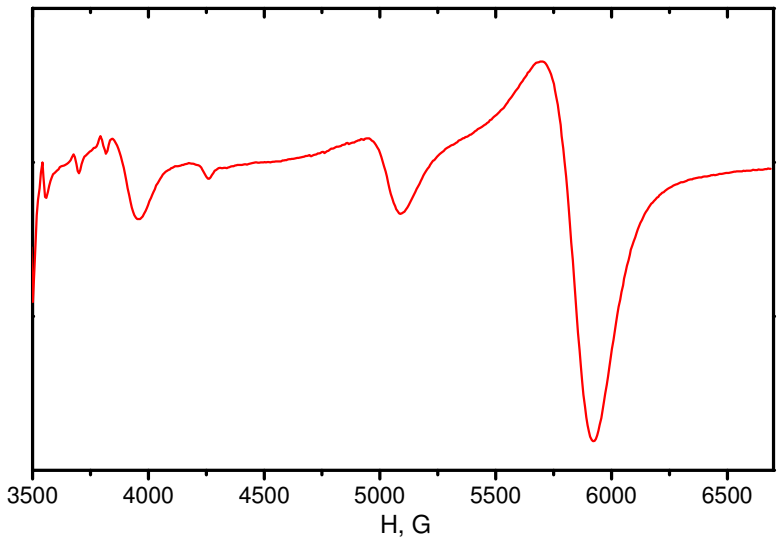

Fig. 4.1.12. Photo-EPR spectra for oxidized KTO at 4.2 K after illumination with light of λ=300-400 nm wavelength.

From the wavelength dependence of the photo-EPR spectra we can conclude that most of our centers appear under band-gap excitation, Fig. 4.1.14, as in the case of the usual light-induced absorption mentioned above.

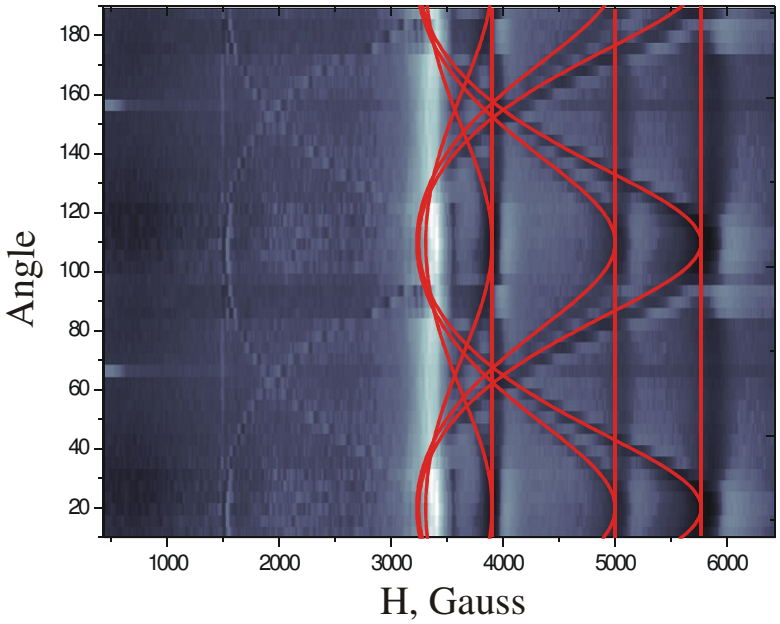

Fig. 4.1.13. The dependence of the photo-EPR signal on the direction of the magnetic field after illumination with λ=300-400 nm light at low temperatures (4.2 K).

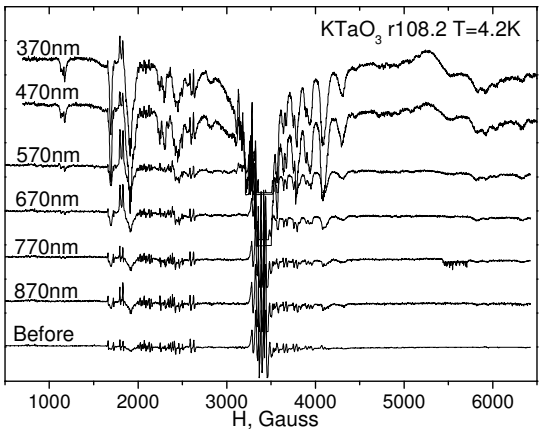

Fig. 4.1.14. Dependence of the light-induced EPR spectra on the pumping wavelength. (Results are vertically shifted for better viewing)

4.2 KTO. Discussion and Conclusions

The broadband green luminescence (GL) in $KTaO_3$ can be revealed best at low temperature under UV band edge illumination, as it was shown in [39]. The luminescence yield is increasing upon reduction and is diminishing upon oxidation, compared to the as grown crystal values. This result leads us to conclude that the crystal growth conditions yield the as-grown crystals in a slightly reduced state [113,114].

To check whether the reduction of the samples did affect only a surface layer or was homogeneous throughout the crystal, a reduced sample was polished thinner in successive steps. The luminescence was measured under identical conditions after each step, revealing constant luminescence intensity throughout the volume of the sample indicating a homogenous reduction. The green luminescence has been discussed successfully as the result of radiative recombination of polaronic type charge transfer vibronic excitons (CTVEs) in $KTaO_3$ [115,116,117].

The reduction treatment is seen to increase the number of charged defects, which stabilize the electron and hole polarons, with following increase of CTVEs concentration and increase of both the luminescence intensity and the amount of SHG in these samples. Here the excitation of the GL-luminescence, resulting mainly at the UV-band edge hints at the production of strongly correlated O^- and Ta^{4+} polarons in the form of CTVE's. The CTVE's with their inherent dipolar nature and clusters of CTVEs interacting with the Coulomb field of charged oxygen defects (like oxygen vacancies), are able to explain the present luminescence and SHG experiments in analogy to similar models employed to explain the light induced VIS-centers in SBN and BCT crystals [108].

The position in the NIR and the large half width of the light-induced and reduction-induced absorption bands also indicate the polaronic nature of the defects created. Hole polaron centers, like two different sorts of O^- centers, were revealed in recent EPR work [40,41]. Electron polarons Ta^{4+} in $KTaO_3$ [118] are not confirmed yet, but similar electron polarons (Ti^{3+} in $BaTiO_3$ and Nb^{4+} in $LiNbO_3$) have been determined experimentally [47,119].

The NIR/VIS light absorption of $KTaO_3$ reported, can be therefore explained as an effect of both, several kinds of O^- hole polarons (1-1.6 eV range) and in addition to the absorption of CTVE cluster – oxygen vacancies complexes (~2.2 eV VIS range) [39].

5 Spectroscopic Study of KTN Crystals

5.1 Absorption and Light-Induced Absorption in KTN Crystals

All our KTN samples at room temperature display aside of the fundamental absorption in the UV (> 3.25 eV for KTN) and in the FIR region (< 0.2 eV ≈ 6μ) only a

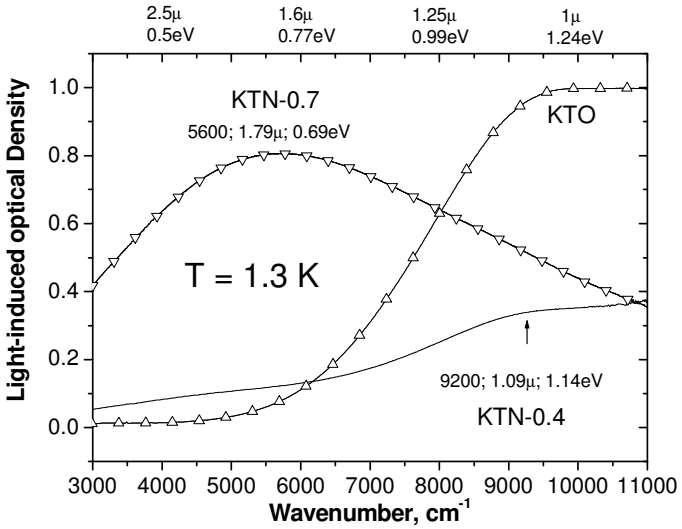

Fig.5.1.1. UV-light induced NIR absorption in KTO, KTN-0.4 and KTN-0.7

weak absorption at ~ 3500 cm^{-1} caused by the presence of the OH centers incorporated during crystal growth. No new absorption was found under UV-light excitation at RT.

At the same time, at low temperatures UV-illumination leads to a pronounced absorption emerging in the NIR region. Figure 5.1.1 presents this effect for quantum paraelectrics KTO, KTN-0.4 and KTN-0.7. The light-induced absorption spectra for KTN-0.4, and KTO appear to be very close to that which was reported recently for nominally pure KTO [39] and which was discussed in the previous chapter, displaying absorption bands at ~ 9200 cm^{-1} (1.14 eV) being attributed to O^- hole polarons, and a very faint band in the 5000 –6000 cm^{-1} region.

Small increasing of the Nb concentration in the quantum paraelectric KTN-0.7 (it is most close to the stability limit at the low temperatures among the compositions used here [91]) results in the emergence of a wide light-induced NIR absorption band at 5600 cm^{-1} (0.69 eV) with half-width ~ 0.5 eV at 1.3 K. This absorption increases and saturates approximately 100 s after UV light (XBO lamp, λ=300-400 nm) switching on (Fig.5.1.2, time depending on the pumping light and monitoring Fourier light intensities).

At low temperatures the NIR absorption is very stable and shows no decay in the dark (Fig. 5.1.3, experiment was done in the similar way as was described in chapter 3, page 37). The position of the absorption maximum agrees well with theoretical calculations ~ 0.78 eV for the Nb^{4+} electron polarons [120,100], experimental observations of electron polarons in related oxides TiO_2 (0.82 eV), BTO (~0.6 eV) [121,122], transient absorption bands at 0.8 eV reported recently in $KNbO_3$ under pulsed electronic beam excitation and tentatively associated with self-trapped electron polarons [120].

The large bandwidth of light-induced absorption can be explained by strong electron-lattice coupling as usual for polarons. This leads to the suggestion that this light-induced NIR absorption band is connected with

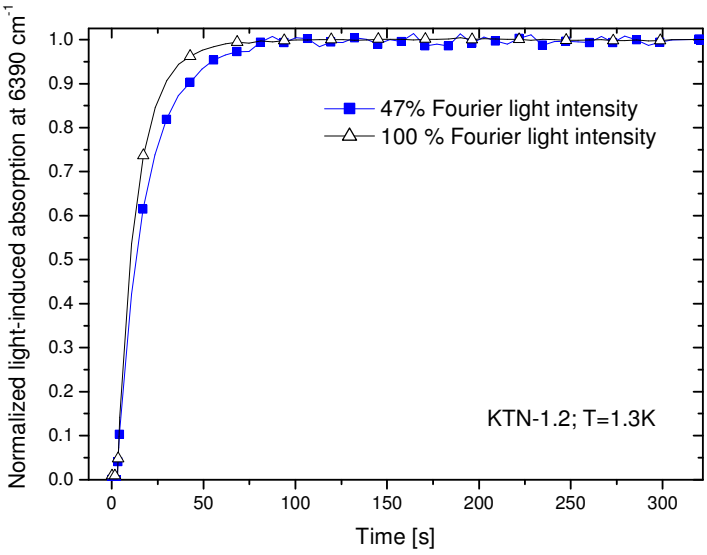

Fig. 5.1.2. Light-induced absorption in KTN-1.2 at the maximum position for NIR polaron absorption.

Nb^{4+} electron polarons. At further Nb concentration increasing a low-T ferroelectric phase transition emerges [91]. Figure 5.1.4 presents the UV light-induced absorption for low-T ferroelectric KTN-1.2 at different temperatures.

The light-induced absorption in the paraelectric cubic phase increases with temperature up to ~ 40 K and afterward decreases, practically vanishing at ~ 80 K (see Fig. 5.1.5).

Also from Fig. 5.1.2 and Fig. 5.1.6 one can conclude that the light-induced Nb^{4+} polaron absorption intensity and decay process strongly depend on the intensity of the Fourier spectrometer light (when other parameters like temperature and pumping light are kept constant).

The intensity dependence of the light-induced Nb^{4+} polaron absorption that was measured at 1.3 K and under XBO lamp illumination (λ=300-400 nm) is shown in Fig. 5.1.7. Even at small intensities there

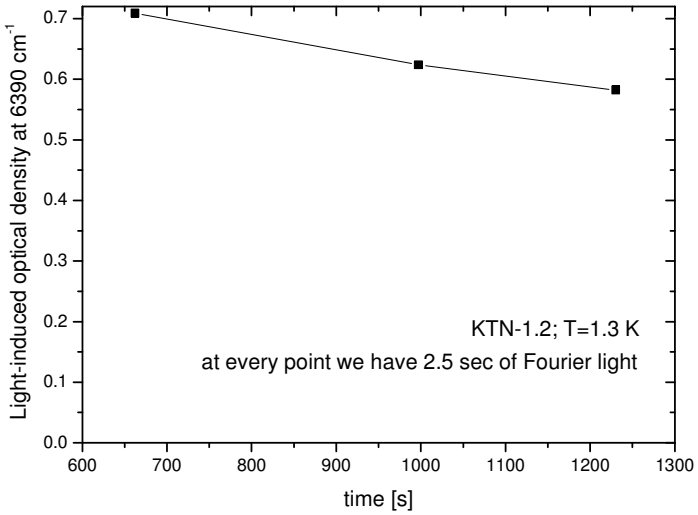

Fig. 5.1.3. The light-induced absorption decay (black squares) after illumination with λ=300-400 nm light (2kW/m^2) at 1.3 K. Solid line is guide for eyes.

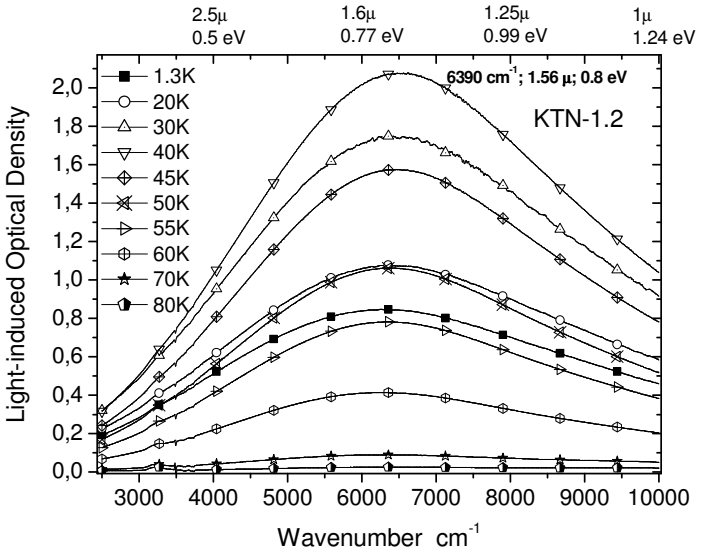

Fig.5.1.4. UV-light induced NIR absorption in KTN-1.2 as a function of temperature.

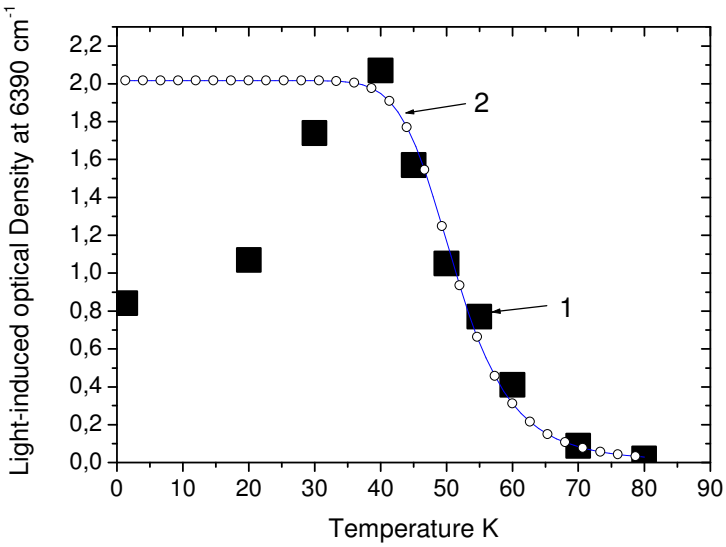

Fig.5.1.5. UV light-induced NIR absorption temperature dependence for KTN-1.2: 1- experimental data, size of the full squares indicates the error bars; 2- fit by a simplified charge transport model, page 49, with activation energy ~ 36 meV)

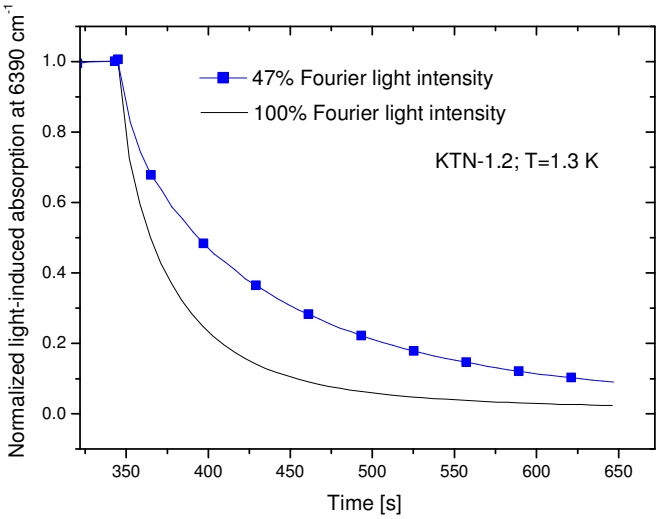

Fig.5.1.6. The light-induced absorption decay after illumination with λ=300-400 nm light (2kW/m2) at 1.3 K. Black curve is decay under 100% of the Fourier spectrometer light and blue is decay under 47 % of the Fourier spectrometer light.

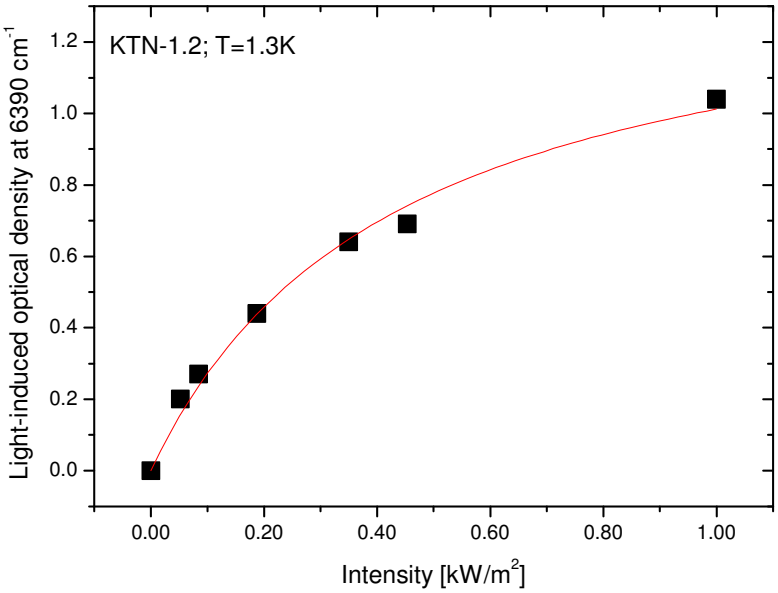

Fig. 5.1.7. Intensity dependence of the light-induced NIR absorption (black squares). Solid line is the fitting result with Eq. 3.4.2.3, page 49. Illumination with λ=300-400 nm light was used as pumping source.

exists a sizable light-induced effect and we can resolve it even better if we will reduce the Fourier spectrometer light intensity. The dependence of the light-induced absorption on the illumination intensity is obviously nonlinear. The decay process is found to be non-monoexponential and the temperature dependence is shown in Fig. 5.1.8 and the normalized light-induced absorption temperature dependence is presented in Fig. 5.1.9.

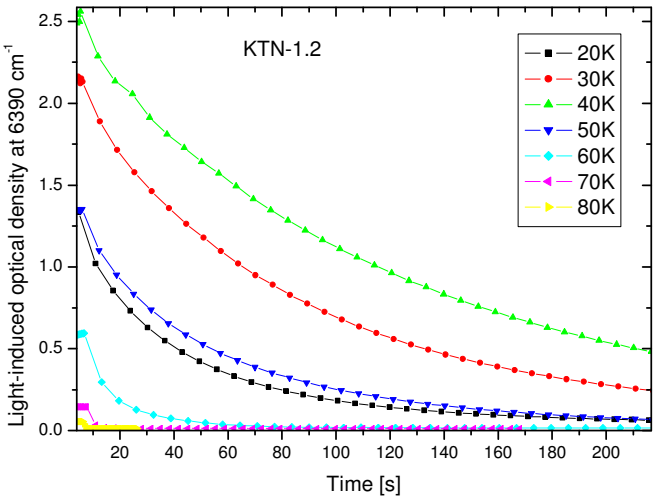

Fig. 5.1.8. The light-induced absorption decay at different temperatures after illumination with λ=300-400 nm light.

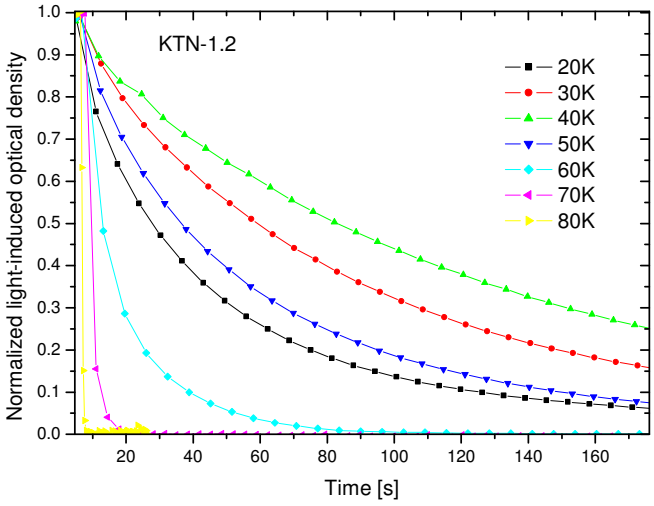

Fig. 5.1.9 The normalized light-induced NIR absorption decay after illumination with λ=300-400 nm light as a function of temperature.

We should take into account that from 20 K till 40 K the decay process is changing and is going to be longer with increasing temperature. The temperature dependence also indicates that the thermal activation of the light-induced Nb^{4+} polaron centers is playing a dominant role in the region 45-100 K. The decay at low temperatures is very small and present only due to the Fourier light.

The measurements show that the light-induced absorption increases with the Nb concentration and the absorption maximum shifts to higher energies closer to predictions and observations for $KNbO_3$ [123,120]. Due to the cubic-rhombohedral ferroelectric phase transition at ~ 16 K, some light scattering from ferroelectric domains increases somewhat the optical losses compared with those at 1.3 K. However, it does not change the main trend. In KTN-7 (which is ferroelectric rhombohedral below 65 K) the light-induced absorption band maximum locates at 6171 cm^{-1} (1.62μ, 0.76 eV) for 1.3 K (Fig. 5.1.10).

This small shift can be related with changes in the lattice constant due to the Nb doping. A similar character is observed in the temperature dependence of the UV-light induced polaron absorption, where the position of the absorption maximum and the thermal activation energy is shifting with the Nb concentration to higher values. For example, the light-induced polaron absorption temperature dependence is shown in Fig. 5.1.11 for KTN 30. In Fig.5.1.12 one could find the approximation of the light-induced absorption in KTN crystals under UV light illumination with four Gaussian peaks at 6308 cm^{-1}, 9241 cm^{-1}, 11022 cm^{-1}, and 16801 cm^{-1} respectively.

Three of them are very similar to the light-induced absorption peaks in pure KTO crystals (see chapter 4, page 62). The wavelength dependence of the light-induced absorption decay is presented in Fig. 5.1.13. The increasing decay time with higher energies can be related to the presence of the additional light-induced absorption bands (see Fig. 5.1.12), which usually appear under UV illumination in pure KTO (see chapter 4, page 62). As a result, at low

temperatures all the KTN crystals under study reveal a UV-light induced NIR absorption band with width and energy characteristic for Nb^{4+} electron polarons.

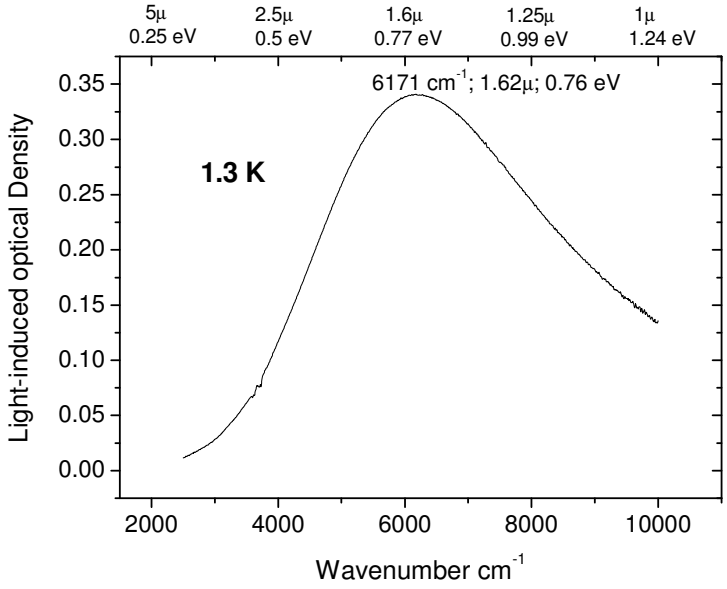

Fig.5.1.10. UV-light induced NIR absorption in KTN-7

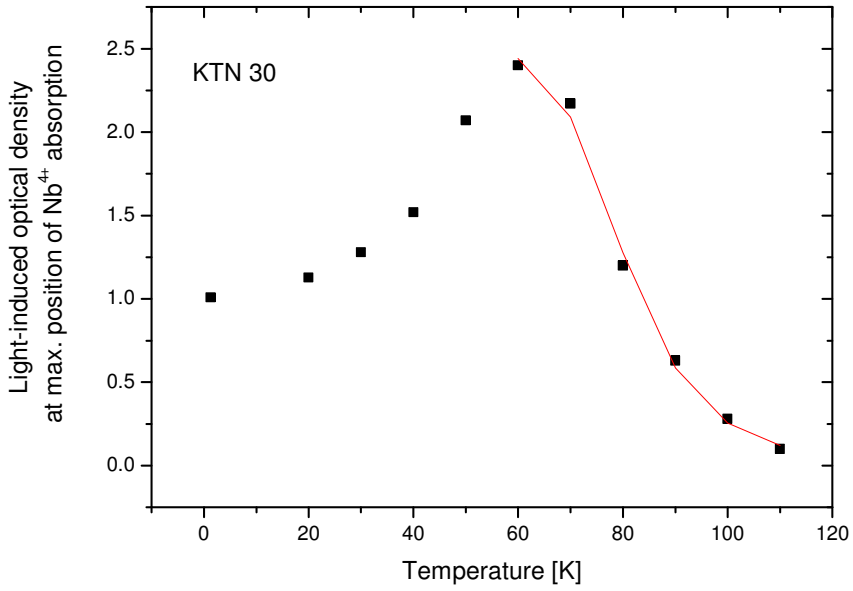

Fig. 5.1.11. UV light-induced NIR absorption temperature dependence for KTN-70/30: 1- experimental data, size of the full squares indicates the error bars; 2- fit by a simplified charge transport model, page 49, with activation energy ~ 76 meV)

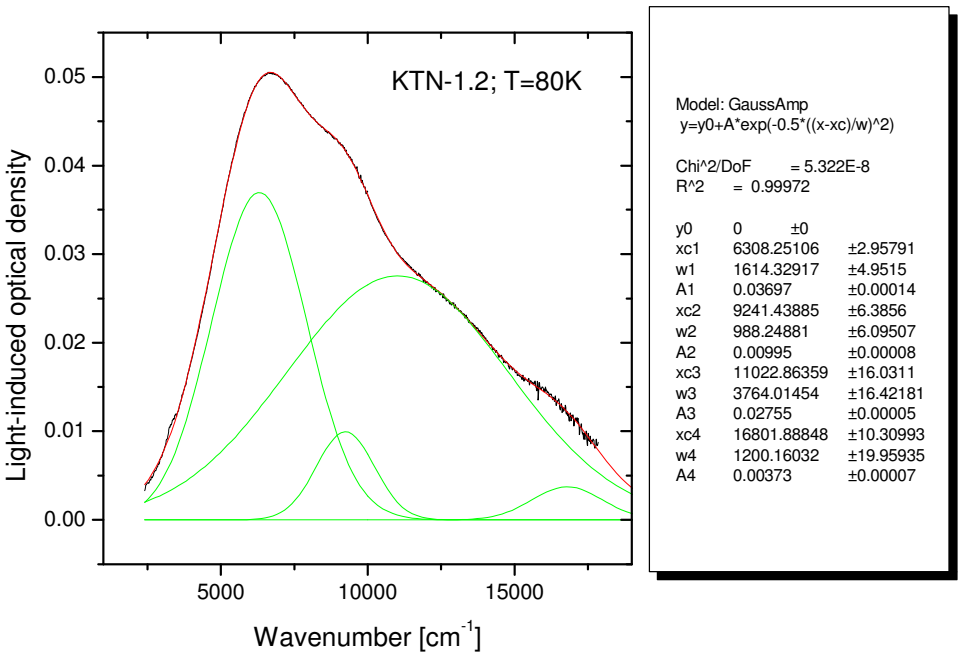

Fig.5.1.12. Light-induced absorption in KTN-1.2 at 80 K.
The peaks positions are from left to right :
6308 cm^{-1} (0.78 eV), 9241 cm^{-1} (1.14 eV), 11022 cm^{-1} (1.36 eV), and 16801 cm^{-1} (2.08 eV).

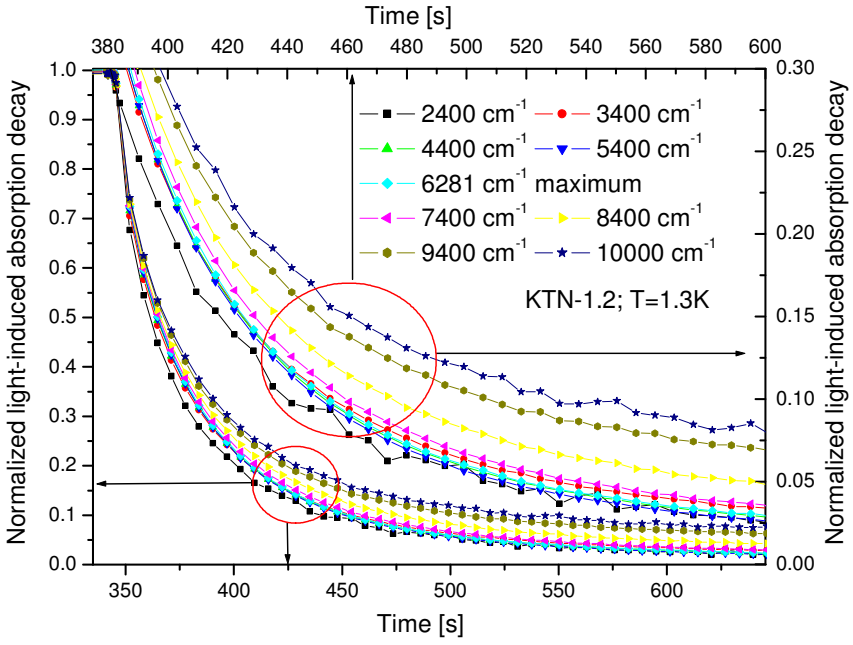

Fig.5.1.13. The light-induced absorption decay for different spectral positions.

5.2 Green Luminescence in KTN Crystals

Surprising results are revealed in the luminescence experiments. Under UV light excitation the KTN specimens under study reveal wideband visible green emission, which is conventional and characteristic for ABO_3 perovskites (Fig. 5.2.1 presents emission and excitation spectra for KTN-1.2). The emission intensity smoothly decays with temperature increasing and practically vanishes at ~100 K, see Fig. 5.2.2.

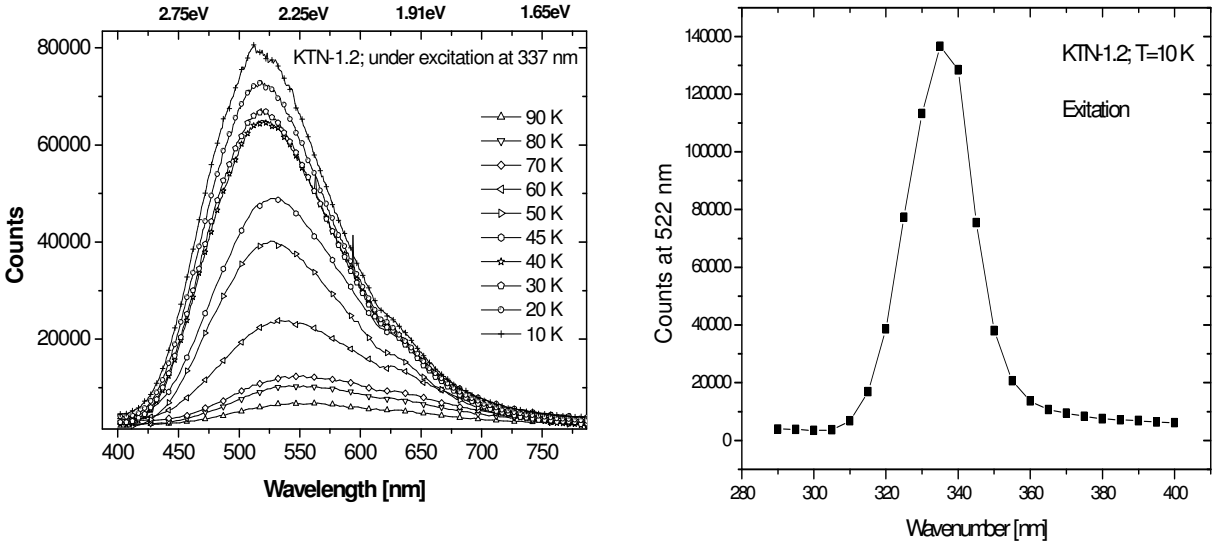

Fig.5.2.1. Excitation and emission luminescence spectra for KTN-1.2.

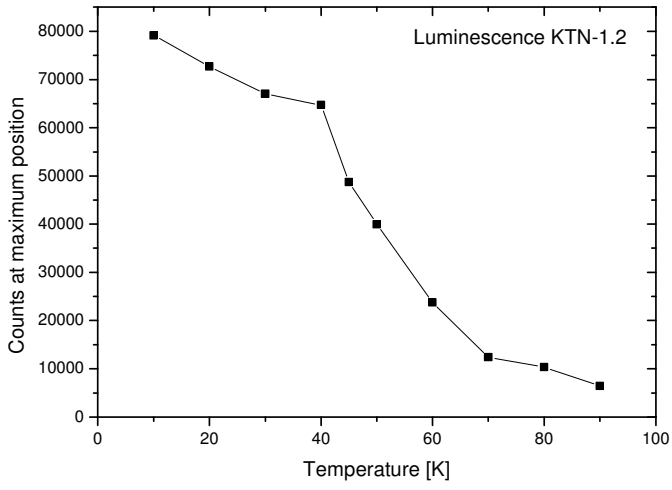

Fig. 5.2.2. Temperature dependence of the luminescence intensity in KTN. Solid line is a guide for eye.

The position of the maximum shifts from 511nm (2.43 eV) at 10 K, till 548 nm (2.25 eV) at 90 K. The nature of this emission in ABO_3 oxides is still a subject under discussion. Various mechanisms, from donor- acceptor recombination, till a charge transfer vibronic exciton recombination, have been proposed (for a list of references see in Ref. [120]). The decay process of the luminescence in KTN –1.2 is shown in Fig. 5.2.3. We found that whereas in all ABO_3

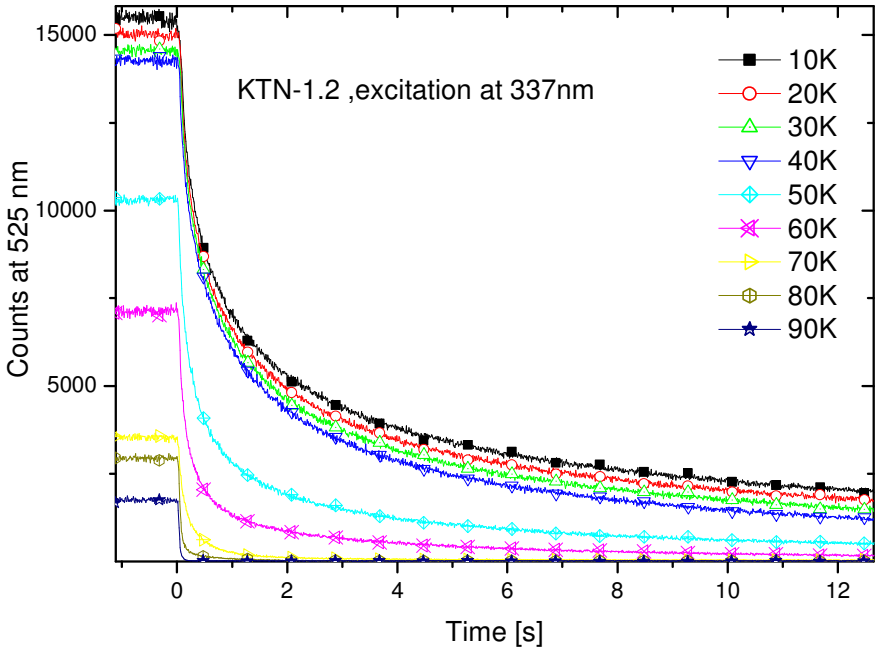

Fig. 5.2.3. Decay process of the luminescence at different temperatures. KTN-1.2.

perovskites this emission has a millisecond order of decay time, in KTN-1.2 it strongly increases below 40 K up to about 10 seconds at 10 K, i.e. namely in the temperature region of the dominant quantum fluctuations. In the same temperature region namely above 40 K the UV light-induced NIR absorption begins to decrease with temperature. This coincidence supports the suggestion that the localization and following release of the photo-induced charge carriers occurring by Nb is constituting the main cause of this phenomenon.

5.3 Theoretical Model for Nb^{4+} Polaron in KTN Crystals

We can discuss the actual light-induced absorption spectra on the basis of a conventional two-site model for optical small polarons hopping between random close pairs of Nb ions [121] (Fig. 5.3.1). In this model the absorption maximum corresponds to the optical Franck-Condon $O \to O'$ transition from the ground state of the Nb^{4+} polaron to the branch of the neighbor $Nb^{4+/5+}$ ion potential with the energy $\hbar\omega = 4E_a$ [121], which gives ~ 0.7 eV for optical transition energy and polaronic activation energy E_a ~ 175 meV (~ 2000 K) for our case. In the low temperature region ($T << \hbar\omega_0$), the

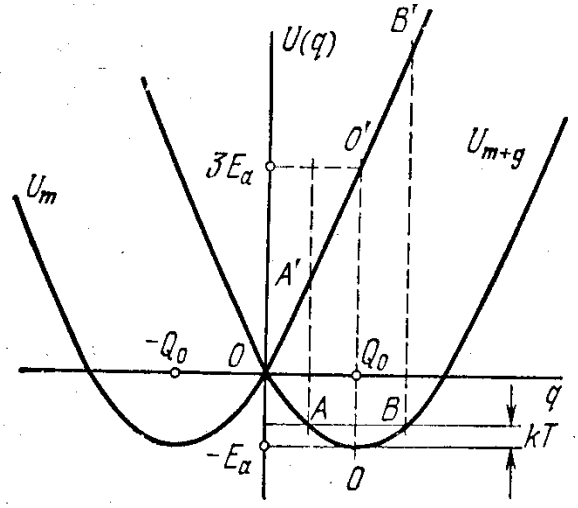

Fig.5.3.1. Configuration curves for the two-site model.

energy of the zero-point vibrations can be estimated as $\frac{\hbar\omega_0}{2}$, which is ~ 55 meV (~ 640 K) for KTO [124]. The width of the polaronic absorption band can be expressed as ~ $8\sqrt{\frac{E_a\hbar\omega_0}{2}}$ [121]. This gives ~ 0.5 – 0.7 eV for the width of the polaron absorption band, which is in good agreement with our experimental results for KTN.

The presence of Nb pairs is not a strong assumption. The possibility of Nb clustering in KTN has been considered, e.g., in Ref. [125]. In very weakly concentrated KTN, like KTN-0.4, the number of Nb pairs is small. Therefore in this case the UV light-induced absorption band is only faintly pronounced in KTN-0.4 as a weak shoulder in the 5000 – 6000 cm^{-1} region (Fig.5.1.1, page 67). In KTN-0.7 the concentration of Nb pairs increases as does the respective electron polaron absorption. The light-induced absorption increases appreciably in KTN-1.2, but further on, for KTN-7 this increasing appears to be not so strong any more. This fact can be understood if in the polaron optical absorption only pairs of neighboring Nb ions play the main role and it is not necessary to form infinite clusters of the nearest neighbor Nb ions.

We believe that even in weakly concentrated KTN there are enough nearest-neighbor-Nb-pairs to account for the observed absorption. This logic, and the absence of the infinite Nb

clusters on the other hand, lead to the important sequence, that the Nb^{4+} optical polaron formation should strongly decrease the d.c. conductance and photoconductivity at low temperatures. And this sequence was confirmed recently in low-temperature photoconductivity measurements of KTN-0.4, KTN-0.7 and KTN-1.2 specimens used in this work, providing strong arguments for the assumption of strong charge localization at low temperatures (Fig. 5.3.2), published by us in [126].

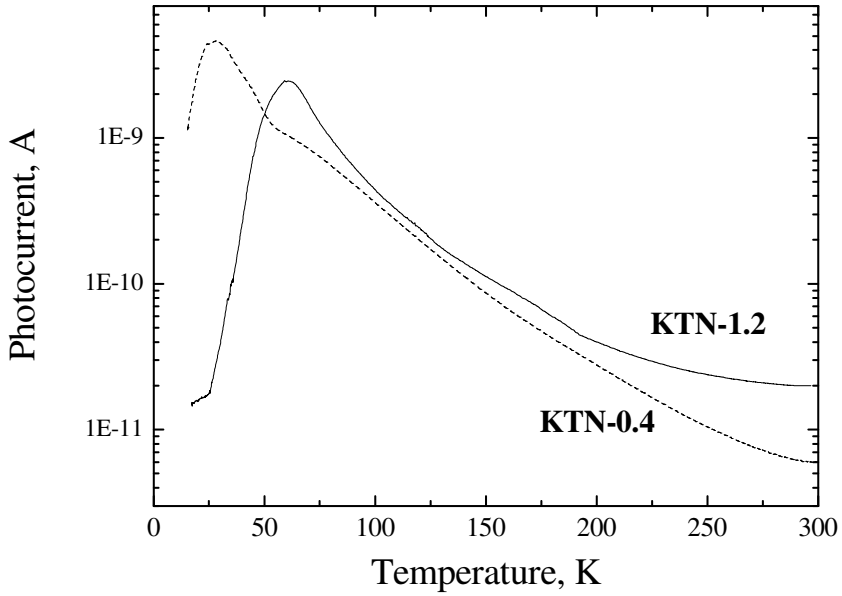

Fig.5.3.2. Temperature dependence of the photocurrent under UV-band-gap excitation.

Now, let us consider the rather strange temperature behavior of the UV light-induced absorption. As it is seen in Fig. 5.1.4, page 69, at the lowest temperatures the light-induced absorption increases somewhat with temperature and then decreases. The nature of the low temperature behavior is not clear at the moment and needs further studies. It only can be assumed that photo-carriers generation, transport, trap transformation processes and changing in oscillator strength can play here a decisive role.

The absorption decay at about 40 K can be associated with the presence of a "thermal quenching level" or thermally activated electron release from polaronic states into the conduction band. From a simplified charge transport model which is described in chapter 3, page 50 (we just replace $Ce^{3+/4+}$ centers with the hole centers in the valence band) estimation gives the value for the Nb^{4+} polaron thermal activation energy as ~ 36 meV for KTN-1.2 and ~76 meV for KTN-30.

Before conclusion two important remarks, regarding NIR absorption band interpretation and photoconductivity features have to be made. Quite long ago, a broad NIR absorption peaking near 0.6 eV has been reported for BTO and KTN-35 [127] and was attributed to deep donor (probably, oxygen vacancy) photoionization into a broad conduction band. However this absorption has been found in strongly reduced specimens only and had another shape. Besides, conventional optical absorption in our KTN specimens, being measured without

additional UV-excitation, did not reveal any absorption in the NIR region. So, we conclude that as it was proven later for Ti^{3+} in BTO [122], too, the UV light induced NIR absorption in KTN is connected with Nb^{4+} polaron optical transitions.

Regarding the photoconductivity, it is very interesting to note, that the low temperature localization of hole or electronic polarons lead to opposite effects in the photoconductivity. Indeed, as it was seen, UV excitation of KTO and STO is accompanied by NIR absorption attributed to localized hole O^- polarons and the photoconductivity of STO [128] and KTO [40] increases at low temperatures too. This effect very strongly reminds the results of Ca and Li doping results of STO [129] and KTO [130,131] respectively, when the low temperature freezing of <100> Li and Ca off center ions leads to O ions displacements, and the appearance of shallow hole traps. These traps withdraw photoholes from recombination with conduction bands photoelectrons and the photoconductivity being controlled by electrons increases. As a result, PhI generation and localization of O^- photoholes (which is accompanied by the appearance of the O^- hole polaron absorption, mentioned above) increases the photoconductivity in STO, KTO and KTO:Li at low temperatures. In contrast, in KTN, the localization of the electronic photopolarons prevails, which decreases the concentration of conductive electrons in the conduction band, decreasing photoconductivity at low temperatures.

5.4 KTN. Discussion and Conclusions

Experimental observations of the UV-light induced NIR absorption supplemented by photoconductivity studies in the temperature region 1.3–300 K have been reported for $KTa_{1-x}Nb_xO_3$ single crystals (x=0, 0.004, 0.007, 0.012, 0.07, 0.3). The results are considered as an evidence for the formation of the small electronic Nb^{4+} polarons at low temperatures.

No photochromic effect was found at RT in all Nb containing species as well as in nominally pure $KTaO_3$. The emergence of the UV-light induced wide absorption bands in the NIR region with maxima at 0.69–0.8 eV at low temperatures is treated as a manifestation of the localization of photo-induced electrons and the formation of Nb^{4+} small electron polarons in close-neighbor Nb-Nb pair centers.

Position and width of the light-induced NIR absorption bands is in good agreement with theoretical estimations for small electronic polarons. It was predicted that Nb doping has to suppress the photoconductivity in KTN at low temperatures, which has been confirmed experimentally in further studies [126]. This agrees with the suggested close-neighbors Nb^{4+}-Nb^{5+} pair centers model, considering Nb^{5+} ions as effective traps for photo-excited electrons at low temperatures.

The effective trapping of charge carriers is supported also by the, characteristic for ABO_3 oxides, “green” photoluminescence, in which the strong increasing of the luminescence decay time from millisecond up to about 10 seconds was found in KTN. In the intermediate temperature region the UV-light induced NIR absorption begins to decrease and then vanishes (~ at 40 K and 80 K respectively for KTN with x=0.012), due to the presence of a quenching level or thermal activation of the electron from the Nb^{4+} polaron into the CB.

The results obtained show clear evidence of the localization of UV excited charge carriers as electronic polarons (Nb^{4+}) at low temperatures for the case of diluted KTN. Also we should mention here that just recently we found light-induced absorption in STO crystals, and it shows similar to KTO crystals light-induced absorption and this fact supports our conclusions too.

6.1 Conclusions

The aim of the current work was to investigate light-induced properties of SBN:Ce, KTO and KTN materials like origin of trapping centers which are involved in the charge transport process, characterization of trapping centers, like temperature dependence, illumination intensity dependence, evolution with time, spectral response, activation energies, the basic properties of the electronic excitations and photo-carriers localization based on results of absorption, light-induced absorption, photoluminescence, and photocurrent. The main contributions of this dissertation are summarized as follows:

- The accompanying decrease of T_c with dopant concentration indicates a suppression of long range ordering by impurity related random fields due to charge mismatch brought by the Cr and Ce doping. The increased width of the $\varepsilon'(T)$ maximum can be regarded as consequence of nonuniform distribution of the doping ions. Ce and Cr doping have a depressing effect on T_c and no self compensation of Ce and Cr ions was found in the experiments, which can be understood on the basis of a local charge compensation in the oxygen sublattice around each defect.

- The doping with small Li-ions was expected to enhance T_c in SBN, due to a dipolar off-center nature of the small Li-ions (like in KTL), but this did not seem to take place in the Chromium co-doped crystals.

- The spin-orbital and crystal field splitting of $4f^1$ level of Ce^{3+} ions is not resolved in the visible range, but this splitting exists and is shown in characteristic absorption bands in the FIR region (around 2000 cm^{-1}).

- Under illumination with Ar^+ laser light or with XBO lamp (380-480 nm) at low temperature SBN:Ce crystals show a broad NIR polaron absorption band around 0.84 eV (6900 cm^{-1}) and a broad VIS-center absorption band near 2.03 eV (16500 cm^{-1})

- At low temperatures (T = 1.3 K) the NIR-polaron centers and the VIS centers in SBN:Ce crystals are very stable and do not decay in the dark. The decay observed of the NIR polaron and the VIS centers is present due to the Fourier spectrometer light. The temperature dependence of the light-induced absorption yields the values of the potential barriers (for the NIR-polaron- 0.08±0.02 eV, for the VIS centers-0.23±0.04 eV)

- The experimental intensity dependence, temperature dependence, and decay process of the light-induced polaron and VIS center absorption can be fitted with the help of the simplified charge transfer model.

- The fit with the help of the simplified charge transfer model to the experimental data at different temperatures of the light-induced Nb^{4+} polaron absorption shows that the parameters of the model are changing. From the model by itself the light-induced polaron absorption should not change in the low temperature region (T<60 K). Perhaps

this slight increasing in the light-induced polaron absorption can be explained taking into account Smakula's formula. There, the oscillator strength is also temperature dependent. If we will take a look to the absorption of the polarons in reduced SBN crystals we will find that in this case also a slight increasing in the polaron absorption as a function of temperature exist. In other words, we can assume that for light-induced Nb^{4+} polarons in the SBN:Ce case the oscillator strength is changing with the temperature.

- Dissociation of the VIS centers under illumination with red Kr^+ laser light or with red laser diode light lead us to conclude that at least one part of the process are NIR-polaron centers. These features give new insight into the dynamic nature of these VIS-centers, which are currently being discussed as either bipolarons (in analogy to such centers in $LiNbO_3$) or polarons trapped at charged centers, or charge transfer vibronic excitons (CTVEs) being trapped at charged centers

- A theoretical model to describe the possible nature of the VIS centers is proposed. The main idea of the VIS-center model in SBN is a triad structure related to the simultaneous bonding of two hole polarons and one electronic polaron. The metastable behavior could be reached here by vibronic effects on the one hand, and by taking part of electronic polarons in the strong local field of two polaronic holes on the other.

- Near infrared absorptions in the KTO crystals due to reduction or due to light-induced intrinsic defects at low temperature is reported here for the first time. The nature of these defects is still under discussion, with correlated self-trapped electron and hole polarons being the most probable candidates yielding good agreement between theoretical calculations and experimental observations.

- Experimental observations of UV-light induced NIR absorption supplemented by photoconductivity studies in the temperature region 1.3–300 K have been reported for $KTa_{1-x}Nb_xO_3$ single crystals (x=0, 0.004, 0.007, 0.012, 0.07, 0.3). Results are considered as evidence for the formation of the small electronic Nb^{4+} polarons at low temperatures.

- The emergence of the UV-light induced wide absorption bands in the NIR region with maxima at 0.69–0.8 eV at low temperatures is treated as a manifestation of the localization of photo-induced electrons and the formation of Nb^{4+} small electron polarons in close-neighbor Nb-Nb pair centers. Position and width of the light-induced NIR absorption bands is in good agreement with theoretical estimations for small electronic polarons. It was predicted that Nb doping has to suppress photoconductivity in KTN at low temperatures, which has been confirmed experimentally in further studies of the photoconductivity.

- The effective trapping of charge carriers is supported also by the, characteristic for ABO_3 oxides, "green" photoluminescence, in which the strong increasing of the luminescence decay time from millisecond up to about 10 seconds was found in KTN at low temperatures.

- In the intermediate temperature region the UV-light induced NIR absorption begins to decrease and then vanishes (~ at 40 K and 80 K respectively for KTN with x=0.012), due to the presence of a quenching level or thermal activation of the electron from the Nb^{4+} polaron into the CB.

- The experimental intensity dependence, temperature dependence, and decay process of the light-induced Nb^{4+} polaron absorption in KTN can be fitted with the help of the simplified charge transfer model, yielding an activation energy of about 36 meV for KTN-1.2 and 76 meV for KTN-30.

6.2 Suggestions for Further Work

Further experimental techniques are necessary to clarify the details of the nature of the VIS centers in SBN. For this purpose we initiated photoconductivity and photo-Hall effect measurements under Kr^{+}-laser or red laser diode illumination, to get new information about the charge carriers created. These investigations are currently under way. Also the lattice site occupancy of dopants, their properties, charge compensation and the distribution of dopant charge states are really interesting field for further investigations and could be done by optical absorption, luminescence and ESR measurements. Another direction in studies of these materials could be investigations in suitable double doping properties, which are important for holographic storage.

From a practical point of view KTN is a well-known advanced material for a number of nonlinear optics applications, holographic gratings, channel switchers e.t.c. As well as quantum paraelectric STO and KTO, diluted KTN is a promising material for operating at cryogenic temperatures, in outer space, and now, for novel optical controlled dielectric devices. Under bandgap illumination a giant photo-induced dielectricity appears in KTO and STO crystals. Further experiments to elucidate the nature of the UV light induced effects and possible photo-induced phase transitions at low temperatures in KTO and KTN crystals are also should be performed. As example, one could do SHG and dielectric susceptibility measurements at low temperatures under or after UV bandgap illumination to clarify how the UV excitation and formation of the light-induced centers is playing a role in possible photo-induced phase transitions.

7 References

1. A. A. Ballman and H. Brown. *The growth and properties of strontium barium metaniobate, $Sr_{1-x}Ba_xNb_2O_6$, a tungsten bronze ferroelectric*. Journal of Crystal Growth **1**, 311-314 (1967)

2. J. B. Thaxter. *Electric control of holographic storage in strontium-barium-niobate.* Applied Physics Letters **15**, 210-212 (1969)

3. J. B. Thaxter and M. Kestigian. *Unique properties of SBN and their use in a layered optical memory*. Applied Optics **13**, 913-924 (1974)

4. F. Micheron, C. Mayeux, and J. C. Trotier. *Electrical control in photoferroelectric materials for optical storage.* Applied Optics **13**, 784-787 (1974)

5. S. Redfield and L. Hesselink. *Enhanced nondestructive holographic readout in strontium barium niobate.* Optics Letters **13**, 880-882 (1988)

6. M. R. Kruer, L. Esterowitz, F. J. Bartoli, and R. E. Allen. *Optical radiation damage of SBN materials and pyroelectric detectors at 10.6 μm.* Journal of Applied Physics **46**, 1072-1079 (1975)

7. A. M. Glass. *Investigation of the electrical properties of $Sr_{1-x}Ba_xNb_2O_6$ with special reference to pyroelectric detection.* Journal of Applied Physics **40**, 4699-4713 (1969)

8. R.R. Neurgaonkar and W.K. Cory. *Progress in Photorefractive Tungsten Bronze Crystals*. J. Opt. Soc. Am. B **3**, 274-282 (1986)

9. R.R. Neurgaonkar, W.K. Cory, J.R. Oliver, M.D. Ewbank, and W.F. Hall. *Development and Modification of Photorefractive Properties in the Tungsten Bronze Family Crystals.* Optical Engineering **26**, 392-405 (1987)

10. R.R. Neurgaonkar, W.F. Hall, J.R. Oliver, W.W. Ho, and W.K. Cory. *Tungsten Bronze $Sr_xBa_{1-x}Nb_2O_6$: a Case History of Versatility*. Ferroelectrics **87**, 167-179 (1988)

11. M. Horowitz, A. Bekker, and B. Fischer. *Image and Hologram Fixing Method with $Sr_xBa_{1-x}Nb_2O_6$ Crystals.* Opt. Lett. **18**, 1864-1966 (1993)

12. A. Krumins, A. Anspoks, S. G. Odulov, J. Seglins, and P. Vaivods. *Thermal Holograms in Doped Ferroelectric SBN Crystals.* Ferroelectrics **80**, 277-280 (1988)

13. J. E. Ford, J. Ma, Y. Fainman, S.H. Lee, Y. Taketomi, D. Bize, and R.R. Neurgaonkar. *Multiplex Holography in Strontium Barium Niobate with Applied Field*. J. Opt. Soc. Am A **9**,1183-1192 (1992)

14. R. De Vre, M. Jeganathan, J. P. Wilde, and L. Hesselink. *Effect of Applied Electric Fields on the Writing and the Readout of Photorefractive Gratings.* J. Opt. Soc. Am. B **12**, 600-614 (1995)

15. H. Y. Zhang, X. H. He, Y. H. Shih, and L. Yan. *Picosecond phase conjugation and two-wave coupling in strontium barium niobate.* Journal of Modern Optics **41**, 669-674 (1994)

16. G. Salamo, M.J. Miller, W.W. Clark III, G.L. Wood, and E.J. Sharp. *Strontium Barium Niobate as a Self-pumped Phase Conjugator.* Opt. Commun. **59**, 417-422 (1986)

17. G.L. Wood, W.W. Clark III, M.J. Miller, E.J. Sharp, G.J. Salamo, and R.R. Neurgaonkar. *Broadband Photorefractive Properties and Self-pumped Phase Conjugation in Ce-SBN :60.* IEEE J. Quant. Elect. QE-**23**, 2126-2135 (1987)

18. K. Megumi, H. Kozuka, M. Kobayashi, and Y. Furuhata. *High-sensitive Holografic Storage in Ce-doped SBN*. Appl. Phys Lett. **30**, 631-633 (1977)

19. K. Sayano, A. Yariv, and R. Neurgaonkar. *Enhanced Photorefractive Gain in Cr-doped Strontium Barium Niobate with an External dc Electric Field*. J. Appl. Phys. **67**, 1594-1596 (1990)

20. Y. Tomita and A. Suzuki. *Photorefractive Properties of Cr-doped Strontium-Barium Niobate at 514.5nm and 632.8 nm: A Comparative Study*. Appl. Phys. **A59**, 579-582 (1994)

21. R.A. Vazquez, M.D. Ewbank, and R.R. Neurgaonkar. *Photorefractive Properties of Doped Strontium-Barium Niobate*. Opt. Commun. **80**, 253-258 (1991)

22. R.A. Vazquez, R.R. Neurgaonkar, and M.D. Ewbank. *Photorefractive Properties of SBN:60 Systematically Doped with Rhodium*. J. Opt. Soc. Am. B **9**, 1416-1427 (1992)

23. M.D. Ewbank, R.A. Vazquez, R.R. Neurgaonkar, and F. Vachss. *Contradirectional Two-beam Coupling in Absorptive Photorefractive Materials: Application to Rh-doped Strontium Barium Niobate (SBN:60)*. J. Opt. Soc. Am. B **12**, 87-99 (1995)

24. T.L. Hall, R. Jaura, L.M. Connors, and P.D. Foote. *The Photorefractive Effect-A review.* Prog. Quant. Electr. **10**, 77-146 (1985)

25. P. Günter and J.P. Huignard. *Photorefractive Effects and Materials, in Photorefractive Materials and Their Applications I: Fundamental Phenomena* Edited by P. Günter and J. P. Huignard. Springer-Verlag, Berlin, 1988

26. H. Kurz and E. Krätzig. *Photorefractive centers in $LiNbO_3$, Studied by Optical-, Mössbauer- and EPR-Methods*. Appl. Phys. **12**, 355-368 (1977)

27. E. Krätzig and O.F. Schirmer. *Photorefractive Centers in Electro-optic Crystals, in Photorefractive Materials and Their Applications I: Fundamental Phenomena*. Edited by P. Günter and J. P. Huignard. Springer-Verlag, Berlin, 1988

28. K. Nasu. *Relaxation of Excited States and Photo-Induced Structural Phase Transitions*. ed. K Nasu (Berlin: Springer, 1997) p.6.

29. K. Nasu, H. Ping, H. Mizouchi. *Photoinduced structural phase transitions and their dynamics*. J. Phys.: Condens. Matter **13**, R693-R721 (2001)

30. T. Hasegawa, K. Tanaka. *Photo-induced anomalous Debye-type relaxation in strontium-titanate*. Abstracts of ICL'02, Budapest, Hungary, 24-29 August 2002

31. T. Hasegawa, S. Mouri, Y. Yamada, K. Tanaka. *Giant photo-induced dielectricity in $SrTiO_3$*. J. Phys. Soc. Jpn. **72**, 42-44 (2003)

32. M. Takesada, T. Yagi, M. Itoh, S. Koshihara. *A gigantic photoinduced dielectric constant of quantum paraelectric perovskite oxides observed under a weak dc electric field.* J. Phys. Soc. Jpn. **72**, 37-40 (2003)

33. M. Tekesada, T. Yagi, M. Itoh, T. Ishikawa, S. Koshihara. *Photoinduced phenomena in quantum paraelectric oxides by ultraviolet laser irradiation*. Ferroelectrics **298,** 317-323 (2004)

34. I. Katayama, Y. Ishikawa, K. Tanaka. *Critical behaviors of photoinduced giant permittivity in potassium tantalate.* Phys. Rev. B **67**, 100102-1−100102-4 (2003)

35. T. Hasegawa, M. Shiraii, K. Tanaka. *Localizing nature of photo-excited states in $SrTiO_3$.* J. Lumin. **87-89**, 1217-1219 (2000)

36. T. Hasegawa, K. Tanaka. *Photo-induced polaron states in strontium titanate*. J. Lumin. **94-95**, 15-18 (2001)

37. S. A. Prosandeev, V. Trepakov, M. Savinov, S. Kapphan. *Characteristics and the nature of the low-frequency dielectric response in moderately concentrated $KTaO_3$: Li.* J. Phys.: Condens. Matter **13**, 9749-9760 (2001)

38. K. Uchida, S. Tseuneyuki, T. Schimizu. *First-principles calculations of carrier-doping effects in $SrTiO_3$.* Phys. Rev. B **68**, 174107-1− 174107-6 (2003)

39. S.E. Kapphan, A.I. Gubaev, V.S. Vikhnin. *UV light-induced absorption in pure $KTaO_3$ at low temperature*. Phys. Stat. Sol. (c) **2**, 128-131 (2005)

40. V. Laguta, M. Glinchuk, I. Bykov, A. Cremoma, P. Galinetto, E. Giulotto, L. Jastrabik, J. Rosa. *Light-induced defects in $KTaO_3$.* J. Appl. Phys. **93**, 6956-6054 (2003)

41. M. Maiwald, O.F. Schirmer. *O^- dynamic Jahn-Teller polarons in $KTaO_3$.* Europhys. Lett. **64**, 776-782 (2003)

42. V.A. Trepakov, S.A. Prosandeev, M.E. Savinov, P. Galinetto, G. Samoggia, S. E. Kapphan, L. Jastrabik, L.A. Boatner. *Low-temperature phase transformations in*

weakly doped quantum paraelectric: novel features and quantum reentrant dipolar glass state in $KTa_{0.982}Nb_{0.0018}O_3$. J. Phys. Chem. Sol. **65**, 1317-1327 (2004)

43. M. Maglione. *Interaction between conductivity and dielectric relaxation in perovskites*. Ferroelectrics **176**, 1 (1996)

44. V. V. Lemanov, E. P. Smirnova, A. V. Sotnikov, M. Weinacht. *Dielectric relaxation in SrTiO3 : Mn.* Phys. Sol. State **46**, 1442-1448 (2004)

45. O.F. Schirmer, Th. W. Kool, , S. Lenjer, M. Maiwald. *EPR of Jahn-Teller polarons in oxide perovskites.* Phys. Stat. Sol. **2**, 124-127 (2005)

46. O. Schirmer, D. von der Linde. *Two-photon and X-ray induced Nb^{4+} and O^- small polarons in $LiNbO_3$*. Appl. Phys. Lett. **33**, 35-38 (1978)

47. S. Lenjer, O.F. Schirmer, H. Hesse, Th.W. Kool. *Conduction states in oxide perovskites: Three manifestations of Ti^{3+} Jahn-Teller polarons in barium titanate*. Phys. Rev. B **66**, 165106-1–165106-12 (2002)

48. H. Liu, R.C. Powell, L.A. Boatner. *Effect of niobium doping on the properties of picosecond laser-induced transient gratings in $KaTa_{1-x}Nb_xO_3$*. Phys. Rev. B **44**, 2461-2469 (1991)

49. NTT Technical Review, R&D Information **1**, 56 (2003)

50. P. Pesach, G. Bartal, E. Refaeli, A. J. Agranat. *Free-space optical cross-connect switch by use of electroholography.* Appl. Opt. **39**, 746-758 (2000)

51. V.N. Bogomolov, E.K. Kudinov, and Yu. A. Firsov. *Polaron Nature of the Current Carriers in Rutile TiO_2*. Soviet Physics-Solid state **9**, 2502-2513 (1968)

52. V.N. Bogomolov and D.N. Mirlin. *Optical Absorption by Polarons in Rutile (TiO_2) Single Crystals.* Phys stat. Sol. **27**, 443-453 (1968)

53. J.T. Devreese. *Polarons and Bipolarons in Oxides*. Z. Phys. B. **104**, 601-604 (1997)

54. I.G. Austin and N.F. Mott. *Polarons in Crystalline and Non-crystalline Materials.* Adv. Phys. **18**,41-101 (1969)

55. D. Emin. *The Formation and Motion of Small Polarons, in Linear and Nonlinear Electron Transport in Solids,* Edited by J.T. Devreese and V.E. van Doren. Plenum Publishing Corporation, New York, 1976

56. D. Emin. *Small Polarons*. Phys. Today, 34-40 June 1982

57. H.G. Reik and D. Heese. *Frequency Dependence of the Electrical Conductivity of Small Polarons for High and Low Temperatures*. J. Phys. Chem. Solids **28**, 581-596 (1967)

58. H.G. Reik. *Optical Effects of Small Polarons at High Frequencies with an Application to Reduced Strontiumtitanate*. Zeitschrift für Physik **203**, 346-361 (1967)

59. P.B. Jamieson, S.C. Abrahams, and J.L. Bernstein. *Ferroelectric Tungsten Bronze-Type Crystal Structure. I. Barium Strontium Niobate* $Ba_{0.27}Sr_{0.75}Nb_2O_{5.78}$. J Chem. Phys. **48**, 5048-5057 (1968)

60. T. S. Chernaya, B. A. Maksimov, I. V. Verin, L. I. Ivleva, and V. I. Simonov. *Crystal structure of* $Ba_{0:39}Sr_{0:61}Nb_2O_6$ *single crystals.* Crystallography Reports **42,**375-380 (1997)

61. K. Megumi, N. Nagatsuma, Y. Kashiwade, and Y. Furuhata. *The Congruent Melting Composition of Strontium Barium Niobate.* J. Mater. Sci. **11**,1583-1592 (1976)

62. A.A. Ballman and H. Brown. *The Growth and Properties of Strontium Barium Metaniobate,* $Sr_{1-x}Ba_xNb_2O_6$*, A Tungsten Bronze Ferroelectric*. J. Cryst. Growth **1**, 311-314 (1967)

63. N. Wittler, G. Greten, S. Kapphan, R. Pankrath, and J. Seglins. *Dielectric Measurements on SBN:Ce.* Phys. Stat. Sol. (b) **189**, K37-K40 (1995)

64. Yu-Huan Xu, Zhonggrong Li, Wu Li, and Hong Wang. *Phase Transition of Some Ferroelectric Niobate Crystals with Tungsten-bronze Structure at Low Temperatures.* Phys. Rev. B **40**, 11902-11908 (1989)

65. R.R. Neurgaonkar, W.K. Cory, J.R. Oliver, W.W. Clark III, G.L. Wood, M.J. Miller, and E.J. Sharp. *Growth and Ferroelectric Properties of Tungsten Bronze* $Ba_{2-x}Sr_xK_{1-y}Na_yNb_5O_{15}$ *(BSKNN) single Crystals*. J. Cryst. Growth **84**, 629-637 (1987)

66. T. Volk, Th. Whoike, U. Doerfler, R. Pankrath, L. Ivleva, and M. Woehlecke. *Ferroelectric Phenomena in Holographic Properties of Strontium –Barium Niobate Crystals Doped with Rare-earth Elements.* Ferroelectrics **203**, 457-470 (1997)

67. A. Gubaev, R. Demirbilek, R. Pankrath, S. Kapphan, I. Kislova, B. Pedko, V. Trepakov. *Doping-Dependent Properties in Photorefractive Congruent* $Sr_xBa_{1-x}Nb_2O_6$*: Ce, Cr Crystals*. Ferroelectrics **303**, 185-188 (2004)

68. R. Niemann, K. Buse, R. Pankrath, M. Neuman, *XPS study of Photorefractive* $Sr_{0.6}Ba_{0.4}Nb_2O_6$*:Ce crystals*. Sol. St. Commun. **98**, 209-213 (1996)

69. T. Woike, G. Weckwerth, H. Palme, R. Pankrath. *Instrumental Neutron Activation and Absorption Spectroscopy of Photorefractive Strontium-Barium-Noibate Single Crystals Doped with Cerium.* Sol. St. Commun. **102**, 743-747 (1997)

70. V. M. Goldschmidt. *Über Atomabstände in Metallen*. Z. Phys. Chem. **133**, 397-419 (1928)

71. J. Bohm, W. Kleber, H.J. Bautsch und I. Kleber. *Einführung in die Kristallographie*. Verlag Technik GmBH Berlin, 12. Auflage, 1990

72. A. Reisman, F. Holtzberg, M. Berkenblit und M. Berry. *Reactions of the Group VB Pentoxides with Alkali Oxides and Carbonates. III. Thermal and X-Ray Phase Diagrams of the System K_2O or K_2CO_3 with Ta_2O_5*. J. Am. Chem. Soc. **78**, 4514-4520 (1956)

73. G.A. Samara and B. Morosin. *Anharmonic Effects in $KTaO_3$: Ferroelectric Mode, Thermal Expansion, and Compressibility*. Phys. Rev. **B8**, 1256-1264 (1973)

74. S.H. Wemple. *Some Transport Properties of Oxigen-Deficient Single-Crystal Potassium Tantalate ($KTaO_3$).* Phys. Rev. **137**, A1575-A1572 (1965)

75. P.A. Fleury and J.M. Worlock. *Electric-field-induced Raman scattering in $SrTiO_3$ and $KTaO_3$*. Phys. Rev. **174**, 613-623 (1968)

76. H. Vogt and H. Uwe. *Hyper-Raman scattering from the incipient ferroelectric $KTaO_3$.* Phys Rev. B **29**, 1030-1034 (1984)

77. C.H. Perry and T.F. McNelly. *Ferroelectric "Soft" Mode in $KTaO_3$.* Phys. Rev. **154**, 456-458 (1967)

78. E. Courtens. Ferroelectrics **183**, 25 (1996)

79. W. R. Abel. *Effect of Pressure on the Static Dielectric Constant of $KTaO_3$*. Phys. Rev. **B4**, 2696-2701 (1971)

80. H. Uwe, H. Unoki, Y. Fujii and T. Sakudo. *Stress Induced Ferroelectricity in $KTaO_3$.* Solid State Comm. **13**, 737-739 (1973)

81. Y. Fujii and T. Sakudo. *Electric-field-induced Optical Second-harmonic Generation in $KTaO_3$ and $SrTiO_3$.* Phys. Rev. **B13**, 1161-1167 (1976)

82. Y. Fujii and T.Sakudo. *Dielectric and Optuical Properties of $KTaO_3$*. J. Phys. Soc. Japan **41**, 888-893 (1976)

83. R.L. Prater, L.L. Chase and L.A. Boatner. *Raman Scattering Studies of the Impurity-Induced Ferroelectric Phase Transition in $KTaO_3$:Li*. Phys. Rev. **B23**, 5904-5915 (1981)

84. R.L. Prater, L.L. Chase and L.A. Boatner. *Raman Scattering Studies of the Efects of a Symmetry-Breaking Impurity on the Ferroelectric Phase Transition in $K_{1-x}Li_xTa_{1-y}Nb_yO_3$*. Solid state Comm. **40**, 697-701 (1981)

85. Y. Yacoby and S. Just. *Differential Raman Scattering from Impurity Soft Modes in Mixed Crystals of $K_{1-x}Na_xTaO_3$ and $K_{1-x}Li_xTaO_3$.* Solid State Comm. **15**,715-718 (1974)

86. B. Hellermann, F. Baller, R. Blachnik, B. Gather, H. Hesse and J. Schnitter. *Crystal growth and characterization of $K(Ta_{1-x}Nb_x)O_3$-solid solutions.* Thermochimica acta **160**, 71 (1990)

87. A. Reisman, S. Triebwasser and F. Holtzberg. *Phase Diagram of the System $KNbO_3$-$KTaO_3$ by the Methods of Differential Thermal and Resistance Analysis*. J. Am. Chem. Soc. **77**, 4228 (1955)

88. S. Triebwasser. *Study of Ferroelectric Transitions of Solid-Solution Single Crystals of $KNbO_3$-$KTaO_3$*. Phys. Rev. **114**, 63-70 (1959)

89. F. Baller, B. Gather, H. Hesse and E. Krätzig. *The Influence of Stress on the dielectric Properties of KTN Crystals*. Phys. Stat. Sol. (a) **116**, K195 (1989)

90. D.M. Hannon. *Electron paramagnetic resonance of Fe^{3+} and Ni^{3+} in $KaTaO_3$.* Phys. Rev. **164**, 366-371 (1967)

91. L.A. Boatner , U.T. Höchli and H. Weibel. *Phase diagram of ferroelectric potassium niobate ($KTa_{1-x}Nb_xO_3$).* Helf. Phys. Acta **50,** 620-622 (1977)

92. G.Greten, S. Hunsche, U. Knüpffer, R. Pankrath, U. Siefker, N. Wittler, and S. Kapphan. *Defect and Light-Induced Absorption, Luminescence and Dielectric Properties in SBN:Cerium*. Ferroelectrics **185**, 289-292 (1996)

93. R. Demirbilek, A.B. Kutsenko, R. Pankrath, S.E. Kapphan. *Investigation of far infrared transitions of Ce^{3+} in congruent SBN crystals*. Ferroelectrics **303**, 775-778 (2004)

94. G. Greten. *Defekt- und Lightinduzierte Absorption, Lumineszenz und Dielektrische Untersuchungen an Strontium-Barium-Niobat:Cer*. Ph.D. Dissertation, University of Osnabrueck (1996)

95. G. Blasse, W.Schipper, and J.J. Hamelink. *On the Quenching of the Luminescence of the Trivalent Cerium Ion.* Inorganica Chimica Acta **189**,77-80 (1991)

96. Ming Gao. *Optical Investigation of Light-induced Charge Transport in SBN Crystals*. Ph.D. thesis (1998)

97. B. Faust, H. Müller, and O.F. Schirmer. *Free Small Polarons in $LiNbO_3$*. Ferroelectrics **153**, 297-302 (1994)

98. O.F. Schirmer, O. Thiemann, and M. Wöhlecke. *Defects in $LiNbO_3$-I. Experimental Aspects*. J. Phys. Chem. Solids **52**, 185-100 (1991)

99. K. Buse, U. van Stevendaal, R. Pankrath, and E. Krätzig. *Light-Induced Charge Transport Properties of $Sr_{0.61}Ba_{0.39}Nb_2O_6$:Ce Crystals.* J. Opt. Soc. Am. B **13**,1461-1467 (1996)

100. R.C. Baetzold. *Calculations of Defect Properties Important in Photorefractive $Sr_{0.6}Ba_{0.4}Nb_2O_6$.* Phys Rev B **48**, 5789-5796 (1993)

101. M. Gao, R. Pankrath, S. Kapphan, and V. Vikhnin. Appl. Phys B **68**, 849-858 (1999)

102. B. Faust, H. Müller, and O.F.Schirmer. *Free Small Polarons in $LiNbO_3$.* Ferroelecttrics **153**, 297-302 (1994)

103. M.G. Clark, F.J. DiSalvo, A.M. Glass, and G.E. Peterson. *Electronic Structure and Optical Index Damage of Iron-doped Lithium Niobate.* J. Chem. Phys. **59**, 6209-6219 (1973)

104. M.D. Ewbank, R.R. Neurgaonkar, W.K. Cory, and J. Feinberg. *Photorefractive Properties of Strontium-Barium Niobate.* J. Appl. Phys. **62**, 374-380 (1987)

105. K. Buse. *Light-Induced Charge Transport Process in Photorefractive Crystals I: Models and Experimental Methods*. Appl. Phys. B **64**, 273-291 (1997)

106. Ming Gao, S. Porcher, R. Pankrath, and S. Kapphan. *Light-induced VIS and NIR absorption in SBN : Ce and SBN : Cr crystals*. J. Korean Phys. Soc. **32**, S542-S544 (1998)

107. Ming Gao, S. Kapphan, R. Pankrath, Xiqi Feng, Yuanfen Tang, and V.S. Vikhnin. *Light-induced VIS-absorption and light-induced charge transfer in pure and doped SBN crystals.* J Phys. Chem. Sol. **61**, 1775-1787 (2000)

108. V. Vikhnin, S. Avanesyan, H. Liu, S. Kapphan. *An origin of light induced centers in the visible range in ferroelectric oxides: possible role of the states of charge transfer vibronic excitons*. J. Phys. Chem. Solids **63**, 1677-1683 (2002)

109. V.S. Vikhnin, A.I. Gubaev, and S.E. Kapphan. *A model of the polaronic origin of the VIS-centers in ferroelectric oxides : SBN-case.* To be published.

110. V.S. Vikhnin, R.I. Eglitis, S.E. Kapphan, E.A. Kotomin, and G. Borstel. *A new phase in ferroelectric oxides: The phase of charge transfer vibronic excitons.* Europhysics Letters **56** (5), 702-708 (2001)

111. V.S.Vikhnin, R.I. Eglitis, S.E. Kapphan, G. Borstel, and E.A. Kotomin. *Polaronic-type excitons in ferroelectric oxides: Microscopic calculations and experimental manifestation.* Phys. Rev. **B 65**, 104304-104304-11 (2002)

112. V.S. Vikhnin. *New polaronic excitons in ferroelectric oxides: phenomenological theory.* Solid State Communications **127,** 283-288 (2003)

113. C. Fischer, C. a. d. Horst, P. Voigt, S. Kapphan, J. Zhao. *Luminicence and optical second harmonic generation by dipolar microregions in $KTaO_3$*. Rad. Eff. and Def. in Solids **136**, 995-999 (1995)

114. C. a. d. Horst, S. Magnien, S. Kapphan. *Variation of Luminescence and Second Harmonic Generation of Defect Polarization Clusters Induced by Reduction in Pure $KTaO_3$ and $KTaO_3$:Fe.* Ferroelectrics **185**, 265 (1996)

115. V. S. Vikhnin, S. E. Kapphan. *Vibronic charge-transfer excitons: possible nature of the unusual properties of virtual perovskitelike ferroelectrics.* Phys. Solid State **40**, 834-836 (1998)

116. V.S. Vikhnin, R.I. Eglitis, E.A. Kotomin, S.E. Kapphan, and G. Borstel. *Fundamental physics of ferroelectrics*, edited by H. Krakauer, AIP Conf. Proc. Ser., Vol. **582,** 228-238 (AIP, Melville, New York, 2001)

117. R.I. Eglitis, E.A. Kotomin, G. Borstel, S.E. Kapphan, and V.S. Vikhnin. *Semi-empirical calculations of the electronic and atomic structure of polarons and excitons in ABO(3) perovskite crystals*. Comput. Mat. Sci. **27**, 81-86 (2003)

118. V. Laguta, M. Zaritskii, M. Glinchuk, I. Bykov, J. Rosa, L. Jastrabik. *Symmetry-breaking Ta^{4+} centers in $KTaO_3$.* Phys. Rev. B **58**, 156-163 (1998)

119. D. v. d. Linde, O. Schirmer, and H. Kurz. *Intrinsic photorefractive effect of $LiNbO_3$.* Appl. Phys. **15**, 153-156 (1978)

120. R.I. Eglitis, E.A. Kotomin, G. Borstel. *Large scale modeling of point defects in ABO_3 perovskites.* Phys. Stat. Sol. (b) **2**, 113-119 (2005)

121. Yu.A. Firsov. *Polarony*. Nauka, Moscow (1975) (in Russian)

122. E. V. Bursian, Y. G. Girshberg, Y. A. Grushevsky, and V. V. Shapkin. *Optical properties of conducting barium titanate crystals and the nature of carriers in $BaTiO_3$.* Ferroelectrics **8**, 417- 418 (1973)

123. L. Grigorjeva, D.K. Millers, V. Pankratov, R.T. Williams, R.I. Eglitis, E.A. Kotomin, G. Borstel. *Experimental and theoretical studies of polaron optical properties in $KNbO_3$ perovskite.* Solid State Commun. **129**, 691-696 (2004)

124. Y. Yakoby, A. Linz. *Vibrational Properties of $KTaO_3$ at Critical Points in the Brillouin Zone.* Phys. Rev. B **9**, 2723-2742 (1974)

125. S. Prosandeev, E. Cockayne, B. Burton, A. Tutik. *First-principles computations of KTN.* arXiv:cond-mat/0401039 v2 7 Jan. 2004

126. A. Trepakov, A. I. Gubaev, S. E. Kapphan, P. Galinetto, F. Rossella, L. A. Boatner, P.P. Syrnikov, and L. Jastrabik. *UV light-induced IR absorption and photoconductivity in $KTa_{1-x}Nb_xO_3$.* International meeting on ferroelectricity (IMF-11). Accepted. To be published in Ferroelectrics.

127. M. DiDomenico, S.H. Wemple. *Optical properties of perovskite oxides in their paraelectric and ferroelectric phases.* Phys. Rev. **166**, 565-576 (1968)

128. T. Ishikawa, M. Itoh, M. Kurita, H. Shimoda, M. Takesada, T. Yagi, S. Koshihara. *Giant photoconductivity in quantum paraelectric oxides*. Ferroelectrics **298**, 141-143 (2004)

129. U. Bianchi, W. Kleemann, J. G. Bednorz. *Ferroelectric domain state transition of $SrTiO_3$:Ca*. Ferroelectrics **157**, 165-170 (1994)

130. R. S. Klein, G. E. Kugel, M. D. Glinchuk, R. O. Kuzan, I. V. Kondakova. *Photoconductivity in $KTaO_3$:Li single crystals.* Phys. Rev. B **50**, 9721-9728 (1994)

131. I. I. Tupitsyn, A. Deineka, V. A. Trepakov, L. Jastrabik, S. Kapphan. *Energy structure of $KTaO_3$ and $KTaO_3$: Li.* Phys. Rev. B **64**, 195111-195111-6 (2001)

8 List of Publications Resulting From This Work

1. *UV light-induced absorption in pure $KTaO_3$ at low temperature*. S.E. Kapphan, A.I. Gubaev and V.S. Vikhnin, Phys. Stat. Sol. (c), **2**, Issue 1, 128-131 (2005).

2. *Kinetics of the light-induced polaron- and VIS- centers SBN:Ce single crystals at low temperature.* A. Gubaev, S.Kapphan, I. Kislova, A. Kutsenko, R. Pankrath, V. Vikhnin, Phys. Stat. Sol. (c), **2**, Issue 1, 167-170 (2005).

3. *Doping-Dependent Properties in Photorefractive Congruent $Sr_xBa_{1-x}Nb_2O_6$: Ce, Cr Crystals*. A. Gubaev, R. Demirbilek, R. Pankrath, S. Kapphan, I. Kislova, B. Pedko, V. Trepakov, Ferroelectrics, **303**, 185-188 (2004).

4. *Photo dissociation of blue-light-induced VIS-Centers in SBN:Ce, Cr and in BCT:Fe into small polarons at low temperatures*. S.Kapphan, A. Gubaev, I. Kislova, A. Kutsenko, R. Pankrath, V. Vikhnin, Ferroelectrics, **303**, 107-112 (2004).

5. *Optical spectra, properties and first principles computations of $Ba(Fe,Nb)O_3$ and $Pb(Fe,Nb)O_3$*. R. Demirbilek, A.I. Gubaev, A.B. Kutsenko, S.E. Kapphan, I.P. Raevski, S.A. Prosandeev, B. Burton, L. Jastrabik, V.S. Vikhnin, Ferroelectrics, **302**, 279-283 (2004).

6. *Charge transfer vibronic excitons and their small clusters trapped by oxygen vacancies: optical manifestation of new metastable states in nominally pure $KTaO_3$ crystal*. V.S. Vikhnin, A.I. Gubaev and S.E. Kapphan, Phonons 2004, Phys. Stat. Sol. (c), **1**, Issue 11, 2844-2847 (2004).

7. *UV light-induced IR absorption and photoconductivity in $KTa_{1-x}Nb_xO_3$*. A. Trepakov, A. I. Gubaev, S. E. Kapphan, P. Galinetto, F. Rossella, L. A. Boatner, P.P. Syrnikov, and L. Jastrabik, International meeting on ferroelectricity (IMF-11). Accepted. To be published in Ferroelectrics.

8. *Photochromism and polaronic photo-charge localization in diluted $KTa_{1-x}Nb_xO_3$.* A. I. Gubaev, S.E. Kapphan, L. Jastrabik, P. P. Syrnikov and V. A. Trepakov. J. Appl. Phys., Accepted. To be published.

9. *A model of the polaronic origin of the VIS-centers in ferroelectric oxides : SBN-case.* V.S. Vikhnin, A.I. Gubaev, and S.E. Kapphan. To be published.

9 Declaration

I hereby declare that this submission is my own work and that, to the best of my knowledge and belief, it contains no material previously published or written by another person nor material which to a substantial extent has been accepted for the award of any other degree or diploma of the university or other institute of higher learning, except where due acknowledgment has been made in the text. I also declare that I have not tried to get a Ph.D. degree before.

Gubaev Airat

Osnabrueck, 10.11.2005.

10 Acknowledgments

I am especially thankful to Prof. Dr. Siegmar Kapphan. This thesis would be simply impossible without his overall help and support. The support and help of Prof. Kapphan were not limited to the scientific supervision, but has been extended to many problems of the daily life. I have learned a lot from numerous stimulating discussions with him in the past three years. Also I would like to thank his wife, Mrs. Marion Kapphan, for her help throughout my stay in Osnabrück.

I thank chairs of Graduate College 695 Prof. Dr. Klaus Betzler and Prof. Dr. Eckhard Krätzig for continuous maintaining the college on the highest level of organization. Also I want to thank them and Prof. Mirco Imlau, Prof. Dr. Manfred Wöhlecke, Dr. Ekaterina Shamonina, Prof. Dr. M. Fally and Prof. Dr. Heinz-Jürgen Schmidt for interesting and useful lectures offered by them within the framework of Graduate College.

A special thanks goes to Mr. Gregor Steinhoff, people in the mechanic workshop and in the electronic workshop for a lot of help during experiments, reparation and production of electronic parts, and help with cryostats and mechanics. I would like to say thanks to Dr. Wolfgang Mikosch for many helpful suggestions at several occasions during my stay at Osnabrueck University. I enjoyed the collaboration with Dr. Riza Demirbilek in the Fourier laboratory.

My particular thanks goes to Dr. R. Pankrath and Dr. Hesse for the growth of the crystals used in this work.

I would like to say thanks to Prof. Valentin Vikhnin and to Dr. Vladimir Trepakov for their valuable comments and suggestions. During my work in Osnabrueck University we have spent a lot of time to build a suitable theoretical model in order to explain all experimental results.

I would like to thank my wife Mrs. Liudmila Gubaeva and my parents. They have always been willing to support me in whatever endeavors I chose to pursue.

The financial support from the Graduate College 695 *"Nonlinearities of Optical Materials"*, financed by the Deutsche Forschungsgemeinschaft and the Federal State of Niedersachsen, is gratefully acknowledged.